

Development Of A Multiphase Composition Measurement Method By Using Capacitive Sensor Array

by

©Javier Ortiz Castro

A Dissertation submitted to the School of Graduate Studies in partial fulfillment of
the requirements for the degree of

PhD

Faculty of Engineering and Applied Science

Research advisor: Dr. Vlastimil Masek
Memorial University of Newfoundland

October 2015

St. John's

Newfoundland

Abstract

Multiphase flow, a flow of two or more liquid/gas components, is present in many industries. One of the challenges is to measure accurately the volumetric/mass ratio of each component against the total volume/mass. In the oil and gas industry, this kind of measurement is performed on a regular basis. Since the early 1980s, many methods have been proposed for multiphase flow measurement and some are commercially available today. However, these sensors often depend on a separator to isolate each phase, or use a homogenizer/mixer to achieve consistent solutions, or employ Gamma-Ray radiation provided by a nuclear source. The approach used in this research is to combine a sensor with an integrated cyclonic stratifier that transforms diverse flow regimes of multiphase flow into a channel flow regime. The sensor employs a relatively simple capacitive sensor array and allows for accurate measurements of phase fractions in real time. The system is also capable of compensating for drift in parameters such as permittivity, often caused by a changed chemical composition, e.g. the level of sulphur in the oil, the salinity of water, or due to variable temperature.

Table of Contents

Abstract	ii
Table of Contents	vi
List of Tables	viii
List of Figures	xiv
1 Introduction	1
1.1 Objectives	3
1.2 Organization of This Work	6
2 Multiphase Flow Measurements	7
2.1 Introduction	7
2.2 Types of Measurements	7
2.3 Flow Conditions	10
2.4 MPFM Measurement Approaches	13
2.4.1 Velocity Measurements	14
2.4.2 Component Fraction Measurement	19
2.4.2.1 Electrical Impedance Method	19
2.4.2.2 Gamma Ray	24

2.4.2.3	Other Techniques	25
2.5	Two Phase Liquid Separation	27
2.6	Conclusion	30
3	Proposed Measurement Method	31
3.1	Stratified Flow Regime in a Rectangular Measurement Chamber . . .	31
3.1.1	Linear Independence of the Measurement	32
3.1.2	Parallel-Capacitor Configuration	33
3.1.3	Series-Capacitor Configuration	34
3.1.4	Summary of Currently in use Methods and Proposed Electrode Configuration	34
3.2	Sensor Analysis	36
3.2.1	Parallel Plate Electrode Model	37
3.2.2	Concentric Cylindrical Electrode Model	43
3.3	FEA Analysis of a Prototype	48
3.3.1	Measurement Process Analysis	50
3.4	Conclusion	52
4	Dielectric Measurement	54
4.1	Introduction	54
4.2	Apparatus for the measurement of dielectric constant	55
4.3	Experiment	57
4.4	FEM approach to the ‘negative’ permittivity problem	64
4.5	Experimental resolution of the ‘negative’ permittivity	67
4.6	Incomplete Separation Study	73
4.6.1	Oil-in-water and water-in-oil differences	74
4.6.2	Permittivity transitional buffer effects	76

4.7	Conclusion	80
5	Design of a Compact Multiphase Flow Loop	82
5.1	Introduction	82
5.2	Multiphase Separator	83
5.3	Positive Displacement Pumps	86
5.4	Data Acquisition and Interfacing	87
5.5	Frequency Measurement	89
5.6	Software	90
5.7	Conclusion	92
6	Experimental Verification	93
6.1	Prototype #1	93
6.1.1	Capacitive Divider/Bridge	94
6.1.2	Frequency Tests	97
6.1.3	Temperature Test	98
6.1.3.1	Air Test	99
6.1.3.2	Air Pump Characterization	99
6.1.3.3	Air Pump Test Results	102
6.2	Capacitive Static Tests	104
6.2.1	Capacitive Test With a Single Coil	104
6.2.2	Capacitive Static Test With Two Coils	105
6.2.3	Capacitive Static Test With Two Coils and a Metal Shield	107
6.3	Prototype #2	108
6.3.1	Hydrocyclone	108
6.3.1.1	Capacitive Test	108
6.3.2	Signal Attenuation Study	111

6.3.3	Automated Attenuation Test	112
6.4	Conclusion	115
7	Flow separation study	116
7.1	Introduction	116
7.2	Flow visualization	117
7.2.1	Electrolytic Flow Visualization	117
7.2.2	Experimental Setup	118
7.3	CFD simulation	122
7.4	Turbo-cyclone	124
7.5	Conclusion	127
8	Conclusion And Future Work	130
8.1	Future Work	134
9	Publications	135
	References	137
	Bibliography	143
A	Flow Loop	146
A.1	Gear Pumps	146
A.2	Data Acquisition Card	147
B	Water and Oil Permittivities	148
B.1	Water Permittivity	148
B.2	Oil Permittivity	153

List of Tables

4.1	Apparatus dimensions	56
4.2	Glass wall - outer	58
4.3	Air dielectric	59
4.4	Water dielectric	60
4.5	Oil dielectric	61
4.6	Glass wall permittivity	63
4.7	Air, Water, Oil capacitances and permittivities	63
4.8	Original configuration model from Figure 4.2	65
4.9	Modified configuration model from Figure 4.8	66
4.10	Glass wall capacitance C3 - inside	68
4.11	Glass wall capacitance C1 - outside	69
4.12	Water dielectric capacitance C2 and permittivity	70
4.13	Capacitance data for determining saline water permittivity	71
4.14	Saline water capacitance	72
4.15	50% mixture separation in time	74
4.16	75
6.1	Coil Inductance Values	112
A.1	Lead Wire Assignments	146

A.2	Jumper Configuration for DAC0	147
A.3	Jumper Configuration for DAC1	147
B.1	Cole-Cole Parameters for the Spectra of the Crude Oils B1 and B2 . .	153

List of Figures

1.1	Conventional offshore component fraction measurements [1].	1
1.2	Individual offshore component fraction measurements [1].	3
2.1	Flow regimes in vertical pipes	10
2.2	Flow regimes for liquid and gas in horizontal pipes	11
2.3	Liquid-liquid flow	12
2.4	Venturi flowmeter	14
2.5	Ultrasonic flowmeter	15
2.6	Positive displacement flowmeter	16
2.7	Cross correlation method [3]	16
2.8	Electromagnetic flowmeter diagram	17
2.9	Capacitance principle [5]	20
2.10	Conductance principle [5]	21
2.11	Electrode configuration for capacitive sensors [21]	21
2.12	Equivalent capacitance circuits for different flow regimes [21].	22
2.13	Configurations of a two coaxial cylinder capacitor	23
2.14	Gamma ray plot for different component fractional ratios.[1]	24
2.15	Nonelectrode electromagnetic flowmeter	27
2.16	Hydrocyclone operating principle	28
2.17	Hydrocyclone application for sand filtering	29

2.18	Turbocyclone	29
3.1	Capacitive level measurement - parallel configuration	32
3.2	Series capacitor configuration level measurement	34
3.3	Hydrocyclone instrumented with three pairs of electrodes.	35
3.4	A cyclonic capacitive sensor with parallel plate electrodes. R_i Designates the outer radii, whereas r_i designates the radii of the inner core, and ρ_i is the radii of the oil/water interfases.	38
3.5	$C_i = C_i(\alpha\%)$, $i = 1, 2$, $\varepsilon_1 = 2.0$, $r_2 = 8 \times r_1$	40
3.6	$C_i = C_i(\alpha\%, \varepsilon_1)$, $i = 1, 2$, $r_2 = 8 \times r_1$	41
3.7	Linear disparity as r_2 increases against r_1	41
3.8	Model 1. The intersection angles for different values of α	42
3.9	Model 1. The intersection angles as a function of composition and ε_1	42
3.10	A cyclonic capacitive sensor with coaxial plate electrodes	44
3.11	$C_i = C_i(\alpha\%)$, $i = 1, 2$, $\varepsilon_1 = 2.0$, $r_2 = 8 \times r_1$	46
3.12	Linear disparity as r_2 increases against r_1	46
3.13	Model 2. Intersection angles for different values of α	47
3.14	Model 2. The intersection angles as a function of composition and ε_1	47
3.15	Configuration of the internal cone for a three electrode sensor	48
3.16	Capacitance for different composition and oil permittivities when $\varepsilon_w = 80$	50
3.17	Intersection angles in the plane $\varepsilon_1 - \alpha$	51
3.18	Intersection angles as a function of composition for different values of ε_1	51
3.19	Surfaces with the same capacitance	52
3.20	Lines with the same composition from different electrodes	53
4.1	Experimental apparatus	56

4.2	Capacitance measurement: (left) total capacitance with a given dielectric contained between the glass walls, (right) glass wall dielectric . .	57
4.3	Glass wall - outer	58
4.4	Air dielectric	59
4.5	Water dielectric	60
4.6	Oil dielectric	61
4.7	FEM electrostatic field simulation.	65
4.8	Conductive dielectric electrode for glass-wall capacitors analysis. . . .	66
4.9	Glass wall capacitance C3 - inside	68
4.10	Glass wall capacitance C1 - outside	69
4.11	Water dielectric capacitance C2 and permittivity	70
4.12	Adjusted the measured permittivity of water by 1.2 factor	71
4.13	Saline water capacitance	72
4.14	50% water/oil mixture: (TOP) oil bubbles dispersed in continuous water phase, (BOTTOM) water bubbles dispersed in continuous oil phase	75
4.15	Transitional buffer between the water and oil phase	77
4.16	C2 capacitance drifting with the transitional buffer width.	78
5.1	Multiphase flow loop	84
5.2	Multiphase separator configurations	85
5.3	Gear pumps	87
5.4	Gear pump response	87
5.5	Gear pump response plot	87
5.6	PC30D DAQ card timing and control section	89
5.7	Gear pump control diagram	91

6.1	First sensor prototype	93
6.2	Circuits employing a square signal for capacitance measurements. . .	94
6.3	Circuits employing a sinusoidal signal for capacitance measurements.	95
6.4	Calculated capacitances	96
6.5	Hartley FET oscillator, source drive	97
6.6	Frequency test results	98
6.7	Practical results vs numerical simulation results	98
6.8	Sensor response for different temperatures	100
6.9	Air pump characterization setup	101
6.10	Air pump response	101
6.11	Sensor response for varying air ratios	103
6.12	Capacitance measurement with a single coil and a metal pipe.	104
6.13	Capacitance measurement with two coils and a plastic pipe.	104
6.14	Capacitance measurement with two coils and a steel pipe.	105
6.15	Capacitance measurement with two coils and a plastic pipe.	106
6.16	Capacitance measurement with two coils and an unshielded plastic pipe	106
6.17	Capacitance measurement with two coils and a shielded plastic pipe .	107
6.18	Capacitance measurement results with two coils and a shielded plastic pipe	107
6.19	Hydrocyclone dimensions.	108
6.20	Hydrocyclone insert.	108
6.21	Hydrocyclone insert with inner coils	109
6.22	Capacitance between electrodes	110
6.23	Capacitive test 1 in prototype #2	110
6.24	Attenuation manual test	112
6.25	Experimental setup	113

6.26	Automated test results	114
7.1	Pulsating hydrogen bubbles [36]	118
7.2	Hydrocyclone modified for flow visualization	119
7.3	Three phase flow loop.	119
7.4	Power supply for flow visualization	120
7.5	Hydrocyclone with electrodes for electrolysis	120
7.6	Angular speed registered inside the hydrocyclone	121
7.7	Hydrocyclone port configuration for differential pressure measurements.	121
7.8	Differential pressure registered in the hydrocyclone	122
7.9	Flow simulation with OpenFOAM.	123
7.10	Transversal view of the sensor during the simulation.	124
7.11	Prototype sensor frontal view	125
7.12	Transversal view of the proposed sensor	125
7.13	Frontal view of the prototyped sensor	126
7.14	Prototyped sensor mounted on the flow loop.	126
7.15	Inductive method, top electrode response at 400kHz	128
7.16	Inductive method, middle electrode response at 400kHz	128
7.17	Inductive method, bottom electrode response at 400kHz	128
7.18	Inductive method, top electrode response at 6MHz	129
7.19	Inductive method, middle electrode response at 6MHz	129
7.20	Inductive method, bottom electrode response at 6MHz	129
B.1	Static permittivity of water	148
B.2	Variation in the permittivity of water (magnitude) with frequency at a fixed temperature	150

B.3	Variation in the real part of permittivity of water with frequency at a fixed temperature	150
B.4	Variation in the imaginary part of the permittivity of water with fre- quency at a fixed temperature	151
B.5	Variation in the real part of ε_{H_2O} vs frequency at different temperatures	151
B.6	Variation in the imaginary part of ε_{H_2O} vs frequency at different tem- peratures	152
B.7	Variation in magnitude of ε_{Oil} vs frequency	153
B.8	Variation in the real part of ε_{Oil} vs frequency	154
B.9	Variation in the imaginary part of ε_{Oil} vs frequency	154

Chapter 1

Introduction

An accurate measurement of fractional components of oil, gas and water in a production well allows for efficient management of the oil and gas (O&G) field. Traditionally, such measurement is performed by separating the multiple phases and routing each of the resulting single-phase flows into a conventional flowmeter (Figure 1.1). Due to

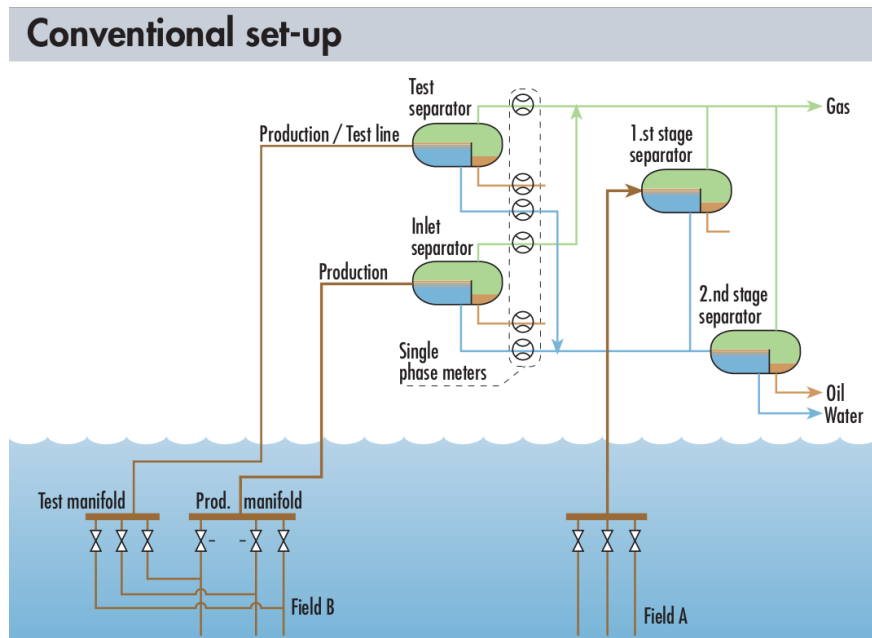


Figure 1.1: Conventional offshore component fraction measurements [1].

the involved complexities of O&G production fields and the separation process, this measurement is performed once in a couple of weeks using a chain of ‘test’ separators. This method is becoming increasingly prohibitive in view of faster reservoir dynamics and complex multi-party ownerships of many production fields today. Because the individual well readings are taken in a cycle of few weeks, a potential loss of revenues may occur in between the readings if the composition ratio drifts. It is therefore more advantageous to complement or even replace this traditional technique with a real-time composition measurement performed at each well head.

Over the past three decades, diverse Oil companies have developed seabed processing in which case the testing equipment is avoided completely due to the high cost and complexity of the main processing system. This new technology that allows the simultaneous measurement of the oil, water and gas fractions in a flow, under a wide range of temperatures, pressures and composition changes is called Multiphase Flow Metering (MPFM) [2] (Figure 1.2).

Since early 1980s, different methods have been proposed to obtain the component fractions in an oil well [3]. The multiphase flow sensors currently available commercially claim having an accuracy ranging from 2% to 5% [4], however, some of these instruments were calibrated against other methods having unpublished uncertainties. These sensors do not account for drifts in phase properties and therefore need to be recalibrated periodically, which can be done again in a cycle of a few weeks only. In this research, a new capacitance based sensor is being developed to measure the component fractions in a mixture without the need for recalibration. The accuracy of the sensor is expected to match or exceed those of the current instruments in a span of practical O&G concentrations (10%-100%). A precise gauging system integrated in a multiphase test loop was developed to measure the calibration curves of the developed instruments.

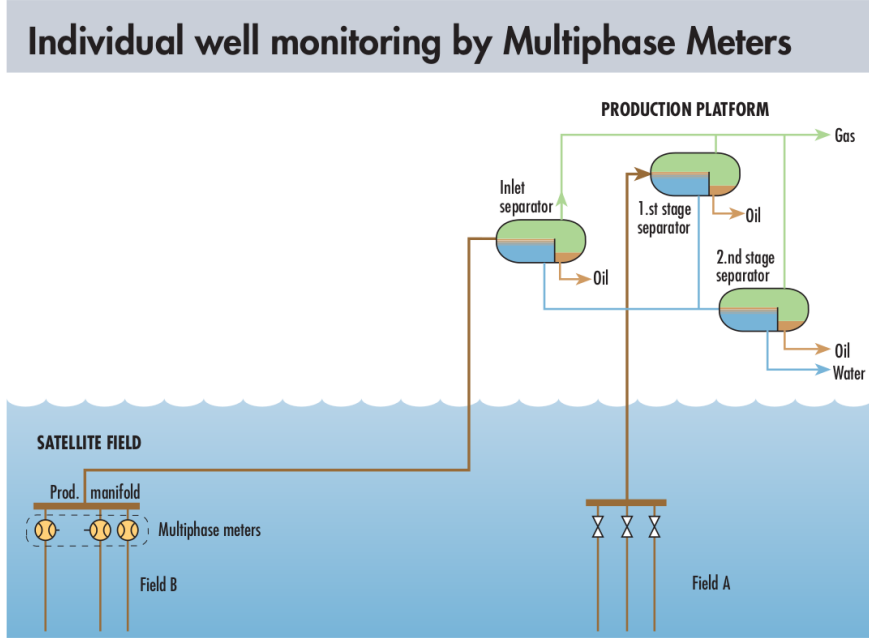


Figure 1.2: Individual offshore component fraction measurements [1].

1.1 Objectives

This R&D work is guided by a set of requirements needed to develop a technology that is desired by the industry but is currently unavailable. The main goal of this research is to develop a sensor that meets the following criteria:

1. Employ a non-nuclear detection technique:
 - In this work a capacitance based technique was prototyped which proved to be highly suitable to create a robust industrial device at a low cost, fast dynamic response, and a high accuracy due to a large discrepancy between the dielectric constants ($\text{Gas} \approx 1$, $\text{Oil} \approx 2$, $\text{Water} \approx 80$).
2. Provide intrinsic safety as no electrical part is directly exposed to the O&G flow.
The power levels will be tuned later to fully meet the standard.

3. Avoid mixing of liquid-liquid-gas phases which translates into a non-complicated product separation downstream. Using a homogenizer or mixer in some commercial models turns the multiphase flow into an emulsion that can be difficult to break downstream without using chemicals and a prolonged separation time.
4. Accept a wide range of concentrations, preferably in a range of 0% to 100% oil in the oil and water liquid phase.
5. Extend lifetime and be maintenance free. This sensor is obstruction free with no exposed parts to be abraded by a flow of suspended solids or sand. This makes it highly suitable for offshore installations near the seafloor, the location that is difficult to access after the initial installation. No deposits or clogs can form inside the sensor.
6. Provide Real Time measurement without a need to take characteristic volume samples. This sensor is an inline type sensor that characterizes the entire flow.
7. Immune to phase parameters or temperature drifts by using a redundancy in the data collection.
8. Robust and low complexity, resulting in a technology deployable on the ocean floor at a lower manufacturing cost.

The above requirements can not be achieved without a number of ‘prerequisites’ or trade-offs. One prerequisite is the pressure drop across the instrument that is induced by the cyclone operation. The flow follows a non-obtrusive path with smooth wall surfaces made of an abrasion-free ceramic coating and turbulence-free flow interfaces. However the fluid momentum in the cyclone is gained at a cost of pressure loss. Additional pressure loss may result when a turbine is used to spin the outer shell of the cyclone to ensure a laminar flow along the wall. This concept may however be

redesigned such that the shell would not be driven by the flow but by an external drive.

Having a direct drive motor actuated cyclone would also result in an improved stratification process that would be independent of the fluid flow velocity. Normally, a minimum flow is required to achieve the needed level of stratification within the cyclonic sensor chamber when a static cyclone is used. If a low flow velocity is present, a recirculating pump that takes a portion of the output flow and re-feeds it to the sensor's inlet can be used, this method may not be as practical as the motor assisted cyclone mentioned above.

There are already subsea production facilities, mostly off the Norway coast, that separate gas from liquids and even produced water at the sea floor. The developed flowmeter could also be modified to be used in those cases when liquid-gas or liquid-liquid-gas separation is required.

In addition to the pressure drop, the top-down vertical flow through the designed instrument was necessary for correct cyclone operation with gravity assistance. However, if a motor driven cyclone is used, a horizontal axis instrument could be implemented. In addition to the development of the sensor itself, during this research other challenges have been overcome. For example, in order to test the sensor, a compact flow loop was developed. The developed flow loop comprises the control of motors, the development of the signal conditioning system, data acquisition and storage system for further data processing and analysis. Other challenges faced during this research are described later in this document.

1.2 Organization of This Work

Chapter 2 describes related work in the area of multiphase flow measurement. Chapter 3 describes the proposed sensor, based on a capacitive technique and presents the theoretical and numerical analysis of the sensor. Chapter 4 provides a further study on the differences in permeabilities of water and oil, as well as mixtures with different texture. Both numerical and experimental approaches are presented and compared. In order to perform the experimental tests, a compact flow loop system was developed. This flow loop that allows evaluation and calibration of the multiphase flowmeter is described in detail in Chapter 5. The experimental verification of the sensor using the flow loop is described in Chapter 6. The measurements were performed by using two different techniques. The first technique is based on the amplitude of a signal; during the experiments performed using this technique, the measurements were affected by ground loops and noise induced through the water liquid phase. In order to avoid ground loops, a second technique, which uses a capacitance-to-frequency converter was tested and described in the same Chapter. Finally, another proposed configuration for a sensor based on the capacitive principle is described at the end of Chapter 6 along with the experimental results. Chapter 7 describes efforts to understand the hydrodynamical processes within the hydrocyclone as well as the new apparatus for speed augmented turbocyclone. The conclusion and the future work are discussed in Chapter 8.

Chapter 2

Multiphase Flow Measurements

2.1 Introduction

Multiphase flow measurement is a challenging task that involves many parameters. The sensor requirements vary considerably depending on the purpose of the measurement. In addition, a particular sensor can yield different values for different spatial distributions of fluids in a multiphase flow. This Chapter describes the most common types of measurements, followed by different types of flows that exist in a pipe and affect the sensor response. Later, different approaches and techniques currently used in flow measurement are described, followed by the process of liquid-liquid separation needed in this sensor prior to a measurement.

2.2 Types of Measurements

During oil production, it is necessary to measure the amount of oil and water that is being extracted. These measurements can be made for various purposes: well monitoring, well testing, production allocation or fiscal reasons.

During the decline of production, it is a well known fact that oil production rate varies

greatly over time. In order to have a continuous flow, high pressurized gas is injected into the well. If the injected gas is insufficient, the oil rate will be too low, and if the amount of injected gas is high this leads to more expensive extraction costs. In order to optimize the amount of gas that should be injected, real time measurements are needed and they constitute an invaluable tool in oil extraction. Transient variations in oil flow cannot be measured and they pass unnoticed when the measurements are made on a tank separator.

Another aspect of well monitoring is referred to as *Flow Assurance*. Flow Assurance is related with all aspects of oil flow from the extraction from the oil well to the sales or the transfer point. By constant flow monitoring, it is easier to identify possible future blockages in the pipes caused by substances that accompany the oil, such as wax, sand, rocks or asphaltenes. During flow monitoring, the tendency of the flow is more important than an instant value, i.e., the precision is more important than accuracy in composition measurement.

Another different measurement is *Well Testing*. It is important to monitor the performance of each oil well in order to maximize the life span of the oil field. These measurements have an impact on important decision making like shutting down a well, drilling a new one, increasing or decreasing the extraction rate from the field, etc. Traditionally, the well testing is performed by using a test separator. Sometimes this test separator works “in parallel” with the production separator. During a measurement, the flow from a well is directed to the test separator, where the flow is separated into oil, gas and water. The recorded value is used as the “theoretical contribution value” of that particular oil well to the overall production from the production facility. The ‘theoretical contribution value’ from that particular oil well is considered constant until the next measurement occurs, after measurements from other oil wells are performed, however, the real contribution can have different values

in time due to transient changes in flow. The typical instrumentation available for a test separator allows for measurements of each of the phases with different accuracy: it is said that the gas is measured with an uncertainty better than 5%, whereas the uncertainty for water and oil is 2% and 1% respectively [5]. It is clear that the use of a Multiphase Flow Meter for these applications allows better decision making as well as better oil field management.

The oil that enters into the production facility can originate from different wells and different owners because the pipes transporting the oil from different companies are commingled together. The measurement of the flow before it enters the manifold is very important, because this allows the allocation of the oil ownership to the different companies at the outlet of the production facility. These types of measurements, called *Fiscal Measurements* are used as the base for the transfer of money between the government and oil companies or between oil companies. The requirements needed for these measurements are more stringent in order to avoid any revenue losses.

Currently an international regulation for MPFM accuracy does not exist, however, there are three basic requirements for multiphase measurements: approximately 5 to 10% for reservoir management, approximately 2 to 5% for production allocation and approximately 0.25 to 1% for fiscal metering [6]. Traditionally, measurements in the oil industry are done using separator tanks and then measuring each phase separately. The use of multiphase flow meters leads to savings because the test separator and associated pipelines are no longer required. In addition, the use of individual MPFMs on each oil pipe connected to the same manifold allows continuous measurements, and these can be installed undersea. In this way it is not necessary to shutdown wells to test them individually, thus avoiding the instabilities in production resulting from the shut-down cycles. The MPFMs also provide real time information that allows for better well monitoring and the detection of any variation in the production rate, for

example problems due to well slugging or gas lift. This results in an extension of the life span of the oil fields and a simplified allocation of production when it is needed.

2.3 Flow Conditions

The flow from an oil well is a multiphase flow, and it is a challenging phenomenon to model, which in turns makes it very difficult to perform any predictions. The different distributions of flows in a multiphase flow are classified into flow regimes. The characteristics of each regime depend upon different factors, such as the ratio of the phases, the velocity of each phase, orientation and geometry of the pipes, etc. The most common liquid-gas flow regimes that can be observed in a vertical pipe are shown in Figure 2.1. The *Bubble Flow* regime occurs when one flow is continuous and the second flow is dispersed into it in the form of tiny bubbles. If small bubbles merge together, they can form larger bubbles and if these bubbles continue growing and approaching a size comparable to the diameter of the pipe, then this flow is called

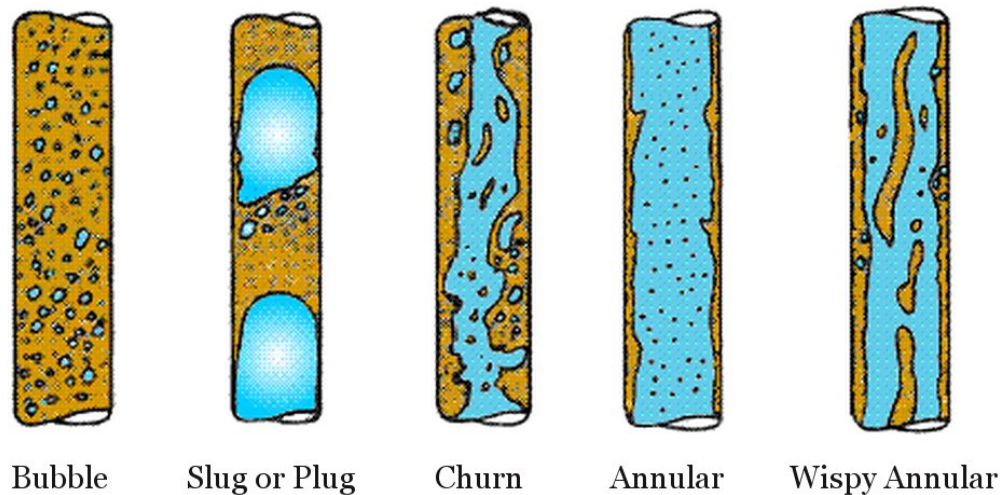


Figure 2.1: Flow regimes in vertical pipes

Slug or Plug Flow. In a *Churn Flow*, the bubbles are smaller than in the previous case, and they have a variable diameter and are almost continuous. In *Annular Flow*, one of the phases flows almost totally in a thin layer on the walls of this pipe, whereas the second phase flows in the center, along with some small bubbles of the first flow. When the bubbles in the middle increase, they gather and form streaks yielding a *Wispy Flow*.

In a horizontal flow, the regimes are slightly different because of the constant action of the gravity acting perpendicularly to the flow. The most common types of horizontal regimes are shown in Figure 2.2. If the phases are completely separated, one of them flowing on the top of the other, then it is a *Stratified Flow*. In *Bubble Flow*, the bubbles are dispersed in a continuous phase, even though they are more concentrated at the top of the fluid due to gravity. An annular-dispersed flow has a layer of liquid flowing on the walls, this layer has a variable thickness due to the effect of gravity and the gas flows in the center in the form of small bubbles. When the bubbles are larger, it then becomes plug or slug flow. The regimes for liquid-liquid flows, even

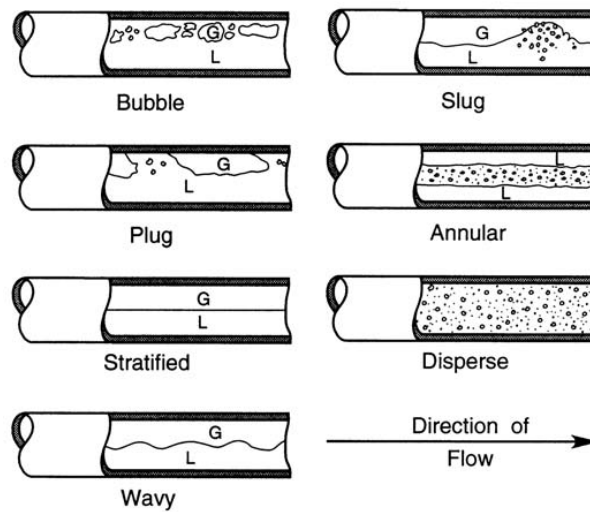


Figure 2.2: Flow regimes for liquid and gas in horizontal pipes


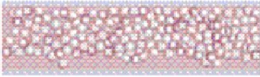

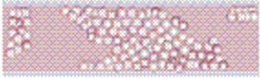

Description	Flow
Stratified: has some mixture at the interface	
Mixed: usually has a dispersion layer and a free phase	
Annular: has one liquid in the center surrounded by the other liquid	
Intermittent: has two phases or a mixture of them occupy the pipe alternately	
Dispersed: The flows are mixed homogeneously	

Figure 2.3: Liquid-liquid flow

though they have great importance in many industries, have not been studied in as much detail as gas-liquid flows [7]. They are presented in a wide variety of patterns ranging from stratified flow at low velocities to complete dispersion at high velocities [8], some depictions of these flows are shown in Figure 2.3.

The different flow regimes make the multiphase flow measurements a difficult task. The first MPFM appeared at the beginnings of the 1990s, and their use is still increasing. There are many techniques employed, however, the measurement of multiphase flow is still a challenge. The oil that is produced and the conditions under which it is being produced, vary greatly over time. This means that an ideal MPFM should be able, at least in theory, to measure the percentage of each phase of the flow, over a wide range of temperatures, pressures, flow regimes and to take measurements continuously, in an non-invasive way, it should be ideally maintenance free, simple and inexpensive. It is clear that such a MPFM still does not exist today [9]. However, different attempts have been made to measure these flows, employing different techniques. The following section explains some of the techniques employed and also the

techniques that have been used in this research.

2.4 MPFM Measurement Approaches

The main information that the users of MPFM expect to obtain is the mass flow rate of the oil, water and gas. An ideal MPFM should be able to obtain this data directly; however, this type of flowmeter does not exist and an inferential mass method should be used instead. In this method, the cross-sectional area, as well as the velocity of each flow is measured. Using this data along with the density, which can be obtained elsewhere during the process, the mass is calculated. Therefore, the main problem can be divided into two parts, one is to measure the velocities of the oil, water and gas, and the other part is to measure the component fraction of the flow. In practice, the speed of the three flows are measured (v_g , v_w and v_o) and usually only two out of the three component fractions are measured (α and β), the other is calculated from the other two ($1 - (\alpha + \beta)$) [3].

The total mass is calculated as

$$M = \alpha v_g \rho_g + \beta v_w \rho_w + [1 - (\alpha + \beta)] v_o \rho_o \quad (2.1)$$

where: α = gas void fraction

β = water fraction

v_g = gas velocity

v_w = water velocity

v_o = oil velocity

ρ_g = density of gas

ρ_w = density of water

ρ_o = density of oil

There are two approaches to measure these parameters: one is homogenization (in line metering), and the other is partial separation (or separation type). In the first method, the three phase flow passes through a mixer in order to obtain a homogeneous fluid before being measured. In the homogeneous flow, the three phases travel at the same speed, and also the density of the flow is the same, and as a result, a reduced number of measurements is required. In the second approach, partial separation, the flow is separated into gas and liquid. Once that the flow is separated, single phase and bi-phase flow measurements can be applied on each flow. The two sections below review some key technologies in flow velocity measurement and a number of component fraction techniques.

2.4.1 Velocity Measurements

Venturi based flow meters use the relationship between the pressure and velocity, i.e. the Venturi effect. This type of sensors measures the pressure difference between the upstream (unobstructed) section and a narrow constriction segment downstream of the pipe. This difference is used to calculate the velocity of the flow (Figure 2.4). In order to achieve the highest accuracy when there is a multiphase flow it is recommended to have the flow as homogeneous as possible.

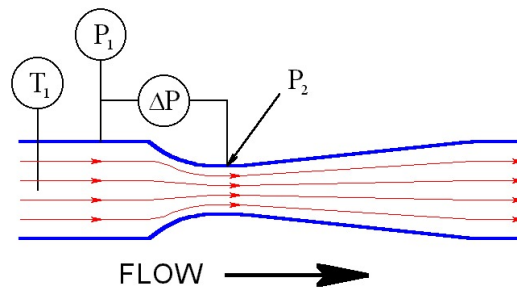


Figure 2.4: Venturi flowmeter

Ultrasonic Doppler Flowmeters use the change in frequency of an acoustic signal as it bounces from suspended particles, e.g. gas bubbles, as they are carried by the flow. The velocity can be conveniently calculated from the “sent” and “received” signal frequency (see Figure 2.5a).

Ultrasonic Transit Time Flowmeters also utilize acoustic signals but in a setting where the time between the signal generation and its reception is measured twice, once traveling upstream and then traveling downstream. The velocity of a signal traveling in the fluid is equal to the speed of the signal propagation with the speed of the flow superimposed. Since the difference in velocities between the signal traveling downstream and the signal traveling upstream is equal to twice the flow speed, the flow velocity can be calculated easily (Figure 2.5b).

In addition to the Doppler and transit time, some research have been done to develop acoustic based multiphase flow meters. Those attempts used a complex array of electrical and acoustic sensors and the signals are processed by using neural networks to try to measure the composition and the flow velocities [10].

Positive Displacement Flowmeters (PD) are designed as a reversal of positive displacement pumps. They are based on a mechanical cyclic movement of enclosed cavities that undergo volumetric changes at the meter input and output. This allows the

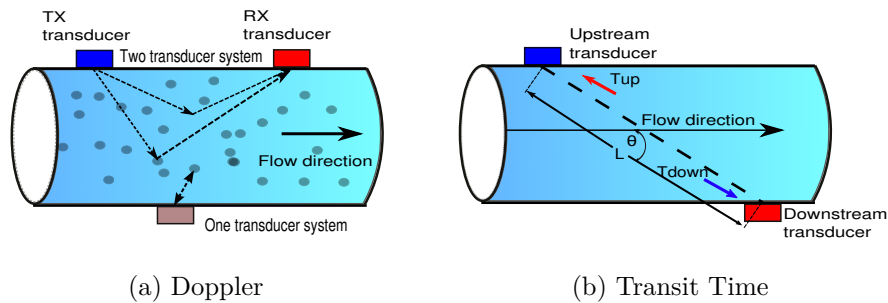


Figure 2.5: Ultrasonic flowmeter

passing of a pre-determined amount of liquid in each cycle. A PD meter can be used to measure the total flow rate as a part of a multiphase flowmeter (Figure 2.6).

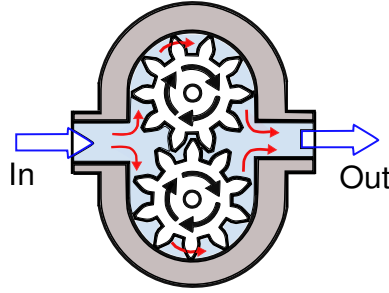


Figure 2.6: Positive displacement flowmeter

Cross Correlation Flowmeters use the particles in the flow, the flow regime variation or the turbulence of a flow, to predict the time of passing of the same feature along two locations that are a known distance apart (Figure 2.7). This measurement method can be instrumented by different types of transducers, for example: microwave, impedance, gamma-ray, differential pressure, or ultrasonic. In [11] this method was used in combination with impedance measurement, to determine individual velocities of gas and liquid phases. One of the advantages of this method is that the velocity is measured directly and there is no need to calibrate the sensor.

Magnetic Flowmeters have a limited use in the oil and gas industry because they are

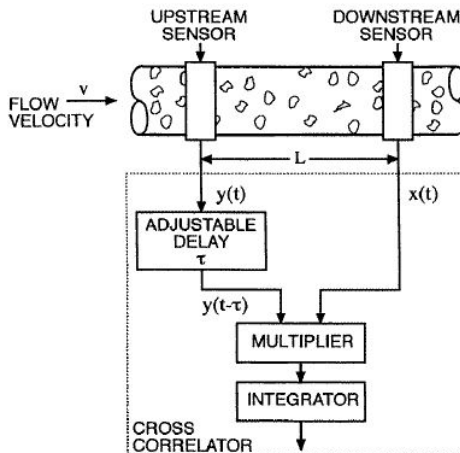


Figure 2.7: Cross correlation method [3]

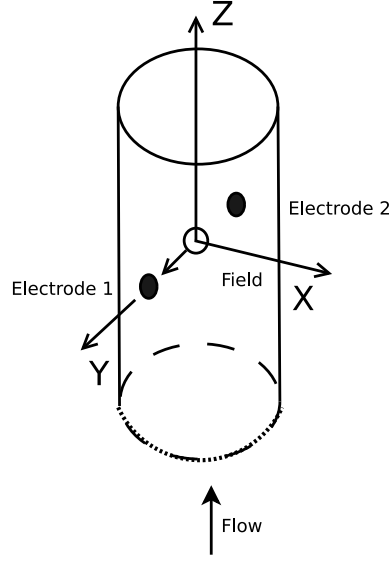


Figure 2.8: Electromagnetic flowmeter diagram

based on the conductivity of the flowing fluid. They are easily installed and offer a truly non-invasive method of flow measurement, which means that they do not present any hydraulic resistance to the flow [12], [13].

Part of this research investigated a method based on the electromagnetic phenomena which requires a more detailed introduction. Figure 2.8 shows a typical electromagnetic flowmeter. Electromagnetic flowmeters are based on the Faraday principle. In these type of sensors, the voltage across the electrodes is proportional to the speed of the fluid. The Faraday law states that if a conductor of length l is moving perpendicularly to the flux lines of an applied magnetic field, then the induced voltage across the terminals of the conductor is expressed by:

$$e = Blv \quad (2.2)$$

where B is the magnetic flux, l is the length of the wire, or in this case, the diameter

of the pipe, and v is the velocity of the flow. Substituting the equation (2.2) becomes:

$$e = BDv \quad (2.3)$$

If the ends of the conductor (liquid), in this case the electrodes are connected to another circuit, an electric current will circulate; this current is also proportional to the flow rate. This type of magnetic flowmeters are used for measuring the volumetric flow of the liquid $Q[\frac{L}{s}]$. The volumetric flow is related to velocity by

$$Q = Av \quad (2.4)$$

where the area of the pipe is:

$$A = \frac{\pi D^2}{4} \quad (2.5)$$

The substitution of (2.5) and (2.4) into (2.3) gives:

$$e = \frac{4BQ}{\pi D} \quad (2.6)$$

According to equation (2.2), if the magnetic field and the diameter remain constant, then the output voltage is linearly proportional to the flow, Q .

Even when the electromagnetic flowmeters work under the principle described here, there are some slight differences, some of them work with either AC, DC or permanent magnets.

Shercliff [14] established that in a magnetic flowmeter the induced voltage is independent of the flow profile provided that the flow is radially symmetrical. In a recent research [15], one magnetic flowmeter with one coil, and an array of electrodes was used to measure the multiphase velocity profiles in a pipe. In equation (2.6), it is assumed that the liquid is a conductor, this type of flowmeters is applied in measuring conductive liquids such as: acids, bases, slurries, foods, dyes, polymers, emulsions and flow mixtures with conductivities higher than the minimal conductivity. It is said that this type of flowmeters should be applied for measurements of liquids with a minimum conductivity between $1 \frac{\mu S}{cm}$ and $5 \frac{\mu S}{cm}$. Tap water has a conductivity of $200 \frac{\mu S}{cm}$ whereas gasoline has $0.01 \frac{\mu S}{cm}$. However, Al-Rabe *et al* [16], developed the theory for applying magnetic flowmeters to poorly conducting fluids, such as oil and gas.

2.4.2 Component Fraction Measurement

The most common techniques for component fraction measurements are gamma ray attenuation, microwave, electrical impedance techniques and venturi meters. Other less common techniques include Pulsed Neutron Activation (PNA) and Nuclear Magnetic Resonance (NMR) [3] [5]. Composition measurement is the major research area of this work. A review of the current techniques in use or in a research domain follows.

2.4.2.1 Electrical Impedance Method

The impedance technique is based on the measurement of the basic electrical properties of the liquids. The conductance and capacitance of the liquid are measured across the pipe with contact or non-contact electrodes (Figure 2.9). Since the area of the electrodes is always constant, the measured values depend only upon the conductivity and permittivity of the fluid. The permittivity or dielectric constant which

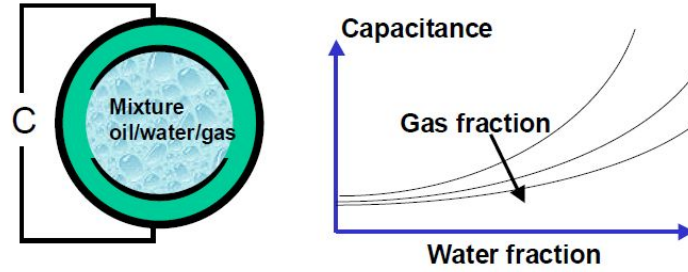


Figure 2.9: Capacitance principle [5]

is different for different substances (in this case oil and water, see Appendix B.1) is used for measuring the capacitance of a mixture composition. The measured value of capacitance, depends on the value of the electric permittivity of each phase and also on the component fraction of oil and water in the mixture.

The capacitance measurements are effective as long as the flow of oil (or non-conductive flow) is continuous, i.e., as long as the conductive flow does not form a continuous path between the electrodes. In a configuration like the one shown in Figure 2.9, if the water cut is below 60-70% the water path may not be continuous. If, however, the water cut increases above this value, then a continuous path is formed and a short circuit between the electrodes occurs and this technique is no longer useful. In these cases, other techniques should be used, for example, conductivity measurement.

The conductivity is measured in many cases by applying a controlled current into the flow and measuring the resultant voltage across the electrodes. The conductivity is calculated by using Ohm's Law with the voltage and current data (Figure 2.10).

Capacitive sensors have been widely studied during the 1970s and 1980s [5]. These studies included several electrode configurations, including: flat plate, concave, ring, helical wound, multiple helix, four concave plates[17], in contact or isolated from the fluid, etc. In those studies, capacitances between 0.1 to 10[pF] are very common.

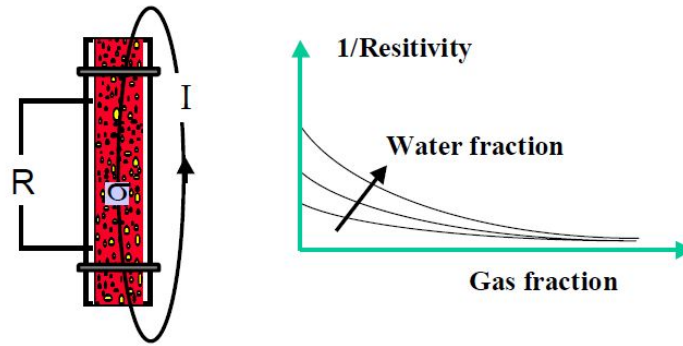


Figure 2.10: Conductance principle [5]

Proper shielding is needed to avoid stray capacitances and to obtain a good signal to noise ratio, since the measured capacitance is very small (on the order of picofarads). Elkow and Rezkallah (1996) compared the performance of two sensors, one with two helical-type electrodes and one sensor with two concave parallel electrodes located at opposite sides of the pipe. They found that problems associated with helicoidal electrodes, like non-linearities, poor sensitivity and poor response can be eliminated by using concave plate electrodes [18] (Figure 2.11).

One of the limiting factors in the use of capacitive sensors is the flow regime. The electric equivalent circuit of the flow inside the pipe changes depending on the type of regime, as can be seen in Figure 2.12.

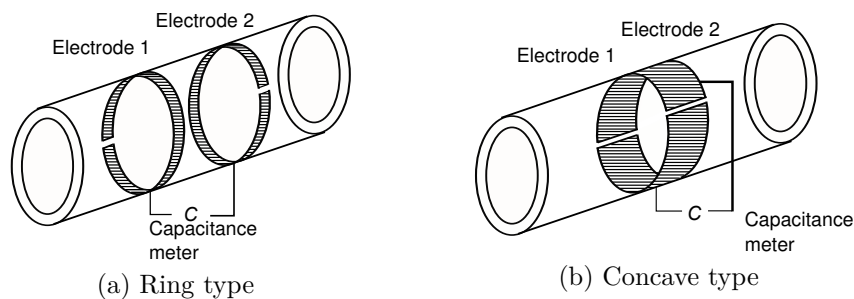


Figure 2.11: Electrode configuration for capacitive sensors [21]

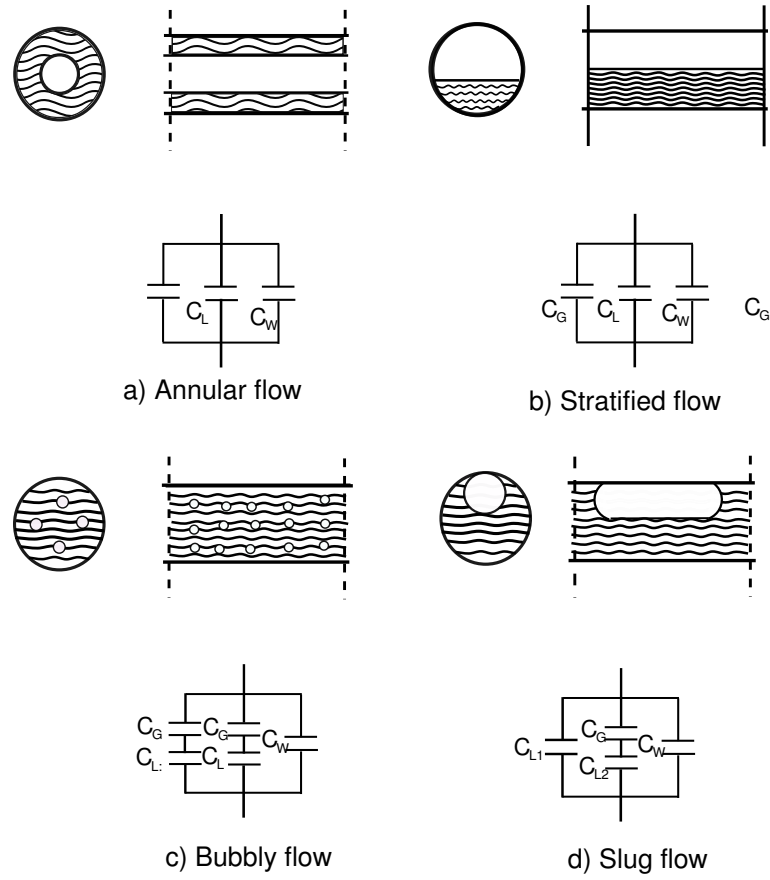


Figure 2.12: Equivalent capacitance circuits for different flow regimes [21].

In order to reduce the regime dependence, Merilo *et al* [19] devised and tested a sensor with three pairs of helical electrodes around the pipe. They measured sequentially the conductance between the opposite electrodes which results in a rotating field, and as a consequence, an average of the field is measured. Lucas and Simonian [20] investigated the rotating electrostatic field using multi-electrode capacitive sensors. This reduced the regime dependency, but the dynamic response of that type of sensor is slower than the response from a simple electrode pair.

Sensors for oil and water measurements with helicoidal electrodes are commercially

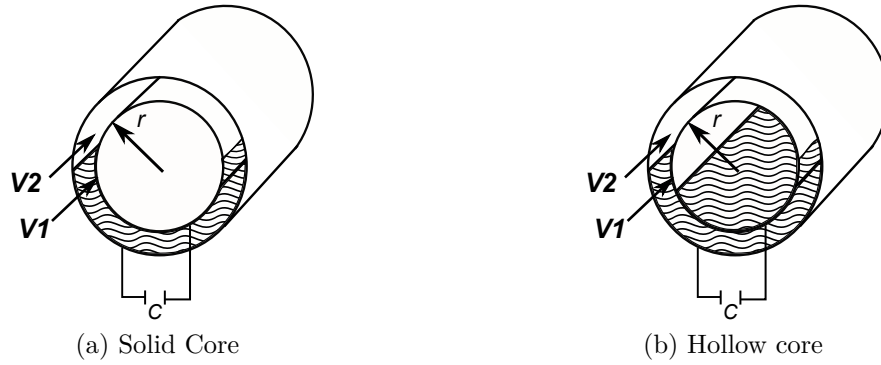


Figure 2.13: Configurations of a two coaxial cylinder capacitor

available. Rotating field and helicoidal sensors have not yet been applied to three-phase flow, however, this principle could be applied to such flows, for example oil, water and gas flows [3].

Research has been conducted for the use of a coaxial capacitor as a sensor. Salah *et al* [22] performed a series of experiments with solid core sensors, as well as with hollow core type sensors (Figure 2.13). For the solid core sensors, the experimental results showed a linear relationship between the measured capacitance and the volume phase ratios. The experimental results showed also that, in the case of a hollow core sensor, the response is not linear and a linearization equation must be used. The experiments also showed that coaxial type sensors have a better sensitivity and linearity than sensors with electrodes on the outside of the pipes. This sensor assumes a fully developed stratified flow in a horizontal pipe segment. This is the major limitation as this condition cannot be guaranteed in the O&G field production case. The chosen method is somewhat similar to this technique in terms of using the two-ring electrode, however, the developed sensor force the flow stratification by using a cyclone separator concept (see Section 2.5). The hydrocyclone creates coaxial layers of flow with the ring electrodes which establishes ideal conditions to the composition measurement.

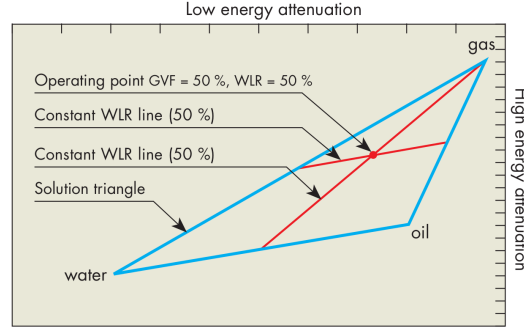


Figure 2.14: Gamma ray plot for different component fractional ratios.[1]

2.4.2.2 Gamma Ray

Gamma Densitometers are based on a principle in which the intensity of gamma rays decrease exponentially as they travel through a substance; the more dense the material is, the more intense attenuation is experienced. There are different γ attenuation methods: single, double or multiple energy attenuation. A single ray measurement can be representative of the density of the flow only if the phases are mixed homogeneously. If that is not the case, then a double γ -ray should be used. A dual energy meter uses a single radioactive chemical source which emits gamma rays at multiple energy levels. The signal from the detectors located at the other side of the pipe measure the attenuation of the rays at two energy levels. These signals are compared to the attenuation of the pure individual components (Figure 2.14). By using this method it is possible to determine several parameters such as Water-Liquid Ratio (WLR)¹ or Gas Volume Fraction (GVF)². The corners of the largest triangle in Figure 2.14 represent the single phase attenuation. The same plot shows an example with an operating point of 50% GVF and a 50% WLR. This technique can be used for any combination of two or three different flows, with only few limitations. One of them is the salinity of the water. Since salt has a higher attenuation coefficient than the

¹WLR is the ratio of the water flow rate to the total flow rate of the mixture [m^3/m^3]

²GVF is the ratio of the gas volume flow rate to the total flow volume flow rate [%]

water, a change in salinity can be a source of error. Scheers and Letton (1996) [25], described a triple γ -ray system in which the third ray is used to calculate the salinity of the water. Another source of inaccuracies is the γ -ray source itself, since it does not have an accurate value, but a statistical approximation, there is always a trade-off between the accuracy obtained and the time required for the measurement. Also the intensity of the γ -ray source can be increased, but the safety measures for human operators need to be increased as well. The use of low energy rays can mitigate the hazard involved; in such cases a radiation window is required, as part of the system. In this project, some features of this method have been adopted, in particular, the use of multiple energy levels in the capacitive sensor were emulated. The key is having each measurement decoupled from others, i.e. being linearly independent of each other. In this way only, it is possible to discriminate the multiple measured parameters. It will be demonstrated later how the linear decoupling discrepancy for the measurement uncertainty is quite important.

2.4.2.3 Other Techniques

The use of *Microwave technology* is based on the variation of the dielectric constant differences between oil and water. In a flow mixture of oil and water, the dielectric constant will have a value which is dependent upon the volume fraction of the two liquids. There are several operation principles for these type of sensors which have been described by Nyfors, E. & P. Vainikainen (1989) [5]. The most common methods, resonance and attenuation, are described below.

The cavity resonant method involves a transmitter and a resonator sensor. The transmitter sends a signal varying in frequency which is detected by the receiver. The maximum amplitude or resonant frequency will depend on the geometry of the resonator and the electric permittivity in the cavity. Thus, by finding the resonant frequency,

the electric properties of the materials can be found and the ratio of oil and water calculated. In theory this method can only be used with oil continuous phase, since the attenuation in water is considerably bigger compared to that on oil [23]. However in [24], the resonant method has been tested for fresh and salt water with frequencies in the range of 100-400MHz.

The other method is based on attenuation of a single frequency signal. The component fraction depends on the attenuation of the signal or the change of a signal phase.

Nuclear Magnetic Resonance Flowmeters (NMR) are employed for analyzing multi-component bodies in many industries. In this technique, a strong magnetic field is applied along RF signal and the transition between spin states is produced. When the RF signal is turned off the spins return to their low energy state, producing another RF signal at the resonant frequency associated with the spin flip. The spectrum of the generated RF signal is related to the volume of interest composition. In case of the multiphase flow, two such sensors can be located at a known spatial separation and the cross-correlation techniques described above can be applied to calculate the flow velocity [26].

Pulsed Neutron Activation (PNA) uses a high energy source of neutrons to irradiate the flowing mixture, introducing activity in the flow. This activity causes gamma radiation to be produced. The spectra of this detected radiation is related to the chemical composition and phase fraction of the mixture.

Linear Variable Differential Transformer (LVDT) makes use of three coil windings that are wrapped around the flow pipe. The coil in the middle is the primary excited by AC current which generates AC magnetic flux inside the pipe. The interaction of the AC flux with a conductive fluid generates AC signal in two secondary or detection coils that are on each side of the primary coil. The flux has a radial component (Φ_r) directed to the center of the coil on one side of the primary and a second radial com-

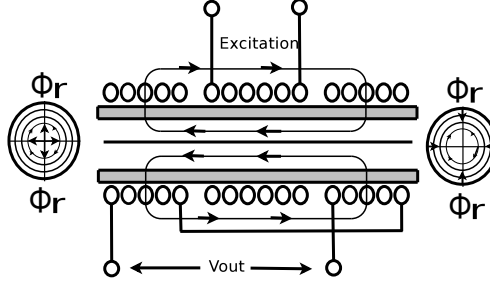


Figure 2.15: Nonelectrode electromagnetic flowmeter

ponent from the center to the outside on the other side of the coil. When conductive liquid passes across the lines of radial flux (Φ_r), concentric loops of currents are generated at both ends. These currents generate voltages in the two detection coils. The electromotive force induced by the main longitudinal flux is cancelled by connecting the two secondary coils in anti-serial connection (Figure 2.15). This type of sensor is very useful for measuring fluids that could otherwise generate sediments on the magnetic flowmeter electrodes. The inductance of the coils change its value when the inside material changes, or in other words when the magnetic permeability changes. If the permeability changes, the inductance changes and also the induced voltages in the coil detectors. In some experiments [27] the variation in the induced voltages has been used to calculate the velocity of bubbles for two-phase flow measurement.

2.5 Two Phase Liquid Separation

Traditionally the measurement of oil and water has been made by separating the phases in a test tank and then measuring single phase flows separately. By doing this, the measurement no longer depends on the flow regime, anymore however, continuous measurements can not be made due to the fact that the separation takes an extended time to occur.

A cyclonic separator makes use of centrifugal forces to separate different substances

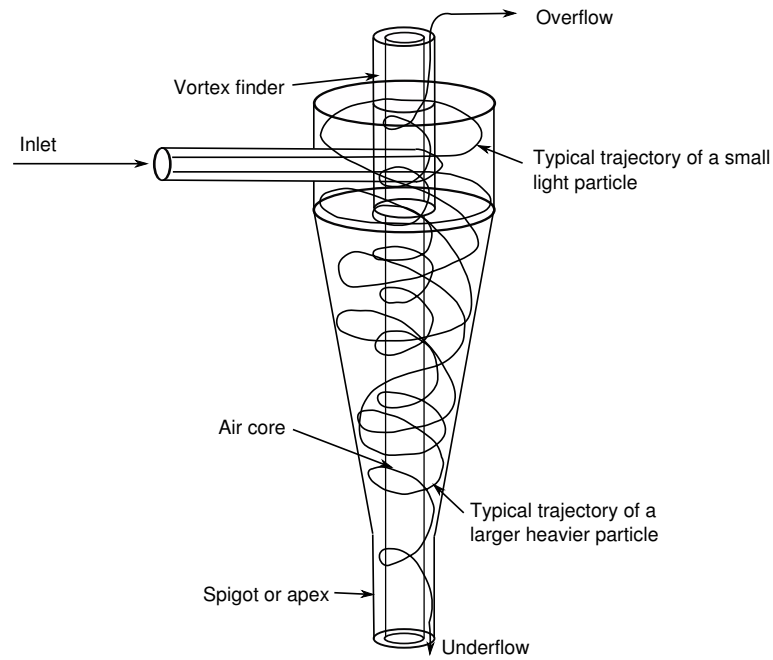


Figure 2.16: Hydrocyclone operating principle

by weight or by differences in density. The first patent for a cyclone appeared in 1885 [28], used for removing dust particles from an air flow (solids from gas). However it was not until the 1940s when this device was used for removing rock from coal, and also in the pulp and paper industry. The success in the mentioned industries was due to the fact that density differences between the particles were very high. The use of cyclonic separators today is wide-spread among many industries, but also in households (cyclonic vacuum cleaners such as Dyson, etc.)

Cyclones can also be used for separating solids from liquids, liquids from liquids, and gases from liquids. In this case, the device is also known as *hydrocyclone*. The simplicity of its design, its versatility, and simple operation, makes the hydrocyclone an ideal candidate for stratifying the multiphase flow needed for the proper operation of the sensor developed in this research.

A generic hydrocyclone features a cylindrical section at the top, followed by a conical section below (see Figure 2.16). When a multiphase flow is injected in the cylindrical



Figure 2.17: Hydrocyclone application for sand filtering

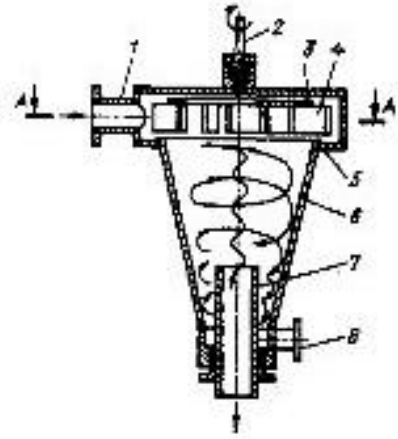


Figure 2.18: Turbocyclone

section, a swirling motion occurs. As a result of this swirling motion, a centrifugal force is exerted on the liquids. As the flows in the multiphase flow mixture have different densities, these flows separate themselves under the application of the centrifugal force, and as a result, the heavier liquid circulates on the outside of the pipe, whereas the lighter one circulates in the middle. The separating hydrocyclones have two outlets, the first one located in the center top part to *bleed* the lighter phase, whereas the heavier phase exits by the second outlet located at the bottom of the cyclone (Figure 2.16). In practice, many different configurations exist according to requirements of the application. Figure 2.17 shows an example of the hydrocyclone application for sand filtering. It may be necessary to apply extra energy to the separation process by means of a turbine (Figure 2.18).

A hydrocyclone is being used in this sensor not to separate the two phases into individual streams, but to convert whatever flow regime exists upstream into a stratified

flow that passes through the sensor. By doing this, the above limitations that current capacitive sensors face can be overcome.

2.6 Conclusion

This Chapter provides an overview of the current state of the art technologies in multiphase sensing and separation. Two types of measurements are considered as part of multiphase flow measurement: the flow velocity measurement and the multiphase flow composition measurement. The sensor developed in this research belongs to the multiphase flow fraction category. The most used principles for multiphase composition sensors are the impedance and the gamma ray sensors. The later sensors are more complex and it is difficult to get real time measurements [29]. The impedance technique has been used for many sensors because of its simplicity, robustness, dynamic response and safety compared with radiation methods. However this technique is sensitive to flow regime, changes in electrical properties and the inversion point [30]. In conclusion, there is no “ideal” multiphase flow meter available today and different error tolerances in measurements are allowable depending on the purpose of the measurements. The characteristics of flows may drift over time or may be affected by the speed, composition or geometry of the pipeline. Such variability in flow regimes makes the multiphase measurement a complicated task. The MPFM currently available uses different approaches to overcome these challenges, but none has yet fully satisfied the requirements demanded by the industry. One of the goals in this research is to improve the field of multiphase measurement by using a unique combination of electro-hydro-mechanical devices.

Chapter 3

Proposed Measurement Method

3.1 Stratified Flow Regime in a Rectangular Measurement Chamber

The previous Chapter outlined the techniques employed in multiphase flow metering. It was also mention that the impedance method is characterized by its simplicity and robustness. Some of the drawbacks of this method is the flow regime dependency. In order to reduce the flow regime dependency, the method proposed in this work separates the flow temporarily by using centrifugal force, i.e. the same way a hydrocyclone operates. The stream of liquid mixture is fed tangentially into the funnel-shape chamber, and the heavier phase is collected near the outer wall, while the lighter phase drifts toward the center in the separation chamber (Figure 2.16). If this separation chamber is instrumented with a capacitive sensor array, a simple, less constrained solution for multiphase measurement is obtained.

This section presents an analysis of the proposed system using an analytical method on two simplified models. Finally, a FEA analysis is presented on a practical prototype. The initial focus is placed on stratified flows being established in the measurement

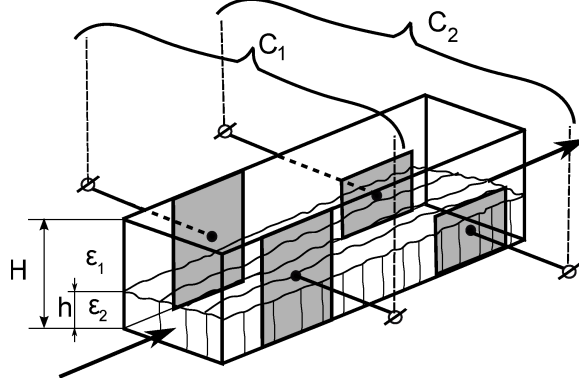


Figure 3.1: Capacitive level measurement - parallel configuration

chamber. The first analysis presents the case of a horizontal pipe segment of rectangular cross-section, illustrated in Figure 3.1. If two parameters, the composition $\alpha = h/H$ and the permittivity ε_1 are to be determined, two linearly-independent measurements are needed. For each additional parameter (unknown), one additional, linearly-independent from others, measurement is required.

3.1.1 Linear Independence of the Measurement

It is a well known fact that two unknown variables can be determined from two equations (or two measured characteristics) only if they are linearly independent of each other. In other words, only graph lines that are not parallel can produce an intersection point $[X,Y]$ that represents the solution. This also applies to any number of variables but the imagining of higher order surfaces (planes) being linearly independent with each other is not as trivial.

The case of oil and water volume fraction measurement can be illustrated on a glass laboratory beaker containing a layer of water at the bottom part and a layer of oil above. If the total volume (height H and cross area A) is known and the densities are also known (ρ_w, ρ_o), one weight measurement (m) can determine the composition (or interface level H_w , $H_o = H - H_w$) using the following formula:

$$H_w = \frac{\frac{m}{A} - H\rho_o}{\rho_w - \rho_o} \quad (3.1)$$

An interesting situation arises when the density of one of the liquids, say oil, drifts to a new unknown value ρ_o^d . Now, since there are two unknown variables, H_w , ρ_o^d , according to the statement above, two measurements or equations that are linearly independent of each other are needed. This can be arranged by mixing two different compositions H_{w1} , H_{w2} and maintaining the same total level H (volume) in both beakers that undergo weight measurement (m_1 , m_2). This is more of an illustration rather than a practical case since the relationship between the two compositions needs to be known, for example “*one beaker contains twice more water than the other beaker*”, otherwise three unknowns (H_{w1} , H_{w2} , ρ_o^d) and two weight measurements will be obtained. Increasing the number of beakers will not help as this always introduces one additional unknown parameter for every additional beaker.

The next subsections shows why changing the aspect ratio (H and /or A) can not lead to a solution of the problem, and also presents the proposed solution.

3.1.2 Parallel-Capacitor Configuration

Figure 3.1 shows two parallel plate capacitors of dissimilar heights that operate in parallel-capacitor configuration $C_1 = C_{1_{\epsilon_1}} || C_{1_{\epsilon_2}}$ and $C_2 = C_{2_{\epsilon_1}} || C_{2_{\epsilon_2}}$. This system is often used in 3-phase level sensors. Despite the linear independence of capacitances with α and ϵ , the sensor can not accommodate variations in composition α from 0% to 100% as the electrode-pair C_2 height is less than the total height H . Having just a small electrode height discrepancy would not solve such a problem due to the increased uncertainty of the measurement and lack of accuracy. Also, channeling the flow through a rectangular pipe of a different aspect ratio, or varying the electrode

width rather than height will only result in a set of linearly dependent measurements.

3.1.3 Series-Capacitor Configuration

A different configuration of pipe and electrodes for measuring flow is described by Wael and Basel [21]. This configuration employs concave plates clamped on a circular pipe, (see Figure 2.11) this type of sensor does not completely encompass the 0% to 100% range of α . A series-capacitor configuration array as illustrated in Figure 3.2 can be used to establish a set of linearly-independent measurements; however, this array is also associated with the above-mentioned problems, plus one electrode obstructs the flow. This situation may be solved by moving the plate outside and inserting a known dielectric plate of a specified height underneath. The disadvantage of doing this is that in series-capacitor configuration systems, large spacings between electrodes pose a challenge in the detection of small capacitances.

3.1.4 Summary of Currently in use Methods and Proposed Electrode Configuration

In summary, despite many drawbacks, all the above-mentioned methods would operate in a restricted range of α . In fact, the concentric ring electrode system described in [22] may be well adapted for the measurement to span the full range of α . Large difficulties

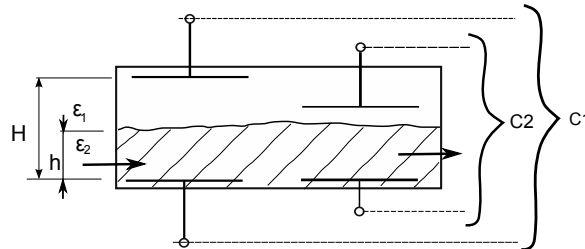


Figure 3.2: Series capacitor configuration level measurement

are however associated with gravity-type horizontal pipe flow stratifier. Multiphase flows often require a long segment of a horizontal pipe that provides enough time for phases to settle down and be separated by gravity. Friction and dents on the pipe walls create turbulences that make the phase separation under rapid flow velocities of $5 - 10 \frac{m}{s}$ flow conditions even more difficult. That is why in industry, large-sized expensive separators are used to slow down the stream significantly. In this research, it was found that the use of a hydrocyclone as part of a sensor, leads to a set of linearly independent equations. A hydrocyclone utilizes the kinetic energy of the multiphase stream plus the gravity to stratify the flow, i.e. to layer the flow coaxially. The stream, fed tangentially into the cyclone of a funnel shape, spins in a helical spiral thus creating centrifugal forces [3] that, combined with the gravity, separates the phases by density. The heavier phase, such as water, is collected near the outer

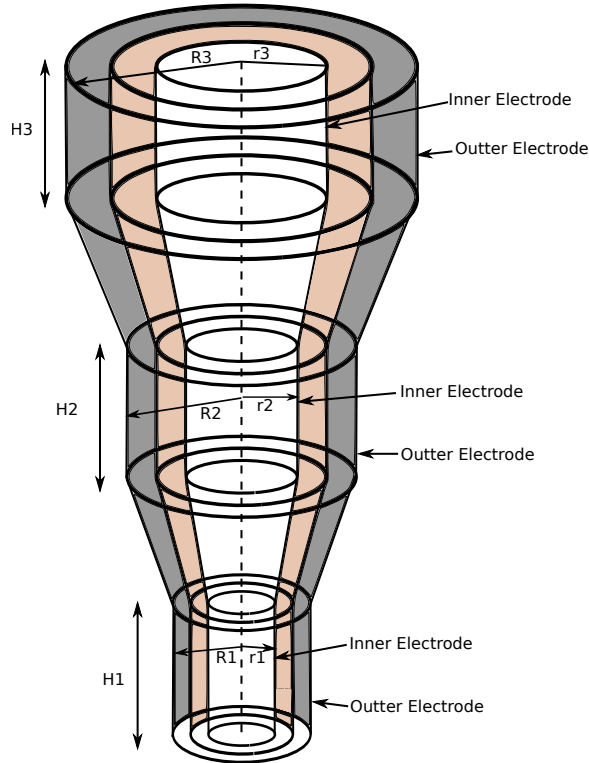


Figure 3.3: Hydrocyclone instrumented with three pairs of electrodes.

wall while the lighter phase, such as oil, drifts towards the centre. If a cyclone is instrumented with a capacitive sensor array, a simple and less constrained solution for multiphase measurement can be found (Figure 3.3).

In the following section, presents the analysis of the proposed system using two analytical and one numerical (FEA) models. The hydrocyclone modulates the depth (or height) of the interface layer between water and oil along the hydrocyclone vertical axis which is key in obtaining the linearly-independent characteristics.

3.2 Sensor Analysis

The solution of a large group of problems in electrostatics is to find a potential distribution that satisfies the Laplace equation with a given electrode geometry and electrode voltages. In order to analytically derive the capacitance of a two electrode array, the following assumptions are considered:

1. Electric fields inside the conductors are negligible due to small current flows; therefore, the conductor surface is an equipotential surface.
2. The boundary between two dielectrics is considered to coincide with the equipotential surface i.e. a two-dielectric capacitor can be dissected into two capacitors of single dielectric constant that are connected in series.
3. Electrodes added in the practical system to act as shields or guards to control fringing flux, reduce unwanted stray capacitance and shield against unwanted pickup of external electric fields are not considered.
4. Fringe capacitance and stray capacitance is neglected.
5. Unwanted capacitive coupling between multiple electrode pairs, the crosstalk, is neglected.

In addition to the above assumptions, consider the cross-section area of the measurement chamber cavity to be constant along the axial direction. This is not necessary for the function of the sensor; however, it maintains the axial flow velocity to be constant along the cyclone's longitudinal dimension.

Two analytical models to verify the sensor feasibility are presented. In the first model, small segments of cylindrical electrodes are considered as planar parallel-plate capacitors. The objective of the first model is to show the non-linear distribution of the dielectric boundary across the array elements that translates into the required set of linearly-independent equations. In the second model, more realistic concentric cylindrical electrodes are considered to show additional non-linearity that translates into an increased measurement robustness. Both models are also geometrically adjusted such that the funnel-shaped cyclone has cylindrical electrodes. In the actual sensor however, cone segment electrodes will be installed to mitigate the flow 'bending' and discontinuity. This case is studied by FEA analysis in section 3.3.

3.2.1 Parallel Plate Electrode Model

In the first approximation, assume that the aspect ratio $\frac{R_i - r_i}{r_i}$ is small enough to consider the concentric cylinder electrodes or their segments as parallel plate capacitors, which is shown in Figure 3.4a. Since the following analysis is not concerned with the absolute capacitance but rather the relative changes across the array, the product, $\epsilon_0 A$, of the parallel plate capacitance is set to unity.

The objective of this analysis is to prove the sensor's working principles for which the optimized design of the cyclonic stratifier is not critical. It will be shown that for any dissimilar radii pair $r_1 \neq r_2$ it can be obtained a unique solution for this problem. By selecting three design parameters r_1 , R_1 and r_2 , R_2 can be calculated from the constant cross-section area condition set above as

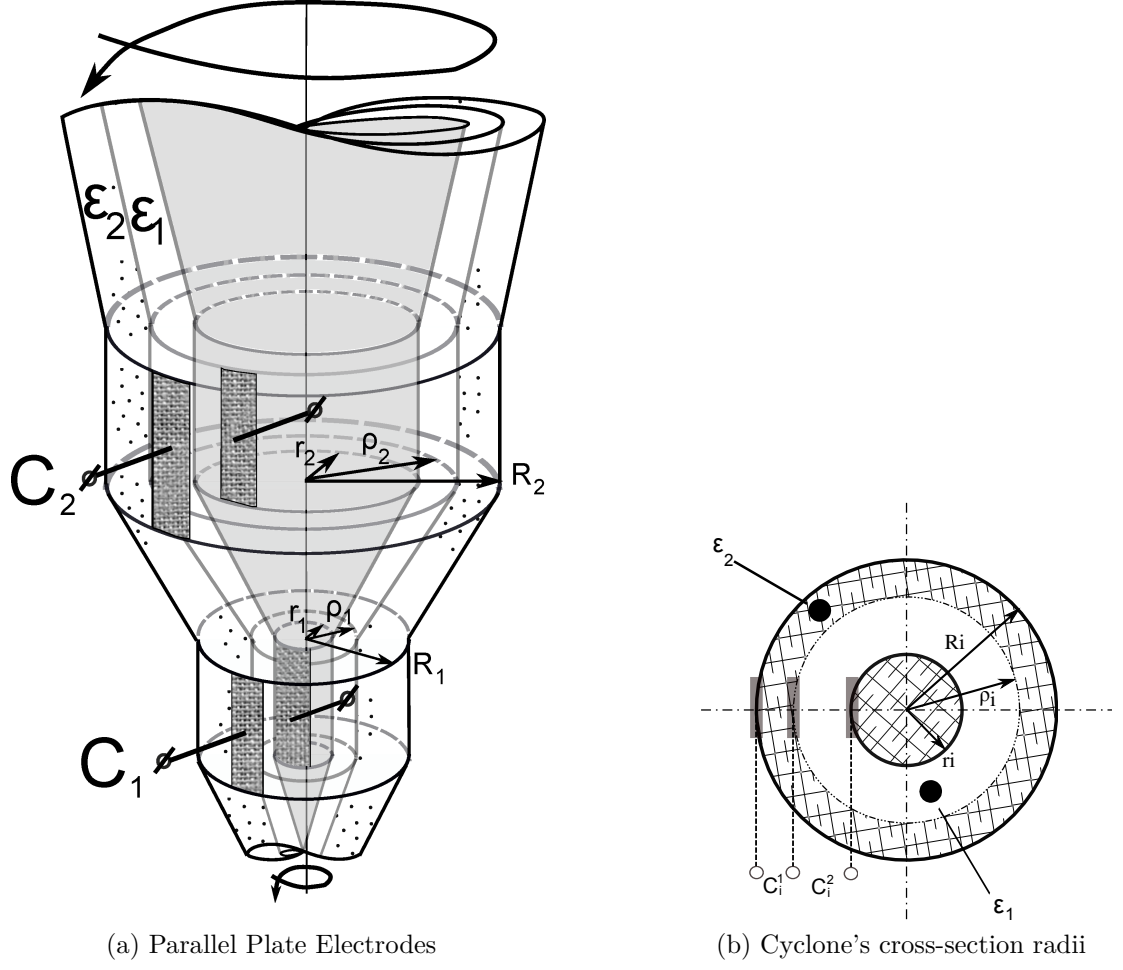


Figure 3.4: A cyclonic capacitive sensor with parallel plate electrodes. R_i Designates the outer radii, whereas r_i designates the radii of the inner core, and ρ_i is the radii of the oil/water interfaces.

$$R_2 = \sqrt{\frac{A_\phi}{\pi} + r_2^2} \quad (3.2)$$

where

$$A_\phi = \pi(R_1^2 - r_1^2) \quad (3.3)$$

then, the electrode pair capacitance C_1 and C_2 can be calculated as

$$C_i = \frac{C_i^1 \cdot C_i^2}{C_i^1 + C_i^2}, \quad i = 1, 2 \quad (3.4)$$

where

$$C_i^1 = \frac{\varepsilon_0 \varepsilon_1 A}{\rho_i - r_i}, \quad C_i^2 = \frac{\varepsilon_0 \varepsilon_2 A}{R_i - \rho_i} \quad (3.5)$$

as seen in Figure 3.4b.

This evaluates to

$$C_i = \frac{\varepsilon_0 \varepsilon_1 \varepsilon_2 A}{\varepsilon_1 (R_i - \rho_i) + \varepsilon_2 (\rho_i - r_i)} \quad (3.6)$$

where: r_1 corresponds to the radii of the internal electrode (r_1 is the bottom and r_2 is the top) and R_1 corresponds to the radii of the external electrode, according to the Figure 3.4b. The composition α , assumed constant across the array, is defined as a volumetric ratio of dielectric ε_1 to the total volume of dielectrics ε_1 plus ε_2 , thus

$$\alpha = \frac{A_{\varepsilon_1}}{A_{\phi}} = \frac{\rho_i^2 - r_i^2}{R_i^2 - r_i^2}, \quad i = 1, 2 \quad (3.7)$$

from which the formula for the dielectric interface radius ρ_i (Figure 3.4b) in terms of α is derived as

$$\rho_i = \sqrt{\alpha(R_i^2 - r_i^2) + r_i^2}, \quad i = 1, 2 \quad (3.8)$$

In the water-oil mixture sensing application, the watercut (% of ε_2 phase) is obtained as $\alpha_w[\%] = 100[\%] - \alpha[\%]$.

Both capacitances C_1 and C_2 can then be expressed in terms of phase permittivities ε_1 and ε_2 , and the composition α by substituting Eq. 3.8 into Eq. 3.6:

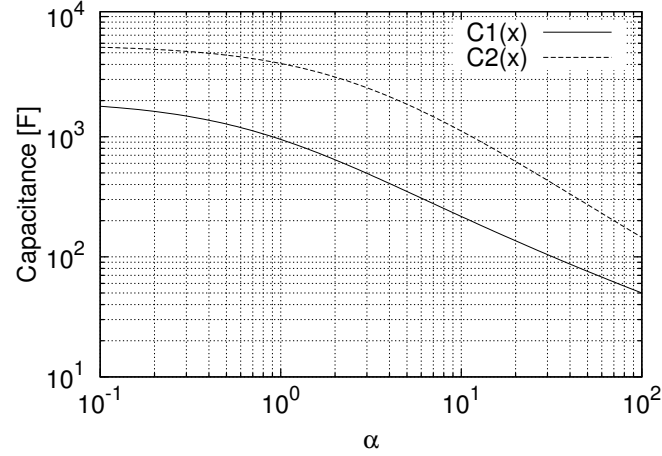


Figure 3.5: $C_i = C_i(\alpha\%)$, $i = 1, 2$, $\varepsilon_1 = 2.0$, $r_2 = 8 \times r_1$

$$C_i = \frac{\varepsilon_0 \varepsilon_1 \varepsilon_2 A}{(\varepsilon_2 - \varepsilon_1) \sqrt{\alpha(R_i^2 - r_i^2) + r_i^2} + \varepsilon_1 R_i - \varepsilon_2 r_i} \quad (3.9)$$

As an example, consider the following parameters and obtain the characteristics plotted using logarithmic scales in Figures 3.5, and 3.6.

$$r_1 = 0.01[m]$$

$$R_1 = 0.05[m]$$

$$r_2 = 2, 4, 8 \cdot r_1 \text{ (three multiples of } r_1 \text{)}$$

$$(\varepsilon_0 A) = 1[Fm] \text{ to simplify the calculation of } C_i$$

$$\varepsilon_1 \in (1.5, 2.5) \text{ range of permittivity (oil)}$$

$$\varepsilon_2 = 80 \text{ constant permittivity (water)}$$

$$\alpha \in (0\%, 100\%) \text{ variable multiphase composition}$$

In a real system, the mixture percentage $\alpha\%$ and the permittivity ε_1 is derived through

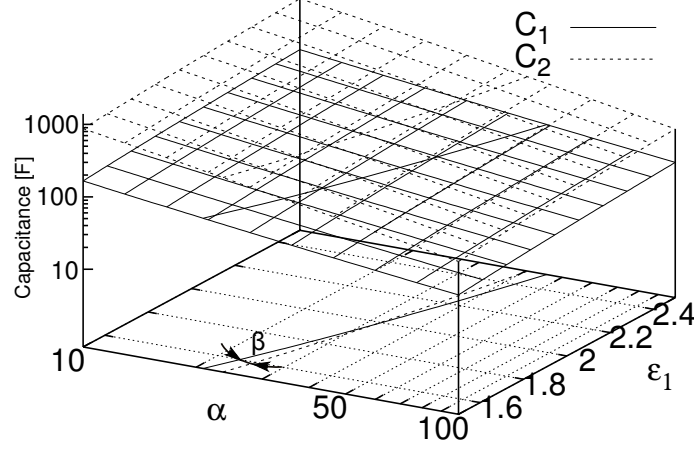


Figure 3.6: $C_i = C_i(\alpha\%, \varepsilon_1)$, $i = 1, 2$, $r_2 = 8 \times r_1$

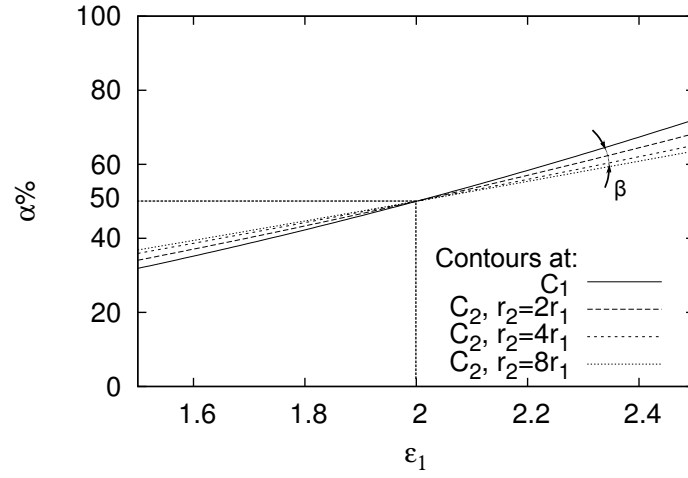


Figure 3.7: Linear disparity as r_2 increases against r_1 .

the following process. First, two capacitances C_1^m and C_2^m are measured. Then, two contour lines $\alpha_i = \alpha_i(\varepsilon_1, C_i^m)$ associated with the measured capacitance C_i^m as shown in Figure 3.6 are derived as:

$$\alpha_i = \frac{\left[\frac{\varepsilon_0 \varepsilon_1 \varepsilon_2 A}{C_i} - \varepsilon_1 R_i + \varepsilon_2 r_i \right]^2 - (\varepsilon_2 - \varepsilon_1)^2 r_i^2}{(\varepsilon_2 - \varepsilon_1)^2 (R_i^2 - r_i^2)} \quad (3.10)$$

The two characteristic curves must be linearly independent in order to extract the desired parameters α and ε_1 . In other words, the two contours projected into the $\alpha \angle \varepsilon_1$

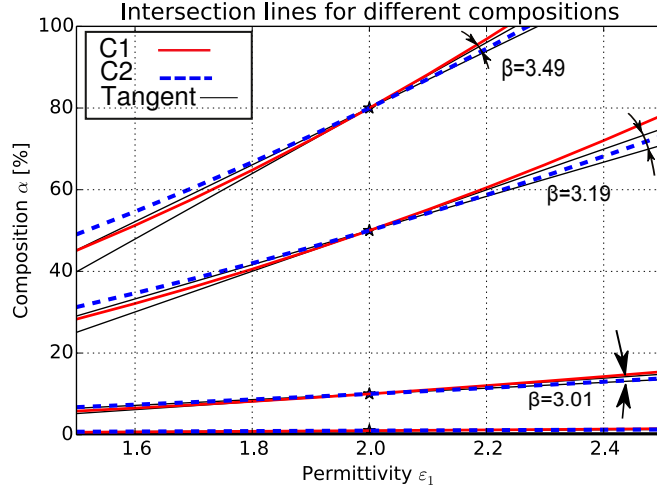


Figure 3.8: Model 1. The intersection angles for different values of α .

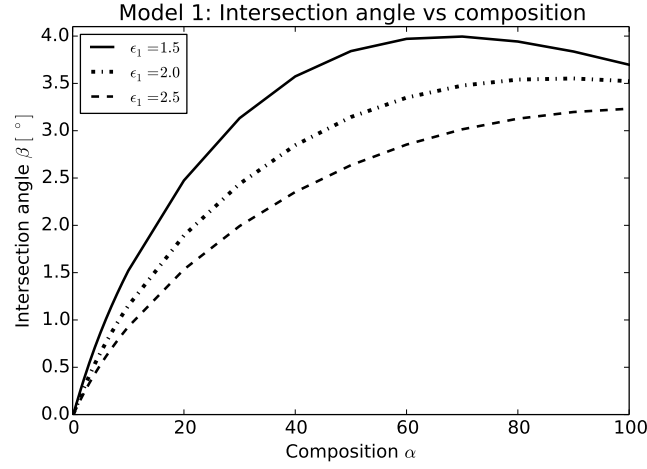


Figure 3.9: Model 1. The intersection angles as a function of composition and ε_1 .

plane (Figure 3.6) must intersect at the angle β within a practical region. Figure 3.7 shows this process for three r_2 radii set as multiples of r_1 . The intersection angle β of these curves is a function of the ε_1 and the composition α as is shown in Figures 3.8 and 3.9. By analyzing these figures, it can be observed that the intersection angle β increases with composition α . At low compositions α , the measurement uncertainty

of α is very small as the individual characteristic curves are nearly parallel with the abscissa. The permittivity parameter ε_1 would however have a large uncertainty due to the small angle β . The practical range on the oil-gas industry starts at 10% of hydrocarbons in the well stream and thus large uncertainty in ε_1 is not limiting. Moreover it is the composition α which is the main parameter provided by currently installed sensors and is required by the industry.

3.2.2 Concentric Cylindrical Electrode Model

In the second approximation, the funnel shape cyclone was considered to be piece-wise smooth again but having concentric ring electrodes as shown in Figure 3.10. By following the steps from the previous model, it will be shown that this model features higher degree of robustness with less uncertainty.

Adopting the same conventions and indexing format from the previous model analysis, the partial capacitances C_i^1 and C_i^2 can be calculated as

$$C_i^1 = \frac{2\pi\varepsilon_0\varepsilon_1 h}{\ln \frac{\rho_i}{r_i}}, \quad C_i^2 = \frac{2\pi\varepsilon_0\varepsilon_2 h}{\ln \frac{R_i}{\rho_i}}, \quad i = 1, 2 \quad (3.7')$$

where h is the height of the electrodes. The total capacitances C_i evaluate to

$$C_i = \frac{2\pi\varepsilon_0\varepsilon_1\varepsilon_2 h}{\ln R_i^{\varepsilon_1} r_i^{-\varepsilon_2} \rho_i^{\varepsilon_2 - \varepsilon_1}} \quad (3.8')$$

or equivalently in terms of the composition α to

$$C_i = \frac{2\pi\varepsilon_0\varepsilon_1\varepsilon_2 h}{\ln \{ R_i^{\varepsilon_1} r_i^{-\varepsilon_2} [\alpha(R_i^2 - r_i^2) + r_i^2]^{\frac{\varepsilon_2 - \varepsilon_1}{2}} \}} \quad (3.11')$$

Figure 3.11 shows the plot of Eq. 3.11'. The two contours $\alpha_{1,2} = \alpha_{1,2}(\varepsilon_1)$ associated

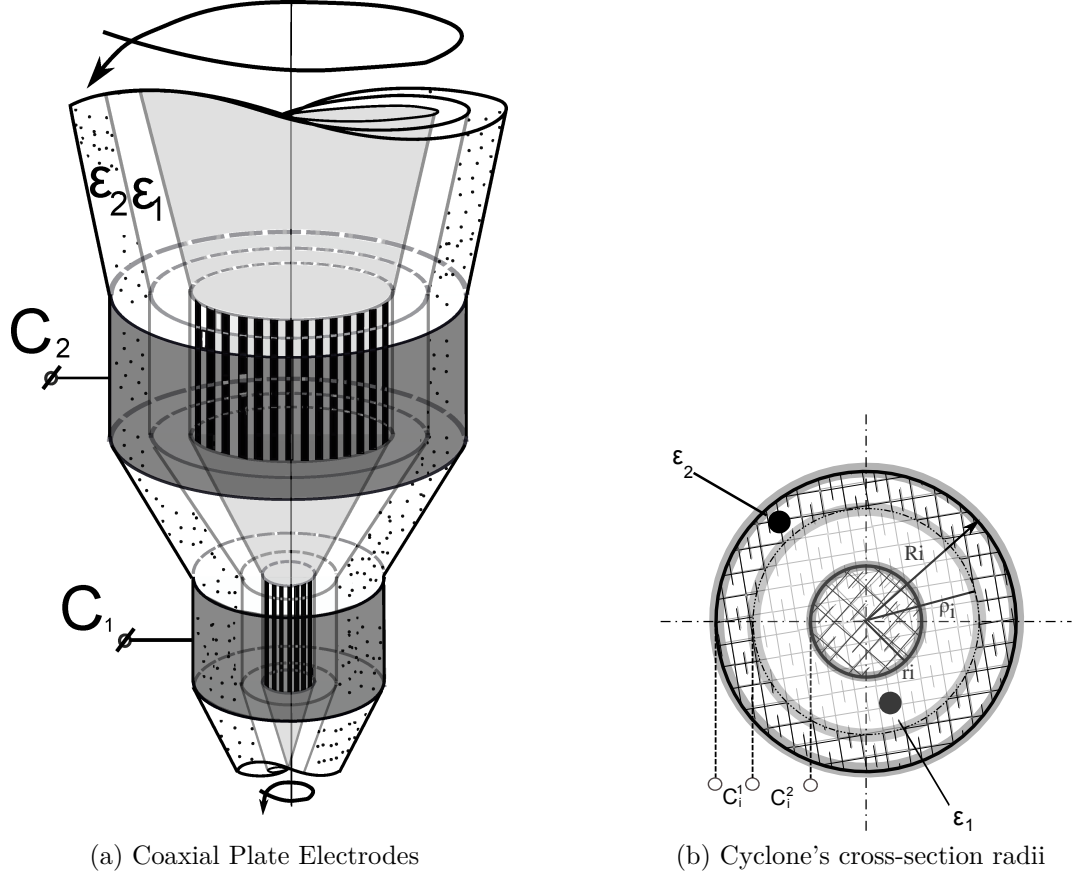


Figure 3.10: A cyclonic capacitive sensor with coaxial plate electrodes

with each corresponding capacitance ($C_{1,2}$) are derived as

$$\alpha_i = \frac{\left(r_i^{\varepsilon_2} R_i^{-\varepsilon_1} \exp\left\{ \frac{2\pi\varepsilon_0\varepsilon_1\varepsilon_2 h}{C_i} \right\} \right)^{\frac{2}{\varepsilon_2 - \varepsilon_1}} - r_i^2}{R_i^2 - r_i^2} \quad (3.12')$$

Comparing the characteristics of linear independence in terms of three different radii r_2 (Figure 3.12) it can be concluded that the ring electrode model (Figure 3.10) features better robustness as larger intersection angles β (Figures 3.13 and 3.14 vs Figures 3.8

and 3.9) lead to less uncertainty in the measurement.

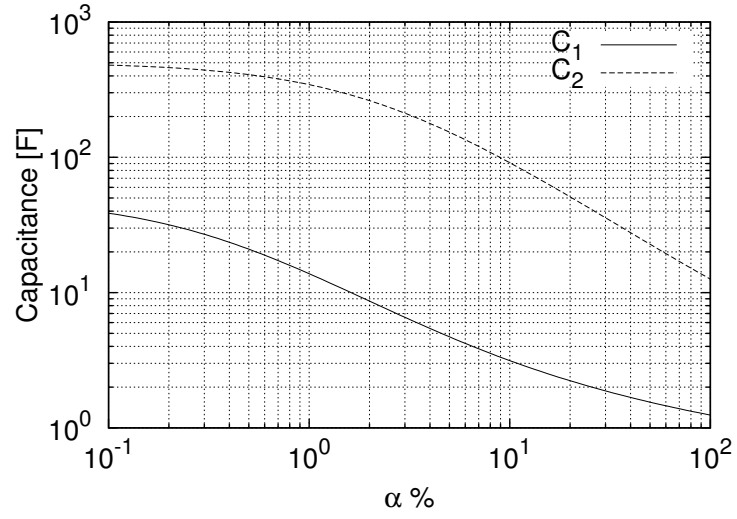


Figure 3.11: $C_i = C_i(\alpha\%)$, $i = 1, 2$, $\varepsilon_1 = 2.0$, $r_2 = 8 \times r_1$

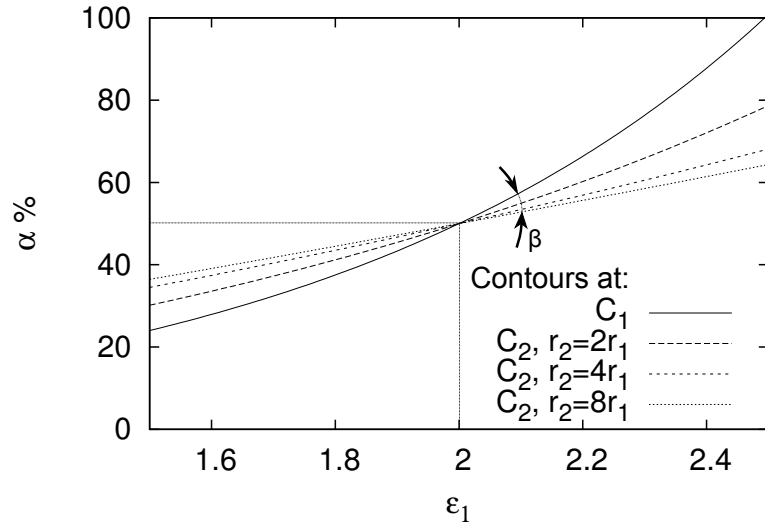


Figure 3.12: Linear disparity as r_2 increases against r_1 .

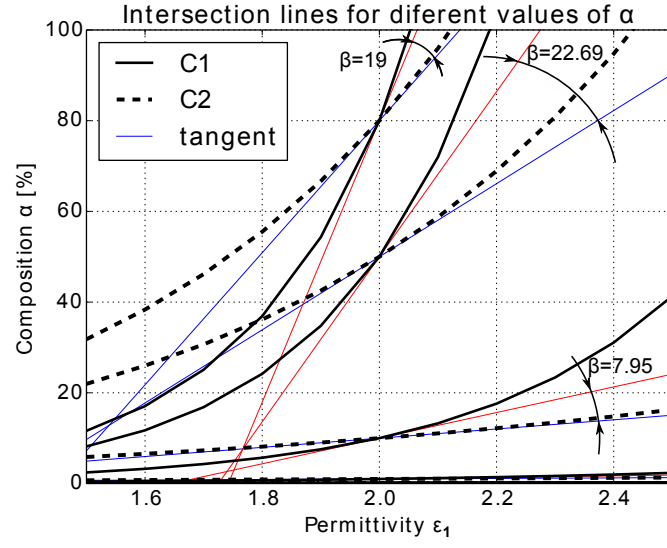


Figure 3.13: Model 2. Intersection angles for different values of α .

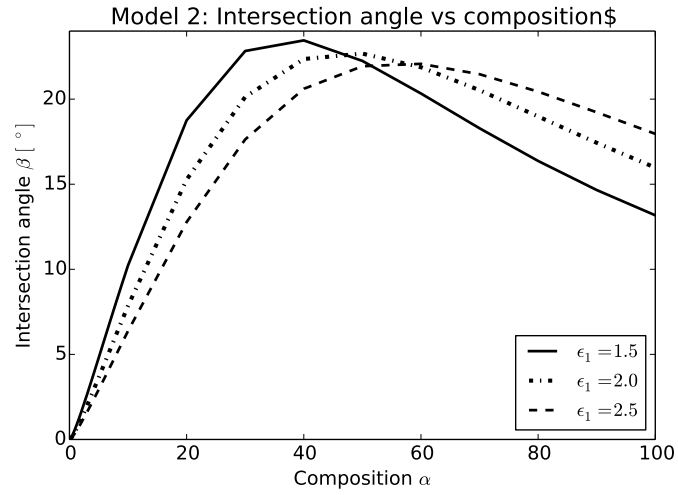


Figure 3.14: Model 2. The intersection angles as a function of composition and ϵ_1 .

3.3 FEA Analysis of a Prototype

The above section demonstrated that the sensor can achieve a level of linear independence and robustness by monitoring the parameter ε_1 drift. The robustness of this sensor can be improved by adding one additional electrode. The sensor with three electrodes can accommodate variations not only in the composition and the oil permittivity, but in the water permittivity as well. The considered model is comprised of three conical electrodes for capacitance measurement separated by two guard electrodes as shown in Figure 3.15.

Since the complexity of this sensor is greater than in the previous models, a computer simulation model was developed. The selected FEA software was the Finite Element Method Magnetics FEMM [31], which is used mainly to solve electromagnetic problems, but this software also has electrostatics solvers as well.

In this model, the three internal electrodes are mounted on a center cone. In this model the outer wall for the liquid is assumed to be made of a conductive material.

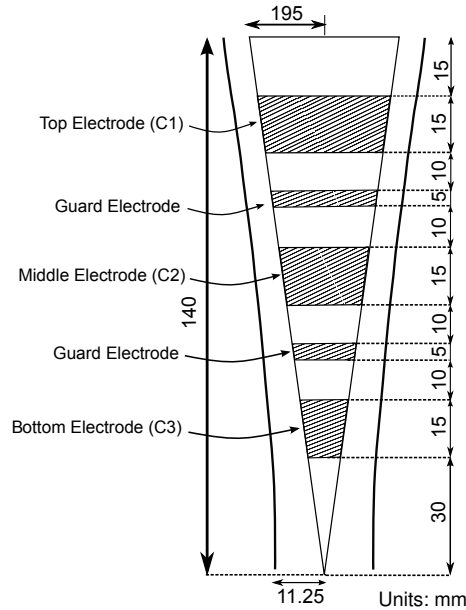


Figure 3.15: Configuration of the internal cone for a three electrode sensor

This wall also works as a second electrode that is common to all three capacitors. In order to work properly, this wall is supposed to be at zero potential, i.e. grounded. The total length of this sensor is 140mm, the physical dimensions of the electrodes are shown in Figure 3.15. In order to maintain a constant cross sectional area between the electrodes and the wall, since the inner electrodes are mounted on a cone, the radii of the outer electrode or wall must satisfy the Eq. 13:

$$R2 = \sqrt{11.25^2 + \left(\frac{h * 19.5}{140}\right)^2} \quad (13)$$

By satisfying this equation the transversal view of the sensor shows that the wall has a hyperbolic profile that can be seen on the same figure.

In these simulations, an intermediate wall surrounding the cone was added. In the simulations, this wall was the interface between the oil and the water. The thickness of this layer covering the inner core, was changed between 0% and 100% in steps of 1%. For every thickness of the oil layer, the three capacitances values were calculated and stored. The oil permittivity values were changed between 1.5 and 3.0 in steps of 0.1. The water permittivity values were changed between 75 and 90 in steps of 1. The capacitance calculations were repeated for every combination of water and oil permittivities. The capacitance values were stored for future use during the calibration of future prototypes.

The computer model allowed us to calculate the capacitances of the three electrodes for different values of oil permittivities, water permittivities and multiphase composition. Figure 3.16 shows the variations in the capacitances of the three electrodes when the water permittivity has a value of 80, for different oil permittivity values and compositions.

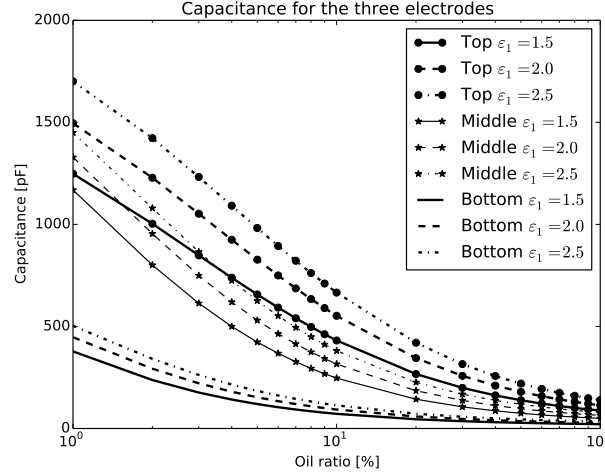


Figure 3.16: Capacitance for different composition and oil permittivities when $\varepsilon_w = 80$.

3.3.1 Measurement Process Analysis

The idea for using the data calculated during the previous simulation is as follows. When a multiphase stream flows through the sensor, the capacitances C_1^m, C_2^m, C_3^m are acquired. The capacitance for the first electrode C_1^m is entered into a computer program. This program generates a matrix of all of the possible combinations of oil permittivity, water permittivity and composition that will produce the same value of capacitance, based on the data obtained from the computer simulations. In order to compare the numerical model with the previous analysis, the case using only the top and the bottom electrode will be considered first. In this analysis the water permittivity is considered constant with a value of $\varepsilon_2 = 80$. The intersection angles for different compositions are shown in Figure 3.17, and the variation of the intersection angle as function of composition in Figure 3.18.

When three electrodes are used, the measured capacitance values are fed into a computer program. The computer program will generate a matrix of all of the $\varepsilon_o, \varepsilon_w$, and α combinations that will give the same value of capacitance. The capacitance can be

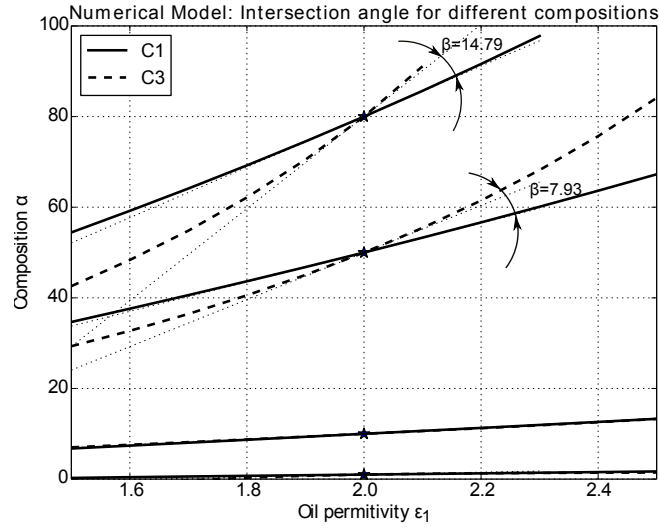


Figure 3.17: Intersection angles in the plane $\epsilon_1 - \alpha$

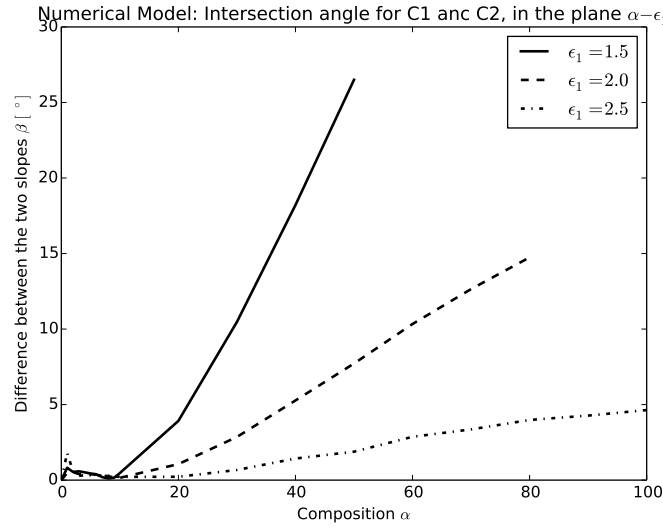


Figure 3.18: Intersection angles as a function of composition for different values of ϵ_1 .

visualized as a surface, in which every point is a combination of the three variables. There will be three different surfaces, one for each electrode. These surfaces intersect each other at curves (loci). These curves eventually intersect in a single point. The coordinates of that point in which the three surfaces intersect each other, represent

the parameter combination of the mixture that was flowing during the measurement. As a test, the capacitance values for a mixture of $\varepsilon_0 = 2.9$, $\varepsilon_w = 86$ and $\alpha = 1\%$ were processed in the manner that was described in the analytical model above. The surfaces generated with the previously described method are shown in Figure 3.19. On each surface a line representing a composition of 1% has been drawn, and the projection of these lines indicates that they indeed intersect in a solution point. From the projected lines redrawn in Figure 3.20, it can be seen that the intersection occurs for the values of $\varepsilon_o = 2.9$ and $\varepsilon_w = 86$ which are the data used initially.

3.4 Conclusion

In this chapter, two analytical models and a numerical FEM model were studied. All models demonstrated an increased level of robustness in the order of model presentation. The robustness accounts for drift in individual phase parameters, the permittivity ε in this case. This type of sensor does not require previous separation of the multiphase flow, and can be used for the full range 0%-100% of oil water composi-

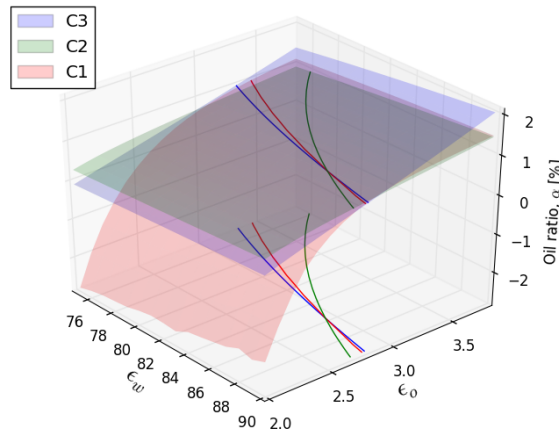


Figure 3.19: Surfaces with the same capacitance

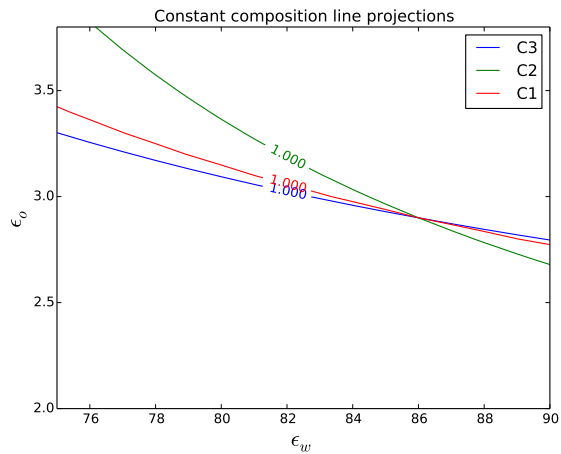


Figure 3.20: Lines with the same composition from different electrodes

tions. The obtained results suggested that the proposed method can be implemented in a prototype. The implemented prototype and its tests will be shown in the next chapter.

Chapter 4

Dielectric Measurement

4.1 Introduction

The developed capacitance sensor measuring multiphase composition is based upon variation of the relative permittivity (the dielectric constant) of the multiphase mixture. The dielectric behavior of a material is characterized by two parameters, one providing a measure of the electric field energy storage capability (capacitance) and the other a measure of the energy dissipation of the material (resistance). The permittivity and conductivity (inverse resistance) of water are much higher with respect to those of oil and gas. This large discrepancy enables the multiphase composition measurement.

Most practical capacitance sensors used today work in a frequency range up to 30MHz; the low frequency in a range of 30kHz to 300kHz, the medium frequency in a range of 300kHz to 3MHz, and the high frequency range from 3MHz to 30MHz. Some sensors also utilize the microwave frequencies in ultra and super high frequency range of 0.3GHz to 30GHz. Since most of the function generators available have a maximum frequency of 3MHz, it was decided to work at a medium frequency.

The dielectric behavior of a material is represented by a complex permittivity that is a function of the frequency. Both water and oil complex permittivities are listed in the Appendix B. At the medium frequency range, the imaginary part can be neglected and the relative permittivity as a function of frequency can be obtained through the measurement of capacitance.

This Chapter describes this study's measurement of the dielectric constant in order to confirm the parameters and processes used in the sensor analysis. The relative permittivities were determined from the measurement of capacitance. The effect of the water phase resistance (conductance) was avoided by using insulated electrodes in the chosen measurement setup.

4.2 Apparatus for the measurement of dielectric constant

A sample volume of the fluidum upon testing has to be inserted between two electrodes of sufficient area in order to measure the resulting capacitance in practical ranges. Such a system can undertake various forms but the most frequently used apparatus are either a parallel plate capacitor or a cylindrical capacitor. In the parallel plate capacitor, the resulting electrostatic field strays away from the sample volume along all four sides (edges) of the electrodes. Closer the plates are spaced together relative to their size, the smaller the stray effect is being observed. In case of using the cylindrical capacitor, only two sides exhibit the stray effects. The cylindrical apparatus was also easier to make in the glass blowing shop at Memorial Univesity.

In order to get a consistent insulation layer, a scientific pyrex glassware to insulate the electrodes from a potentially conductive dielectric was used. The resulting apparatus takes a shape of a cylindrical annulus to hold the sample volume in between two

cylindrical glass walls. The dimensional stability of the dielectric spacing between the walls was not as accurate as it was requested initially ($< \pm 0.1\text{mm}$), however, it still enabled to conduct the required experiments for this research. The electrodes were made of a brass shim stock material coiled into a cylinder, one on the outside wall and the other on the inside wall. The apparatus is shown in Figure 4.1 with dimensions listed in table below.

Inside Diameter of Inner Wall	104.0 mm
Outside Diameter of Inner Wall	110.0 mm
Inside Diameter of Outer Wall	119.3 mm
Outside Diameter of Outer Wall	125.5 mm
Cylindrical Annulus Height	100.0 mm
Electrode Height	80.0 mm

Table 4.1: Apparatus dimensions

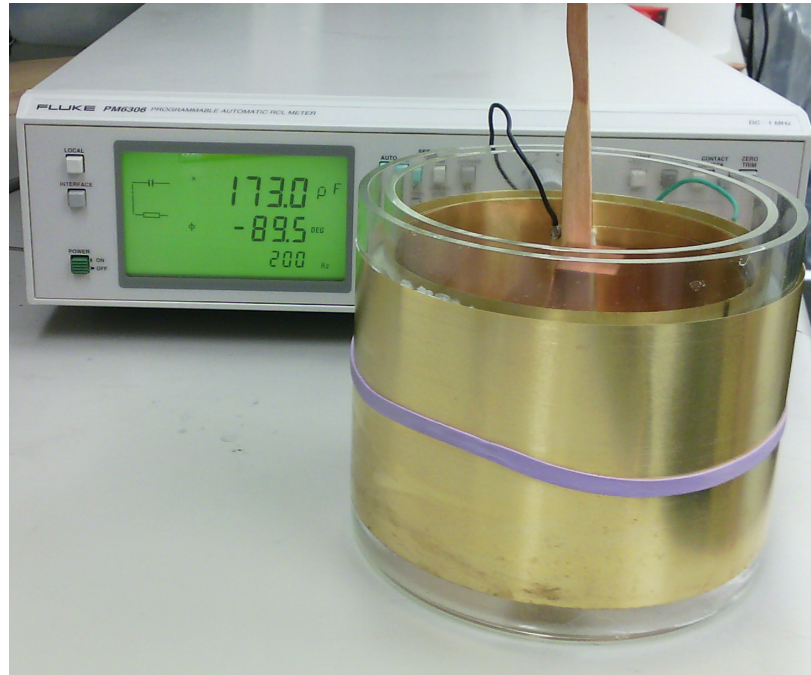


Figure 4.1: Experimental apparatus

4.3 Experiment

In order to determine the permittivity of the material under study, the capacitance was measured by using a Fluke LCR meter model PM6306, then the permittivity was calculated from the capacitor's formula. A series of three measurement runs, each separated by 24 hours, were conducted and then averaged for the purpose of extracting the dielectric constant - the permittivity. Each run spanned four decades of the frequency range between 200Hz and 800kHz. Figure 4.2 portrays the concept of the measurement.

The measured capacitance data of the outer glass wall, air, tap water and mineral oil are listed in Tables 4.2 - 4.5 as well as in a graph format in Figures 4.3 - 4.6. The measurement data also list the impedance angle. Since the electrodes are well insulated from the dielectricum under study, the impedance angle observed was near 90 degrees which constitutes the ideal capacitance case where the capacitive reactance is the only component of the total impedance.

The formulas used in calculating the permittivity of the measured dielectricum ϵ_X are derived for the case of cylindrical capacitors connected in series. Capacitances

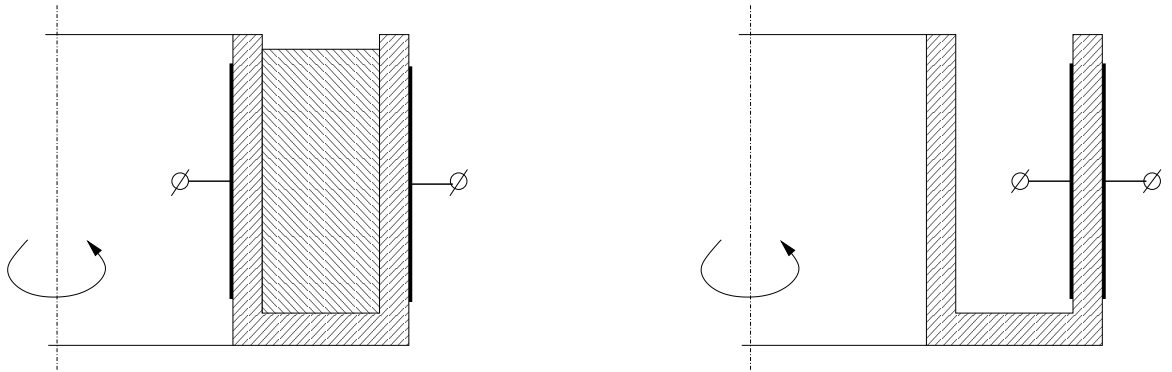


Figure 4.2: Capacitance measurement: (left) total capacitance with a given dielectric contained between the glass walls, (right) glass wall dielectric

Freq[Hz]	$C^1[pF]$	$\phi^1[^\circ]$	$C^2[pF]$	$\phi^2[^\circ]$	$C^3[pF]$	$\phi^3[^\circ]$	$C^{av}[pF]$
2E2	372.8	-89.6	368.3	-89.6	363.2	-89.6	368.1
4E2	371.7	-89.6	367.3	-89.7	362.2	-89.7	367.1
8E2	370.9	-89.6	366.4	-89.7	361.3	-89.7	366.2
2E3	369.8	-89.7	365.3	-89.7	360.3	-89.7	365.1
4E3	369.0	-89.7	364.6	-89.7	359.6	-89.8	364.4
8E3	368.3	-89.8	363.88	-89.8	358.92	-89.8	363.7
2E4	367.3	-89.8	363.04	-89.8	358.10	-89.8	362.8
4E4	366.6	-89.8	362.38	-89.8	357.46	-89.8	362.1
8E4	366.0	-89.5	361.88	-89.8	356.97	-89.8	361.6
2E5	365.1	-89.1	361.1	-89.8	356.2	-89.8	360.8
4E5	364.1	-88.4	360.1	-89.9	355.3	-89.9	359.8
8E5	361.5	-86.7	358.1	-89.9	353.4	-89.9	357.7

Table 4.2: Glass wall - outer

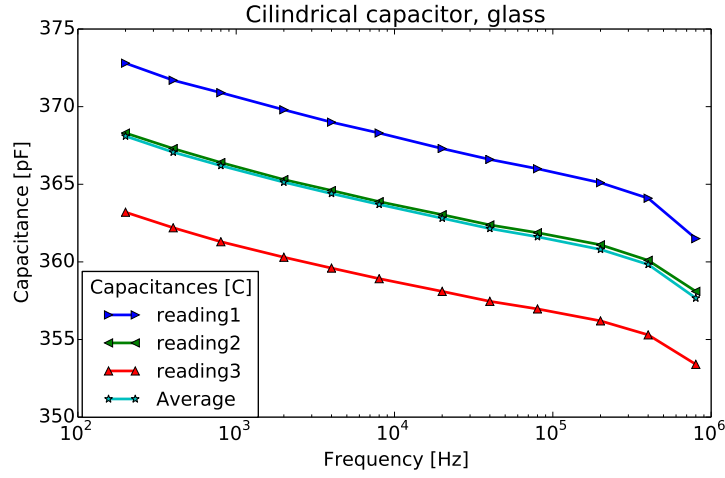


Figure 4.3: Glass wall - outer

Freq[Hz]	$C^1[pF]$	$\phi^1[^\circ]$	$C^2[pF]$	$\phi^2[^\circ]$	$C^3[pF]$	$\phi^3[^\circ]$	$C^{av}[pF]$
2E2	52.0	-89.9	49.4	-89.9	48.3	-89.9	49.9
4E2	51.9	-89.9	49.3	-89.9	48.3	-89.9	49.8
8E2	51.9	-89.9	49.3	-89.9	48.3	-89.9	49.8
2E3	51.8	-89.9	49.3	-89.9	48.3	-89.9	49.8
4E3	51.8	-89.9	49.2	-89.9	48.2	-89.9	49.7
8E3	51.7	-89.9	49.22	-89.9	48.2	-89.9	49.7
2E4	51.65	-90.0	49.18	-90.0	48.15	-90.0	49.7
4E4	51.60	-90.0	49.15	-90.0	48.14	-90.0	49.6
8E4	51.54	-90.2	49.13	-90.0	48.12	-90.0	49.6
2E5	51.45	-91.0	49.08	-90.1	48.06	-90.1	49.5
4E5	51.39	-91.9	48.99	-90.0	47.98	-90.0	49.5
8E5	50.90	-91.5	48.68	-90.0	47.69	-90.1	49.1

Table 4.3: Air dielectric

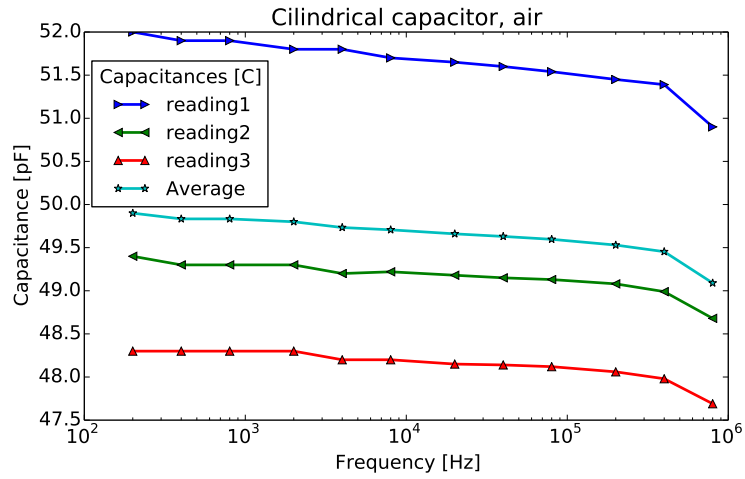


Figure 4.4: Air dielectric

Freq[Hz]	$C^1[pF]$	$\phi^1[^\circ]$	$C^2[pF]$	$\phi^2[^\circ]$	$C^3[pF]$	$\phi^3[^\circ]$	$C^{av}[pF]$
2E2	184.1	-89.6	192.0	-89.5	187.2	-89.8	187.8
4E2	183.5	-89.6	191.4	-89.6	186.4	-89.9	187.1
8E2	183.0	-89.6	190.9	-89.6	185.9	-89.8	186.6
2E3	182.4	-89.7	190.3	-89.7	185.3	-89.9	186.0
4E3	181.8	-89.7	189.8	-89.7	184.8	-89.9	185.5
8E3	181.41	-89.7	189.43	-89.7	184.45	-89.9	185.1
2E4	180.87	-89.8	188.94	-89.7	183.94	-89.9	184.6
4E4	180.35	-89.8	188.56	-89.7	183.52	-89.9	184.1
8E4	179.88	-89.8	188.16	-89.7	183.13	-90.0	183.7
2E5	179.34	-89.7	187.51	-89.5	182.64	-90.0	183.2
4E5	178.7	-89.6	186.6	-89.2	182.0	-89.8	182.4
8E5	177.3	-89.4	184.6	-88.8	180.4	-90.0	180.8

Table 4.4: Water dielectric

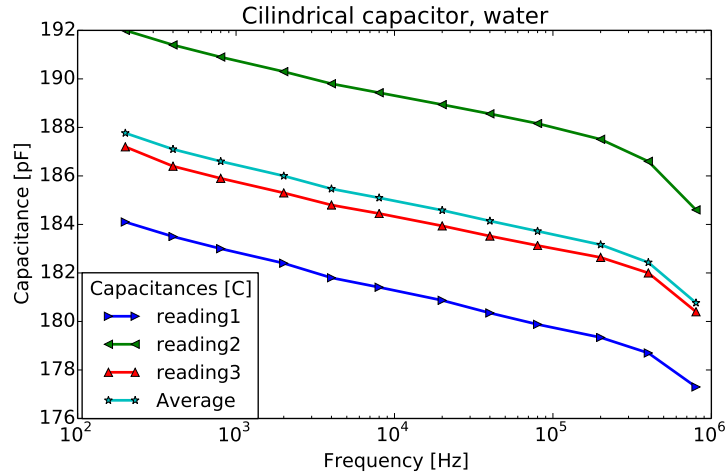


Figure 4.5: Water dielectric

Freq[Hz]	$C^1[pF]$	$\phi^1[^\circ]$	$C^2[pF]$	$\phi^2[^\circ]$	$C^3[pF]$	$\phi^3[^\circ]$	$C^{av}[pF]$
2E2	79.0	-89.8	79.1	-89.8	78.4	-89.8	78.8
4E2	78.8	-89.9	79.0	-89.9	78.3	-89.9	78.7
8E2	78.7	-89.8	78.9	-89.8	78.2	-89.8	78.6
2E3	78.7	-89.9	78.8	-89.9	78.1	-89.9	78.5
4E3	78.6	-89.9	78.8	-89.9	78.1	-89.9	78.5
8E3	78.54	-89.9	78.72	-89.9	78.0	-89.9	78.4
2E4	78.48	-90.0	78.65	-89.9	77.91	-89.9	78.3
4E4	78.45	-90.0	78.59	-90.0	77.85	-89.9	78.3
8E4	78.43	-90.0	78.53	-90.0	77.78	-90.0	78.2
2E5	78.38	-90.1	78.44	-89.9	77.68	-90.0	78.2
4E5	78.24	-89.9	78.27	-90.0	77.53	-89.8	78.0
8E5	77.8	-89.9	77.8	-90.0	77.0	-90.0	77.5

Table 4.5: Oil dielectric

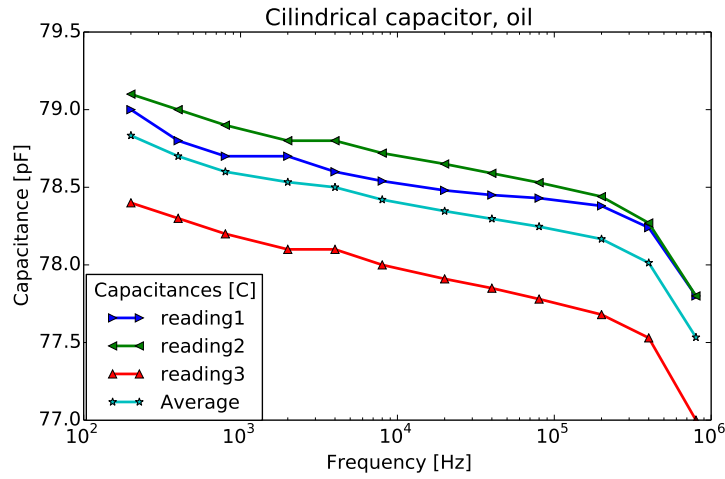


Figure 4.6: Oil dielectric

C1 and C3 represent the capacitance component of the outer and inner glass walls, whereas C2 represents the capacitance of the material under study.

$$C1 = \frac{2\pi 8.8542 \times 10^{-12} \varepsilon_G 0.080}{\log \frac{0.1255/2}{0.1193/2}} \quad (4.1)$$

$$C2 = \frac{2\pi 8.8542 \times 10^{-12} \varepsilon_X 0.080}{\log \frac{0.1193/2}{0.110}} \quad (4.2)$$

$$C3 = \frac{2\pi 8.8542 \times 10^{-12} \varepsilon_G 0.080}{\log \frac{0.110/2}{0.104/2}} \quad (4.3)$$

$$C = \frac{1}{\frac{1}{C1} + \frac{1}{C2} + \frac{1}{C3}} \quad (4.4)$$

Initially, the glass permittivity was calculated from Eq 4.1 using the average capacitance from Table 4.2. Once the glass permittivity is known, it is possible to calculate the capacitance of the inside glass wall using by Eq 4.3. These data are listed in Table 4.6.

The partial capacitance component C2 attributed to air, water and oil dielectricum alone was calculated using Eq 4.4 and the average capacitances in Tables 4.3-4.5 together with the above C1 and C3. Finally, the dielectricum permittivities ε were derived using Eq 4.2. Table 4.7 lists the calculated parameters.

The column for the permittivity of water is missing in Table 4.7 since the capacitance turned to be negative. However the other two dielectrics, air and oil, have their permittivity relatively close to the anticipated values ($\varepsilon_A \approx 1.0$ and $\varepsilon_O \approx 2.5$). The developed hypothesis is that this difference originates from the fact that the water dielectricum has an associated conductivity that is much larger in comparison to the air and oil that are de facto insulators. The conductive water dielectricum requires a different approach which is outlined in the following two sections.

Freq[Hz]	$C1^{av}[pF]$	$\varepsilon_R[1]$	$C3[pF]$
2E2	368.1	4.19	332.47
4E2	367.1	4.18	331.68
8E2	366.2	4.17	330.88
2E3	365.1	4.16	330.09
4E3	364.4	4.15	329.30
8E3	363.7	4.14	328.50
2E4	362.8	4.13	327.71
4E4	362.1	4.12	326.92
8E4	361.6	4.12	326.92
2E5	360.8	4.11	326.12
4E5	359.8	4.10	325.33
8E5	357.7	4.07	322.95

Table 4.6: Glass wall permittivity

Freq[Hz]	$C_A^{av}[pF]$	$C_W^{av}[pF]$	$C_O^{av}[pF]$	$C2_A^{av}[pF]$	$C2_W^{av}[pF]$	$C2_O^{av}[pF]$	$\varepsilon_A[1]$	$\varepsilon_O[1]$
2E2	49.9	187.8	78.8	69.85	-2502.32	143.56	1.27	2.62
4E2	49.8	187.1	78.7	69.73	-2536.32	143.52	1.27	2.62
8E2	49.8	186.6	78.6	69.80	-2538.49	143.48	1.27	2.62
2E3	49.8	186.0	78.5	69.87	-2550.32	143.46	1.27	2.62
4E3	49.7	185.5	78.5	69.74	-2563.14	143.72	1.27	2.62
8E3	49.7	185.1	78.4	69.80	-2556.41	143.65	1.27	2.62
2E4	49.7	184.6	78.3	69.87	-2559.51	143.60	1.27	2.62
4E4	49.6	184.1	78.3	69.73	-2572.75	143.87	1.27	2.62
8E4	49.6	183.7	78.2	69.75	-2626.87	143.61	1.27	2.62
2E5	49.5	183.2	78.2	69.62	-2635.33	143.89	1.27	2.62
4E5	49.5	182.4	78.0	69.69	-2697.83	143.53	1.27	2.62
8E5	49.1	180.8	77.5	69.09	-2769.16	142.63	1.26	2.60

Table 4.7: Air, Water, Oil capacitances and permittivities

4.4 FEM approach to the ‘negative’ permittivity problem

In order to gain a deeper understanding of the water permittivity measurement, a finite element model of this process in the electrostatic domain was conducted. The model created is axisymmetric and therefore represents the actual conditions without any scaling factor that is common in 2-D planar FEM models. The resulting capacitance was calculated from the total energy of the electrostatic field established by one coulomb charged electrode. The formula in Eq 4.6 was used and since one coulomb charge is applied, the resulting capacitance simplifies to the reciprocal of twice the energy value.

$$A = \frac{Q^2}{2C} \quad [J] \quad (4.5)$$

$$C = \frac{Q^2}{2A} \quad (4.6)$$

$$C = \frac{1}{2A} \quad (4.7)$$

Figure 4.7 and Table 4.8 lists the energies stored in the field as obtained by Maxwell FEM software for the electrode configurations corresponding to the experiment above (Figure 4.2) and the resulting capacitances. The FEM meshing density was refined in a number of iterations and provided the output data when the energy error fell below 1%. This simulation confirmed the previous experimental problem where the capacitance of the water dielectric becomes negative resulting in negative permittivity. Observing the energy data alone shows the total energy is smaller than the combined energies of the glass dielectricum only.

The initial configuration in which the glass dielectric capacitors (C1 and C3) had

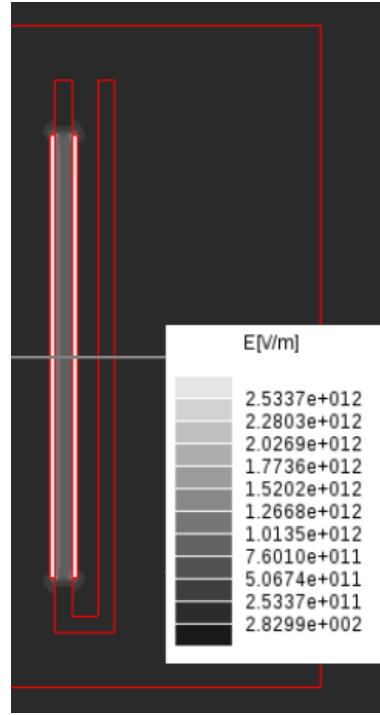


Figure 4.7: FEM electrostatic field simulation.

capacitive element	field energy A[J] FEM simulation	capacitance [pF] Eq 4.7
C1 (glass out)	1.36122e+9	367.32
C3 (glass in)	1.50516e+9	332.19
C (w/ water)	2.8608e+9	174.78
C2 (water)		Eq 4.4: -88740.18

Table 4.8: Original configuration model from Figure 4.2

the electrode on the water side spanning over the entire water domain volume was modified. This case is illustrated in Figure 4.8 as if the electrode system was filled by a highly conductive mercury instead of water. Table 4.9 lists the energies and resulting capacitances C1 and C2, with the water permittivity. This study revealed

that by considering the conductance of the measured dielectricum the capacitance drifts to higher values and as a result generates the water permittivity of 73.9 that is close to the real value. The next section will confirm this hypothesis through another experimental verification.

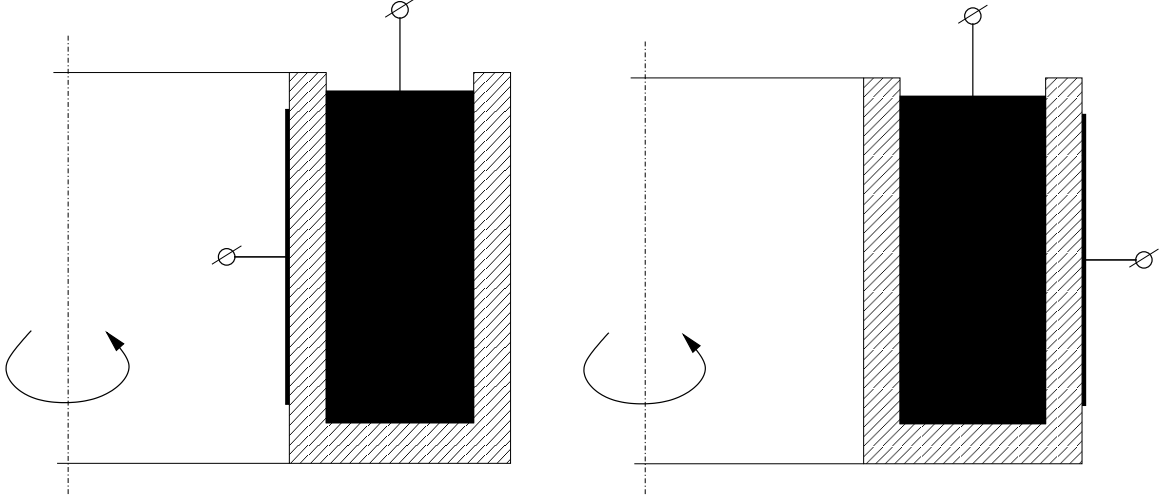


Figure 4.8: Conductive dielectric electrode for glass-wall capacitors analysis.

capacitive element	field energy A[J] FEM simulation	capacitance [pF] Eq 4.7
C1 (glass out)	1.27029e+9	393.61
C3 (glass in)	1.46714e+9	340.80
C (w/ water)	2.8608e+9	174.78
C2 (water)		Eq 4.4: 4052.8

```
octave/matlab:
C2=1/(2*(2.8608-1.46714-1.27029))
C2=4.0528 [nF]
EPSw=4052.8*log(0.1193/0.110)/(2*3.1415926*8.8542*0.08)
EPSw=73.907 [1]
```

Table 4.9: Modified configuration model from Figure 4.8

4.5 Experimental resolution of the ‘negative’ permittivity

Based on the results from the fem simulation, another experiment that replicated the same process was performed. A spiraled bare copper wire 14 AWG was inserted between the glass walls and immersed into the water dielectric. The copper wire formed one electrode while the shim electrode on the outside glass wall or the inside glass wall created the capacitor C1 and C2 respectively. Three runs of data are listed in Tables 4.10 - 4.11. It can be observed that there has been a small shift to higher capacitance values which corresponds to a reduced energy of the field.

Water dielectric capacitance C listed in Table 4.12 was measured again with the copper wire removed. This capacitance also differs by some 5% from the Table 4.4 but the experiment was reconfigured and remained unchanged over the course of three runs of data collection which was not the case of the former experiment. The calculated capacitance C2 and corresponding permittivity ϵ_W became more realistic this time but near the value of 96 at the low frequencies which is a 20% higher than the expected values (Appendix B). This corresponds to the 20% discrepancy largely seen in the air and oil permittivity measurement above and thus it was concluded that the dimensions of the glass apparatus used in Eq 4.2 are not very accurate. Besides the glass dimension tolerances, however, the shape deviation in terms of the concentricity may actually have more effect on the obtained results. Based on these findings, the permittivity data was compensated by a factor of 1.2 which is plotted in Figure 4.12. It can also be observed the data drifting out of control in the last decade of high frequencies. This behavior can be understood as a result of the measured impedance angle largely deviating from the negative 90 degrees angle of an ideal capacitor largely seen at the high frequencies. In order to justify this assumption, an additional ex-

Freq[Hz]	$C^1[pF]$	$\phi^1[^\circ]$	$C^2[pF]$	$\phi^2[^\circ]$	$C^3[pF]$	$\phi^3[^\circ]$	$C^{av}[pF]$
2.00E+002	338.2	-89.6	338.7	-89.6	338.8	-89.6	338.57
4.00E+002	337.3	-89.7	337.7	-89.7	337.8	-89.6	337.60
8.00E+002	336.4	-89.6	336.9	-89.6	336.9	-89.6	336.73
2.00E+003	335.5	-89.7	335.9	-89.7	335.9	-89.6	335.77
4.00E+003	334.8	-89.7	335.2	-89.7	335.2	-89.6	335.07
8.00E+003	334.08	-89.6	334.49	-89.6	334.51	-89.5	334.36
2.00E+004	333.21	-89.3	333.64	-89.5	333.56	-89.2	333.47
4.00E+004	332.33	-88.9	332.9	-89.2	332.56	-88.7	332.60
8.00E+004	330.91	-88.1	332	-88.6	330.75	-87.6	331.22
2.00E+005	324.7	-86	328.7	-87.1	322.9	-85.1	325.43
4.00E+005	312.9	-83.9	321.2	-85	308.5	-82.7	314.20
8.00E+005	293.8	-82.1	304.2	-82.7	285.9	-80.8	294.63

Table 4.10: Glass wall capacitance C3 - inside

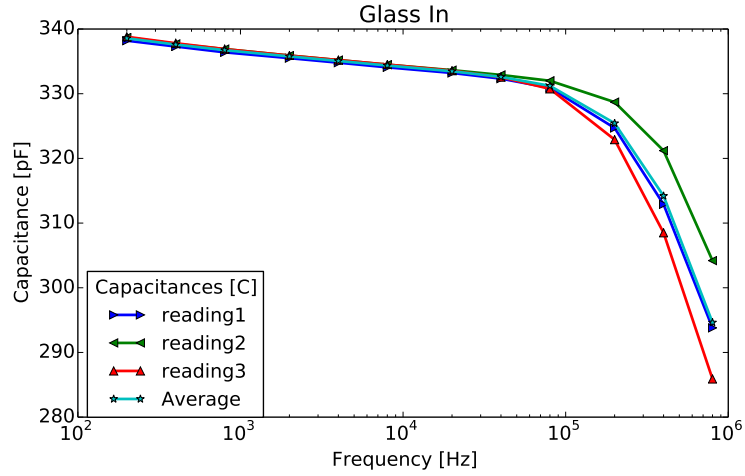


Figure 4.9: Glass wall capacitance C3 - inside

Freq[Hz]	$C^1[pF]$	$\phi^1[^\circ]$	$C^2[pF]$	$\phi^2[^\circ]$	$C^3[pF]$	$\phi^3[^\circ]$	$C^{av}[pF]$
2.00E+002	407.5	-89.6	407.4	-89.6	407.3	-89.6	407.40
4.00E+002	406.3	-89.6	406.1	-89.6	406.1	-89.6	406.17
8.00E+002	405.2	-89.6	405.1	-89.6	405	-89.6	405.10
2.00E+003	404	-89.7	403.8	-89.7	403.8	-89.6	403.87
4.00E+003	403.1	-89.6	402.9	-89.7	402.8	-89.6	402.93
8.00E+003	402.29	-89.6	402.11	-89.6	401.96	-89.4	402.12
2.00E+004	401.17	-88.3	401.02	-89.4	400.76	-89	400.98
4.00E+004	400.12	-88.8	400.08	-89.1	399.49	-88.3	399.90
8.00E+004	398.16	-87.8	398.93	-88.4	396.64	-87	397.91
2.00E+005	389.8	-85.4	394.4	-86.5	384	-83.8	389.40
4.00E+005	373.6	-83.1	383.8	-84.1	361.9	-81.2	373.10
8.00E+005	347.7	-81.1	360.8	-81.5	331	-79.6	346.50

Table 4.11: Glass wall capacitance C1 - outside

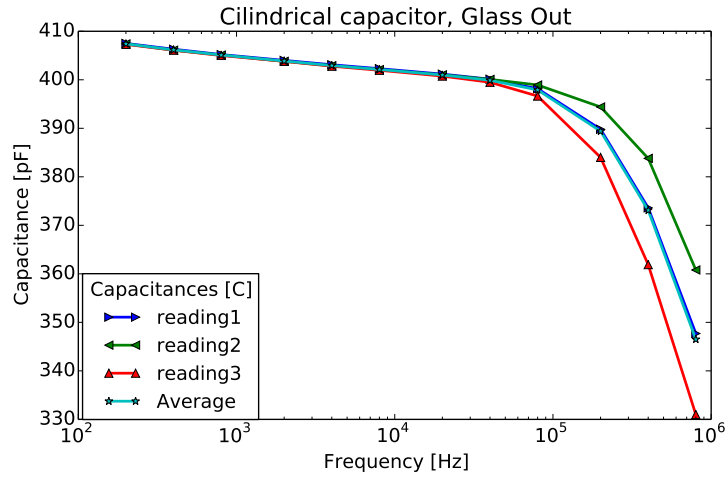


Figure 4.10: Glass wall capacitance C1 - outside

Freq[Hz]	$C^1[pF]$	$\phi^1[^\circ]$	$C^2[pF]$	$\phi^2[^\circ]$	$C^3[pF]$	$\phi^3[^\circ]$	$C^{av}[pF]$	$C2[pF]$	ε_W
2.00E+002	179.3	-89.6	178.7	-89.6	178	-89.6	178.67	5296.70	96.59
4.00E+002	178.8	-89.7	178.2	-89.7	177.4	-89.7	178.13	5273.05	96.16
8.00E+002	178.3	-89.6	177.7	-89.6	177	-89.7	177.67	5255.34	95.84
2.00E+003	177.8	-89.7	177.2	-89.7	176.5	-89.7	177.17	5260.96	95.94
4.00E+003	177.4	-89.7	176.8	-89.7	176.1	-89.7	176.77	5238.50	95.53
8.00E+003	177.03	-89.7	176.45	-89.7	175.77	-89.8	176.42	5241.35	95.58
2.00E+004	176.59	-89.8	176.04	-89.8	175.34	-89.8	175.99	5277.01	96.23
4.00E+004	176.24	-89.8	175.7	-89.8	174.99	-89.8	175.64	5374.46	98.01
8.00E+004	175.89	-89.8	175.36	-89.8	174.64	-89.8	175.30	5802.40	105.81
2.00E+005	175.39	-89.6	174.87	-89.6	174.17	-89.7	174.81	12560.11	229.05
4.00E+005	174.8	-89.5	174.3	-89.5	173.6	-89.6	174.23	-8096.98	-147.66
8.00E+005	173.2	-89.2	172.7	-89.3	172.2	-89.3	172.70	-2042.22	-37.24

Table 4.12: Water dielectric capacitance C2 and permittivity

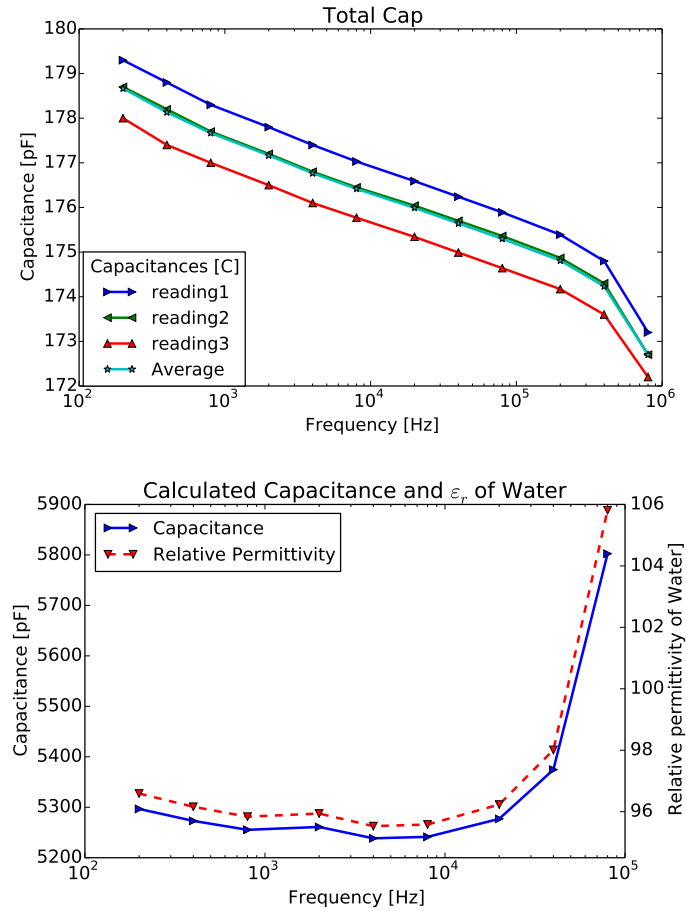


Figure 4.11: Water dielectric capacitance C2 and permittivity

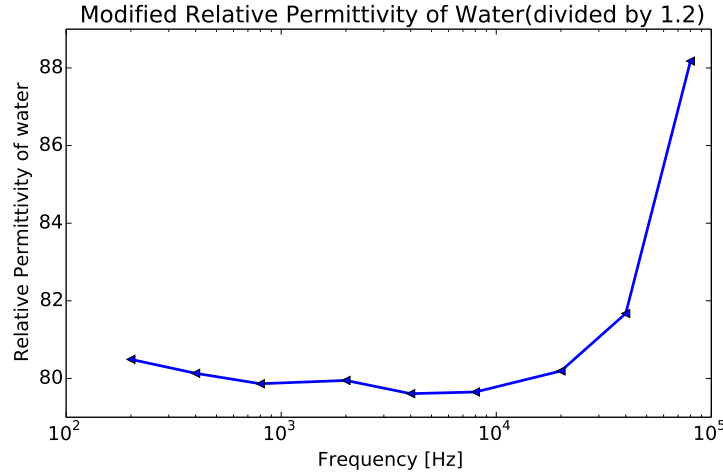


Figure 4.12: Adjusted the measured permittivity of water by 1.2 factor

Freq[Hz]	$C3[pF]$	$\phi[^\circ]$	$C1[pF]$	$\phi[^\circ]$	$C[pF]$	$\phi[^\circ]$
2.00E+002	339	-89.6	384.8	-89.6	173.9	-89.6
4.00E+002	338	-89.7	383.6	-89.7	173.4	-89.7
8.00E+002	337.2	-89.6	382.7	-89.6	173	-89.7
2.00E+003	336.2	-89.7	381.6	-89.7	172.5	-89.7
4.00E+003	335.5	-89.7	380.8	-89.7	172.1	-89.7
8.00E+003	334.83	-89.8	380.05	-89.8	171.77	-89.8
2.00E+004	334.01	-89.8	379.13	-89.8	171.37	-89.8
4.00E+004	333.41	-89.8	378.42	-89.8	171.05	-89.8
8.00E+004	332.93	-89.8	377.85	-89.8	170.75	-89.9
2.00E+005	332.2	-89.8	377	-89.8	170.38	-89.8
4.00E+005	331.4	-89.8	376.2	-89.8	169.9	-89.9
8.00E+005	329.8	-89.8	374.5	-89.8	169	-89.9

Table 4.13: Capacitance data for determining saline water permittivity

periment was conducted with saline water that has much higher conductivity. The resistance component of the measured impedance significantly decreased which is demonstrated in Table 4.13 by more consistent impedance angle near negative 90 degrees. As a result the calculated permittivity shown in Figure 4.13/Table 4.14 is more consistent in this experiment justifying earlier assumptions. This study also suggests

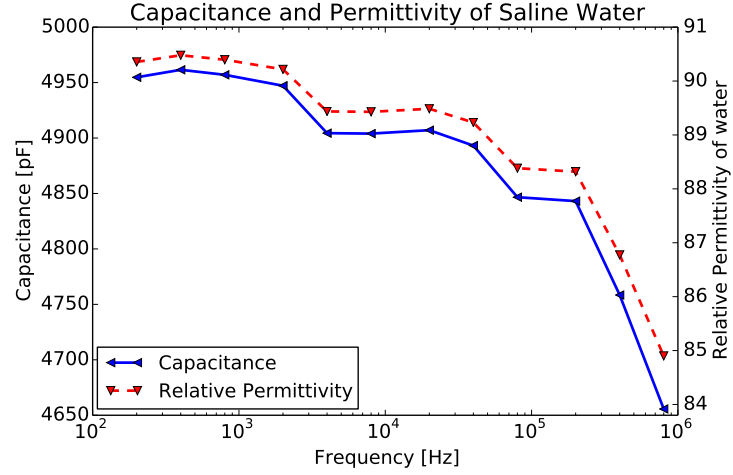


Figure 4.13: Saline water capacitance

	Freq[Hz]	C2[pF]	ε_{SW}
[h]	2.00E+002	4954.76	90.35
	4.00E+002	4961.53	90.48
	8.00E+002	4957.00	90.40
	2.00E+003	4947.15	90.22
	4.00E+003	4904.39	89.44
	8.00E+003	4903.99	89.43
	2.00E+004	4907.08	89.49
	4.00E+004	4893.15	89.23
	8.00E+004	4846.65	88.38
	2.00E+005	4843.11	88.32
	4.00E+005	4758.44	86.77
	8.00E+005	4655.66	84.90

Table 4.14: Saline water capacitance

that if sufficient conductivity is present in the water phase, the composition sensor may benefit from not-insulating the outer electrode that faces the centrifuged water phase and make the water phase acting as an electrode. This will result in a nearly one dielectricum capacitor that may have larger sensitivity than a multi-dielectricum

one.

The data collected and calculated are in the range near the expected values which was the objective of this study, to confirm the large difference between the oil dielectric and water dielectric permittivities. A new apparatus will be constructed in future to conduct more accurate measurements of the same phenomena. The new apparatus will have more dimensional accuracy but mostly the insulation layer will have the thickness at least an order of magnitude smaller than the measured fluidum dielectric between the electrodes. The electrodes will be suspended from above and immersed into the fluidum. While immersed, the electrodes will be lowered and risen to induce a flow between the electrodes that will help to 'clean' them from any air bubbles that may have developed on the walls.

4.6 Incomplete Separation Study

The last part of this study investigates the effect of an incomplete separation of the multiphase composition in which a multiphase domain is partly present between the individual phases, oil and water. Hydrocyclone's function is to centrifuge the mixture into separate phases, however, this process is very complex and has many parameters that govern the separation process. Time and the centrifugal velocity (tangential speed of flow in the cyclone) are the most significant parameters of all. Given a prolonged time, similar to the gravity based separators, the process eventually converges into well separated layers that were considered in the previous Section. However, the process of hydrocarbons extraction needs to sustain certain production flows and shall not be constrained by the hydrocyclone operation. Turbo-cyclone concept may significantly increase the centrifugal effect and thus reduce the need for large volume hydro-cyclones. This concept is outlined in the Future Work section.

In this study, it was first considered the effect of a well mixed composition. A 50% oil/water mixture was prepared using Corning Magnetic Stirrer model PC-620 and poured into the glass apparatus to measure the capacitance development over the time. The Table 4.15 lists this capacitance as measured at 800kHz. Two separate experiments were conducted, the impedance angle was monitored only in the first run and confirmed a nearly perfect capacitor with glass insulated electrodes. The first run settled just after 30 seconds from the initial pour and the second run after 60 seconds. After a minute and half the process is settled to 0.01% with an average measured capacitance of 129.6 pF. This closely corresponds to two capacitors in parallel, bottom half with water dielectric and top half with oil ($180.8\text{pF}/2 + 77.5\text{pF}/2 = 129.15\text{pF}$). The equivalent permittivity of the mixture before it started to separate is calculated as 28.38 which sits between the permittivity of water ($78 \sim 81$) and the permittivity of oil ($1.5 \sim 2.5$).

4.6.1 Oil-in-water and water-in-oil differences

A parallel study based on FEM simulation was conducted for two 50% water/oil mixtures. In one model, oil bubbles were dispersed in a continuous water phase while

Time[s]	$C^1[\text{pF}]$	$\phi[^\circ]$	$C^2[\text{pF}]$	$C^{av}[\text{pF}]$	$C^2[\text{pF}]$	$\varepsilon_M[1]$
0	140	-89.3	166	153.0	1556.44	28.38
15	134	-89.4	160	147.0	1099.79	20.05
30	132.5	-89.5	155	143.8	942.82	17.19
45	132.3	-89.5	134	133.2	619.56	11.29
60	132.2	-89.4	128.3	130.2	559.59	10.20
75	132.1	-89.4	127.5	129.8	552.27	10.07
90	132.0	-89.4	127.2	129.6	548.67	10.00
105	132.0	-89.4	127.2	129.6	548.67	10.00
120	132.0	-89.4	127.2	129.6	548.67	10.00

Table 4.15: 50% mixture separation in time

the composition was reversed in the other model, i.e. water bubbles were dispersed in a continuous oil phase. Both cases are illustrated in Figure 4.14. The dimensions of the parallel plate capacitor are 0.08m(W) x 0.01m(H) x 1.0m (L - default dimension in the Maxwell 2-D FEM simulation).

Table 4.16 shows the capacitance of both models calculated by Eq 4.7 and the relative permittivity equivalent to one dielectricum capacitor calculated using the parallel plate capacitor formula with the dimensions of the FEM model stated above:

$$\varepsilon_r = \frac{0.01 \times C[pF]}{8.8542 \times 0.08} \quad (4.8)$$

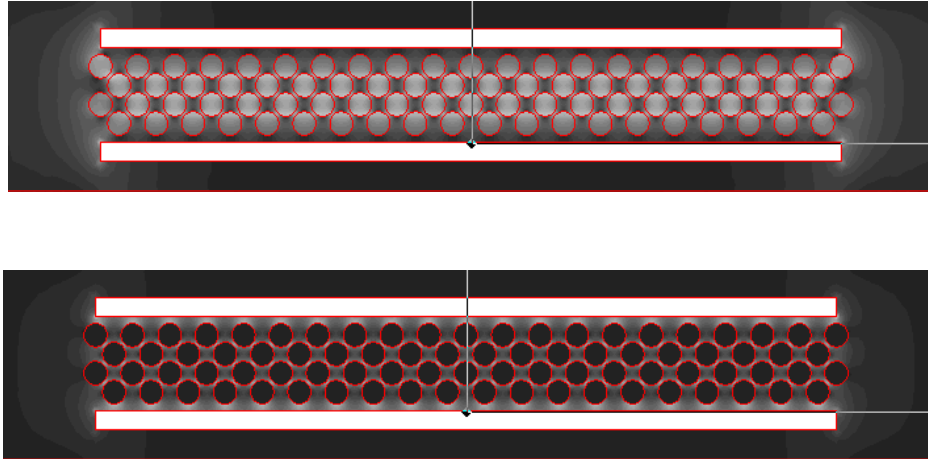


Figure 4.14: 50% water/oil mixture: (TOP) oil bubbles dispersed in continuous water phase, (BOTTOM) water bubbles dispersed in continuous oil phase

configuration	field energy A[J] FEM simulation	capacitance C[pF] Eq 4.7	equivalent permittivity $\varepsilon_r[1]$ Eq 4.8
Oil-in-Water	1.564e+8	3197	45.134
Water-in-Oil	1.1919e+9	419.5	5.922

Table 4.16

One can observe how quantitatively different electrostatic field cases result from the same mixture composition of 50% oil and water but with different dispersion layouts. In both cases the continuous phase is dominating the field, i.e. the equivalent permittivity of the oil-in-water mixture corresponds to nearly two fold less the water permittivity while the equivalent permittivity of the water-in-oil mixture corresponds to three fold more the oil permittivity. This could explain the large data deviations in the experimental work described in the next section. In the experimental work, large oil concentrations above 50% generate a very consistent, extremely low uncertainty calibration curves as expected from a sensor. However, mixtures of higher water content behave very erratically providing calibration curves of large uncertainty. This study proves again the need for an efficient hydrocyclone to eliminate the uncertainty of the mixture composition and the associated measurement.

4.6.2 Permittivity transitional buffer effects

In the end of this study, a limited analytical analysis was conducted to gain a partial view of the inaccuracies in composition reading when a transitional buffer is developed between the water phase and the oil phase. Here it was considered that the permittivity gradually changes from oil permittivity to water permittivity over a buffer of certain width. The transition is considered to be linear as depicted in the picture below (Figure 4.15).

The total capacitance is derived from the formula for cylindrical capacitor in infinitesimal format which constitutes a parallel plate capacitor, Eq 4.9. The only difference from a cylindrical capacitor of a constant permittivity is that here the permittivity is changing linearly with the radial distance φ .

It was assumed the buffer to range from φ_1 to Φ_1 in the radial direction. The resulting capacitance in Eq 4.13 is similar to the plain cylindrical capacitor formula such as the

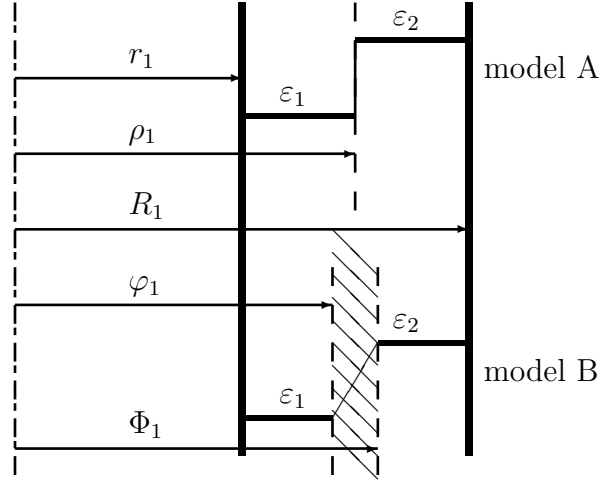


Figure 4.15: Transitional buffer between the water and oil phase

one listed in Eqs 4.1 - 4.3 with a factor $\frac{\varepsilon_1 \Phi_1 - \varepsilon_2 \varphi_1}{\Phi_1 - \varphi_1}$ in place of the relative permittivity in the numerator as well as one additional coefficient $\frac{\varepsilon_1}{\varepsilon_2}$ in the denominator's argument. Figure 4.16 plots the capacitance as it changes with the transitional buffer width. The horizontal lines in the plot represent different oil/water compositions when a stepwise permittivity profile is considered (Model A). Naturally, the 50% stepwise permittivity change in Model A meets the Model B characteristic at the buffer of zero width. However, as the buffer width increases up to 10% of the total cavity width, the sensor as outlined in the previous Chapter would provide an erroneous reading by 0.8% of the composition (watercut) for every percent of the buffer width. This would negatively affect the targeted accuracy of the proposed sensor, however, based on the experiments outlined later in this work, the uncertainties of sensor reading were in the range of 1% or below in case of higher oil concentrations. This gives an indication that the buffer width in the tap water/mineral oil multiphase system was

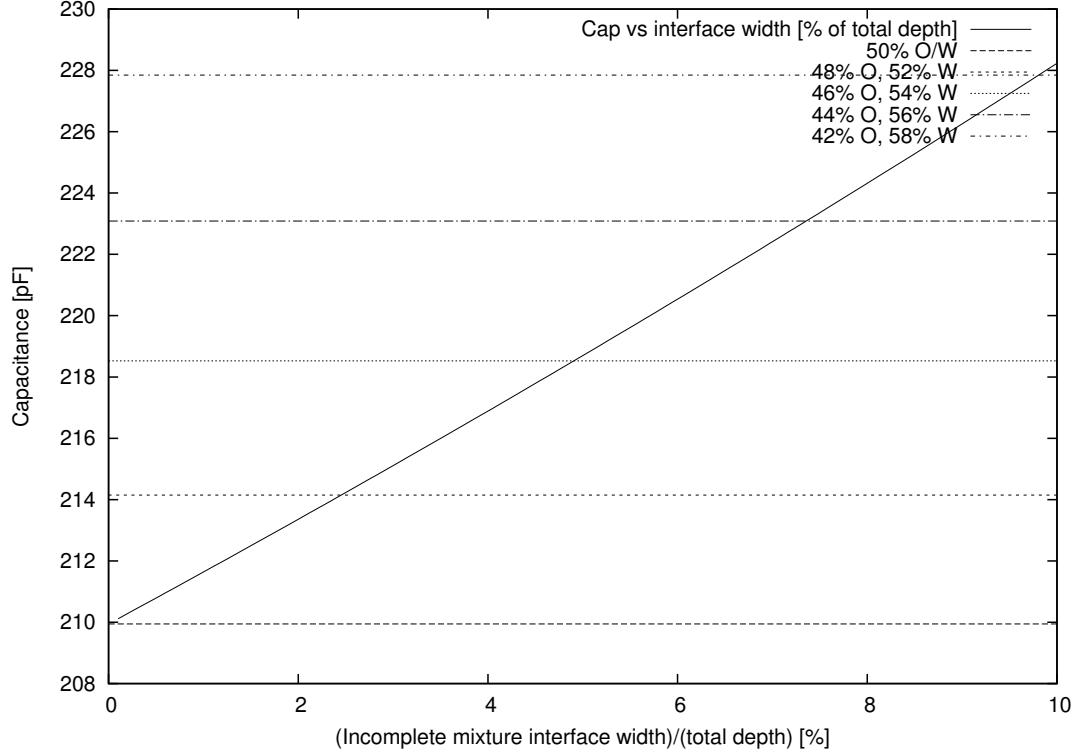


Figure 4.16: C2 capacitance drifting with the transitional buffer width.

well stratified in the hydro-cyclone with a buffer width below 1%.

This is only a theoretical study that will require a thorough experimental verification that is beyond the scope of this work. The experimental work explained in the next section lacked a system to monitor and control the interface buffer width. As part of this research, it was implemented a visualization technique to monitor the level of separation (stratification) within the cyclone's chamber, but the level of detail was insufficient to gain meaningful data. The future work involves the design and implementation of a turbo-cyclone that will allow to vary the tangential speed independently from the net flow through the sensor.

$$dC = \frac{\varepsilon_0 \varepsilon_r(\varphi) 2\pi \varphi H}{d\varphi} \quad (4.9)$$

$$C^{-1} = \int_{\varphi=\varphi_1}^{\varphi=\Phi_1} \frac{1}{dC} = \int_{\varphi_1}^{\Phi_1} \frac{d\varphi}{\varepsilon_0 \varepsilon_r(\varphi) 2\pi \varphi H} = \int_{\varphi_1}^{\Phi_1} \frac{d\varphi}{D(\varphi)} \quad (4.10)$$

$$\begin{aligned} \varepsilon_r(\varphi) &= a + b\varphi \\ a &= \frac{\varepsilon_1 \Phi_1 - \varepsilon_2 \varphi_1}{\Phi_1 - \varphi_1} \\ b &= \frac{\varepsilon_2 - \varepsilon_1}{\Phi_1 - \varphi_1} \end{aligned} \quad (4.11)$$

$$\begin{aligned} C^{-1} &= \int_{\varphi_1}^{\Phi_1} \frac{d\varphi}{\varepsilon_0(a + b\varphi) 2\pi \varphi H} = \\ &= \frac{1}{2\varepsilon_0 \pi H} \int_{\varphi_1}^{\Phi_1} \frac{d\varphi}{(a + b\varphi)\varphi} = \\ &= \frac{1}{2\varepsilon_0 \pi H} \int_{\varphi_1}^{\Phi_1} \left[\frac{-b/a}{(a + b\varphi)} + \frac{1/a}{\varphi} \right] d\varphi = \\ &= K_1 \int_{\varphi_1}^{\Phi_1} \frac{d\varphi}{(a + b\varphi)} + K_2 \int_{\varphi_1}^{\Phi_1} \frac{d\varphi}{\varphi} = \\ &= \frac{K_1}{b} \left\{ \ln |a + b\varphi| \right\}_{\varphi_1}^{\Phi_1} + K_2 \left\{ \ln |\varphi| \right\}_{\varphi_1}^{\Phi_1} = \\ &= \frac{K_1}{b} \ln \frac{|a + b\Phi_1|}{|a + b\varphi_1|} + K_2 \ln \frac{|\Phi_1|}{|\varphi_1|} = \\ &= \ln \left[\left(\frac{|a + b\Phi_1|}{|a + b\varphi_1|} \right)^{\frac{K_1}{b}} \left(\frac{|\Phi_1|}{|\varphi_1|} \right)^{K_2} \right] \\ K_1 &= -\frac{b}{2a\varepsilon_0 \pi H} \\ K_2 &= \frac{1}{2a\varepsilon_0 \pi H} \end{aligned} \quad (4.12)$$

$$\begin{aligned}
C &= \frac{1}{K_2 \ln \left[\frac{\left(\frac{\Phi_1}{\varphi_1} \right)}{\left(\frac{|a+b\Phi_1|}{|a+b\varphi_1|} \right)} \right]} = \\
&= \frac{1}{\frac{1}{2\varepsilon_0\pi H \frac{\varepsilon_1\Phi_1 - \varepsilon_2\varphi_1}{\Phi_1 - \varphi_1}} \ln \left[\frac{\left(\frac{\Phi_1}{\varphi_1} \right)}{\left(\frac{\varepsilon_r(\Phi_1)}{\varepsilon_r(\varphi_1)} \right)} \right]} = \\
&= \frac{2\varepsilon_0\pi H \frac{\varepsilon_1\Phi_1 - \varepsilon_2\varphi_1}{\Phi_1 - \varphi_1}}{\ln \left(\frac{\Phi_1}{\varphi_1} \right) - \ln \left(\frac{\varepsilon_2}{\varepsilon_1} \right)} \tag{4.13}
\end{aligned}$$

4.7 Conclusion

The work described in this section aimed at providing a deeper knowledge of the processes and the associated parameters utilized in the measurement of multiphase composition through a capacitance. A fundamental measurement of the water permittivity opened a new floor for further studies as a simple cylindrical model with sharp boundaries turned to be insufficient - resulting in negative capacitance/permittivity. A set of FEM analysis and additional experiments were conducted to verify that the conductive phase has to be considered across its full domain with stray fields at the electrode boundaries. The recommendation for the future experiments is to significantly decrease the insulation layer thickness from the current 3.0 millimeters, and immerse the system of concentric electrodes into the analyzed liquid - rather than pouring the liquid into a glass vessel.

The same mixture composition but different dispersion layouts were analyzed using FEM. It shows how quantitatively different results can be obtained for oil-in-water or water-in-oil situation with the continuous phase dominating the equivalent permittivity.

Lastly, a concept of incomplete separation resulting in a transitional buffer where

permittivity changes gradually rather than piecewise was analyzed by FEM and analytically. A transfer function corresponding to the error uncertainty propagation was derived for the case of 50% oil/water composition; 0.8% of composition drift for 1% increase of the buffer width. This work is only scratching a surface of the more complex phenomena where emulsions can dominate the flow. A more sophisticated experimental apparatus is required to complete this study.

The future plan includes an electrodynamic FEM analysis of sensor, considering the effect of the frequency in the electrical permittivity of the liquids. In addition, the configuration in which the outer electrode is in direct contact with the liquid will be analyzed and tested. This configuration can potentially improve the accuracy of the sensor and simplify its construction.

Chapter 5

Design of a Compact Multiphase Flow Loop

5.1 Introduction

Sensor calibration plays an important role in development of a new sensor as well as in most commercial sensor validations. In fact some sensors require a periodical re-calibration in the field due to the previously mentioned reasons of aging and drifts in parameters.

A sensor calibration requires that the sensor be tested in a wide variety of compositions which calls for an automated system due to the long period of data collection. In order to generate the wide composition changes in a controlled environment, many manufacturers have built flow recirculating loops that provide a flow of precise composition, and circulates it through the sensor under test. Once the flow passes through the sensor, it enters the separator where it slowly separates into the original components. After the separation process is complete, the liquids can be used again, possibly in a different oil/water composition as needed. In addition to the testing facilities owned

by the main manufacturers, there are a few independent facilities around the world, for example at the Southwest Research Institute (CEESI in USA), TÜV-NEL (Scotland). IFP (France), SINTEF (Norway), DNV Kema (Netherlands) and others. The differences between these facilities are mainly the operation range, the composition of the flow (biphase or multiphase) and the composition of each phase. Even when they have many differences, all of them have the same main parts. All of them have a separator, some type of speed controlled pump connected with single phase flowmeters, a mixer section and connections for the sensor under test. Some sections of this flow loops have transparent pipes that allows for flow visualization [2].

As part of this research, a small flow loop was developed, this compact flow loop is shown in Figure 5.1. This flow loop has most of the basic components of a typical flow loop used in industry. The flow loop comprises a separator tank, two gear pumps, and a mixer stage where the flows mix before entering into the sensor. After the flow circulates through the sensor, it enters the gravity-based separator where it slowly separates into the original components, oil and water. After the separation process is complete, the liquids can be used again, possibly in a different oil/water composition as needed. The operation of this flow loop, as well as the data acquisition is performed by a computer and additional signal conditioning systems. The following sections describe in detail every part of this flow loop in detail.

5.2 Multiphase Separator

A multiphase separator is a type of production facility found within the Oil and Gas industry and is available in many different forms: vertical, horizontal, or spherical (Figure 5.2). They are used to separate the stream from the production field into oil, water, and gas. Horizontal separators are generally smaller and less expensive than

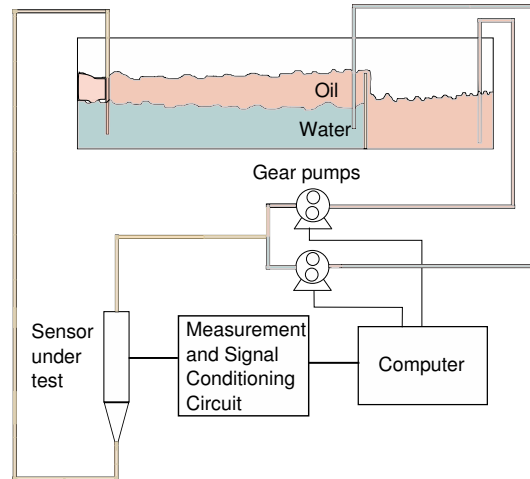


Figure 5.1: Multiphase flow loop

vertical separators. In addition, they are more suited to the separation of three-phase flow. Vertical separators require less room to operate and are commonly used on offshore topside facilities. The separation is accomplished principally by gravity, in which the heavier phase drifts to the bottom and the lighter phase drifts to the top. Spherical separators use the same principle as the vertical or horizontal separators, but they are seldom used due to their lower efficiency and size.

In this project, a horizontal separator was used. The separator body is made of a plexiglas tank, connecting transparent tubes and an aluminum lid (see Figure 5.1). Clear plexiglas was chosen as a sight glass to monitor the effectiveness of the separation. Since the initial focus of this research is on two-phase flows, the tank is not pressurized and can also be open to the atmosphere.

A 100cm (L) x 20cm (W) x 20cm (H) tank was designed to hold a maximum volume of 40 litres. A 99% pure liquid paraffin oil dyed to a red colour, (for distinction from the water phase) was used, along with tap water. This type of separation is dependent on gravity as the heavier water will settle at the bottom of the tank since the specific gravity of oil and water is typically 0.88 and 1.00 respectively. This separated water

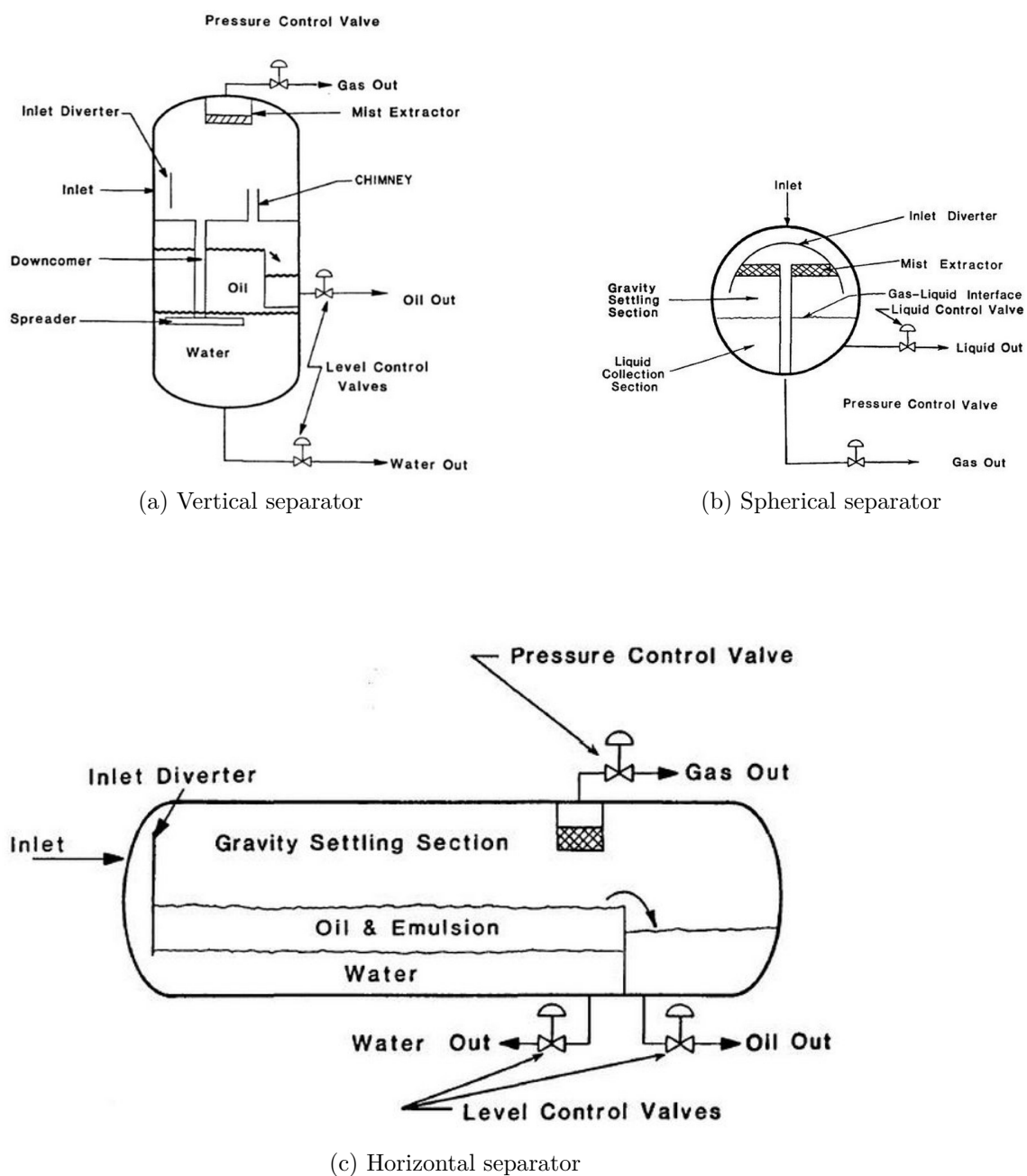


Figure 5.2: Multiphase separator configurations

is known as “free water”. The paraffin oil forms an “oil pad” on top of the water phase. In some cases emulsions can form due to vigorous mixing of the two phases. An emulsion requires a much greater settling time for separation to occur. There are different type of sensors to measure the thickness of the emulsion layer, for example differential pressure, capacitance, microwaves, ultrasound, etc. [32]. An increase in temperature and/or chemical agent assistance can aid in the prevention of an emulsion formation. Settling time (or retention time) is dependent on the experimental or field data and will generally range between three minutes and thirty minutes [1], however, the use of a wire mesh as a coalescer, can improve the separation process.

5.3 Positive Displacement Pumps

Oil and water flow must be derived in a precise composition formula. To achieve this, two gear pumps manufactured by Micropump Inc. [33] were chosen due to their accuracy, reliability and variable speed control. Gear pumps use the meshing of gears (as shown in Figure 5.3) to pump the fluid by the positive displacement principle. They are very accurate and allow for high pressures and liquid viscosities. Each gear pump provides a tachometer signal for feedback purposes, these signals were connected to a data acquisition card. The technical specifications for the gear pumps used are shown in Table A.1.

The gear pumps were first tested to verify their calibration characteristics. These tests were made by using a power supply with a fixed voltage of 24V while the control voltage was changed. At the same time, the frequency of the tachometer signal output was measured. The results of these tests are shown in Figure 5.4 and the plot in Figure

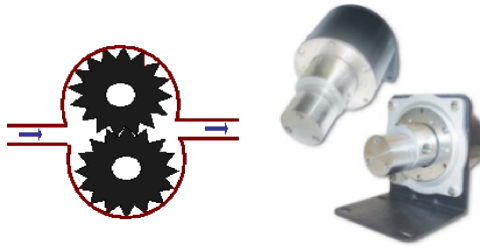


Figure 5.3: Gear pumps

V _{in}	Frequency [Hz]
0.5	7.16
0.75	16.91
1	26.23
1.24	35.3
1.49	44.31

Figure 5.4: Gear pump response

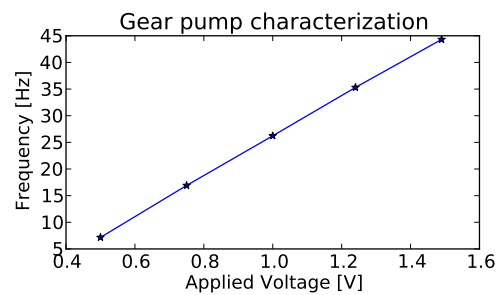


Figure 5.5: Gear pump response plot

5.5. The resulting equation that describes this behaviour is:

$$\text{Output frequency} = 37 * (\text{control_Voltage}) \left[\frac{\text{Hz}}{\text{V}} \right] - 10.85 [\text{Hz}] \quad (5.1)$$

5.4 Data Acquisition and Interfacing

In order to control the flow rate from each pump, it is necessary to apply a control voltage between 0 and 5VDC to the gear pump. This is done by using an ISA data acquisition card model PC30D DAQ card manufactured by Eagle Technologies. The access to this card is made through I/O operations. The default base address for this card is 700H and comprises of 32 byte locations.

The DAQ PC-30D has a A/D subsystem which consists of two 12 bits D/A converters (DAC0 and DAC1) and two 8 bit D/A converters (DAC2 and DAC3). The two converters used for the motor control were DAC0 and DAC1. These converters can be configured as 0+10V unipolar or $\pm 10V$ bipolar. For this application, both converters were configured for the 0+10V unipolar mode by setting the proper jumpers according to the Tables A.2 and A.3.

The relation between digital command and the output voltage from the DAC, for the 0 to +10 V range, is given by the following equation:

$$V_{DAQ} = \frac{(Digitalcode) * (10)}{4096} \quad (5.2)$$

from this equation, it can be obtained

$$Digitalcode = (V_{DAQrequired}) * 409.6 \quad (5.3)$$

The calibration flow loop was then implemented and the sensor data measured. During each test, the ratio of oil and water was changed, but the total flow rate was kept constant. This means that the speed of one pump will change from the minimum speed to the maximum, and at the same time, the speed of the other pump will change from the maximum speed to the minimum, but the total flow will remain the same. Tests under different flows can be performed by changing the maximum speed of the pumps. The maximum speed is specified at the beginning of the tests. In the code, the maximum speed is specified as a fraction of 5V (maximum voltage) and the output voltage is expressed as a fraction of this maximum voltage (Eq. 5.4).

$$DAC_{value} = (\% \text{ of maximum speed}) * (Maximum Voltage) * 4.096 \quad (5.4)$$

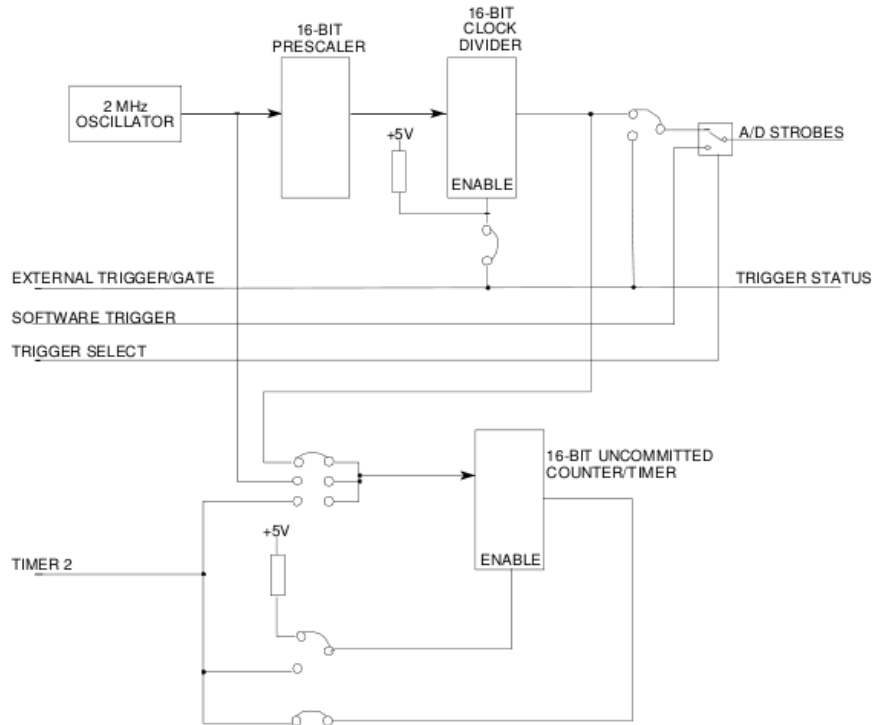


Figure 5.6: PC30D DAQ card timing and control section

5.5 Frequency Measurement

The PC30D DAQ has a timing and control section which comprises a 2MHz Master clock driven by a crystal oscillator, a 16 bit prescaler, a 16-bit clock divider and an uncommitted counter timer, which can be used for signal generation, or as a frequency or pulse period counter (Figure 5.6).

Since the tachometer signal generated by each pump has a low frequency it is not possible to measure it directly using the DAQ card, the period of the signal was measured instead, by using the next procedure: One prescaler was configured to divide the signal from the master clock by a factor of 10, and then divided again by a factor of another 10 generating a 20kHz signal which is applied to the counter.

The input signal from the tachometers should be connected to the counter enable input, however, there are two input signals, one from each pump, and only one input port for the counter. For this reason, the tachometer signals were connected to the digital inputs instead and the period was measured by using a polling-based method. The procedure to measure the frequency of the tachometer signals is as follows. The input signal is polled continuously and when it changes the polarity, the counter starts to count the pulses coming from the divider. The counter will continue working while the input signal changes the polarity twice again. At this moment, the counter is stopped and its value read from the User Counter Register. The value read from the counter is multiplied by a conversion factor of 0.00005 which is the period of the reference signal of 20kHz.

If the measured frequency is different from the targeted frequency, the control voltage applied to the pumps is adjusted. This process is repeated until the output frequency matches the required frequency (Figure 5.7).

5.6 Software

The complete calibration cycle was automated to ease the data logging over long periods of time and to assess the repeatability of the sensor in the end. The DAQ card was installed on a PC Linux system and the software for controlling the DAQ card was written in *C* language. The following algorithm was implemented for this purpose.

1. The maximum speed of the pumps is specified first.
2. The program then asks for additional parameters: the maximum percentage of water, the minimum percentage of oil, and the stepping increment.

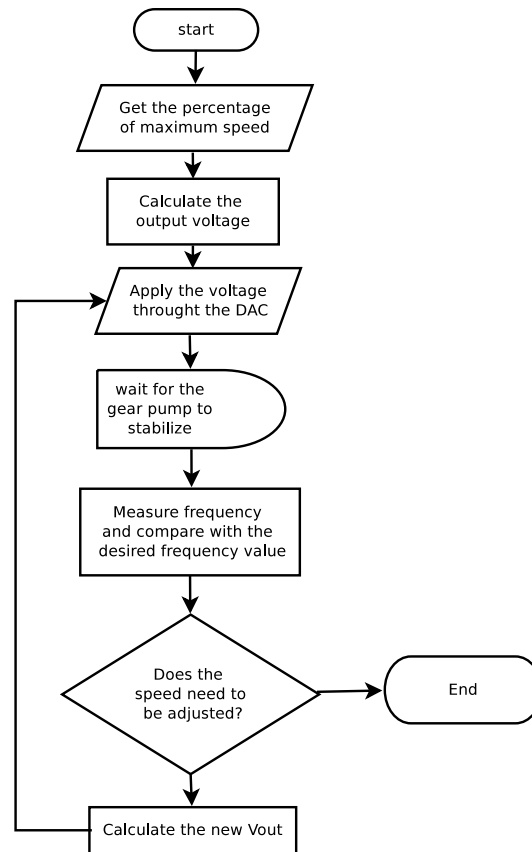


Figure 5.7: Gear pump control diagram

3. At the beginning of sensor calibration the oil pump operates at the minimum specified speed, and the water pump operates at the maximum.
4. Once the measurements have been taken, the oil speed is increased by a factor of the above stepping increment. At the same time, the speed of the water pump is decreased by the same factor, by doing this, the volumetric flow rate is kept constant.
5. Once the flow settles at the new setting rate, the sensor calibration measurements are performed followed by the speed of the pumps being adjusted again.
6. This process is repeated until the oil pump is operating at the maximum speed

(or maximum volumetric flow) and the water pump is operating at the minimum speed. The calibration data from the sensor are stored in a file for further analysis.

5.7 Conclusion

The flow conditions can vary during the oil production. In order to calibrate the sensor it is necessary to test it in a wide range of O&G compositions. Implementation of a compact flow loop allowed testing of the new sensor automatically. The automatic system is capable of running through the calibration process autonomously without operator's intervention for long periods of time. This setup will also enable the future experimental work on sensor robustness. The next Chapter describes the techniques employed in the sensor design as well as the first tests in which the flow loop was used as a calibration tool.

Chapter 6

Experimental Verification

6.1 Prototype #1

The first prototype built to verify the working principle of the developed sensor is shown in Figure 6.1. The inner core made of PVC has a conical shape and the electrodes were ‘painted’ using a silver-based conductive paint of very low resistance. Two guard electrodes located between the sensing electrodes were also painted and grounded. The external shell, made of aluminum, was also grounded. To prevent any conductivity issues, the inner core with painted electrodes was insulated using a transparent lacquer.

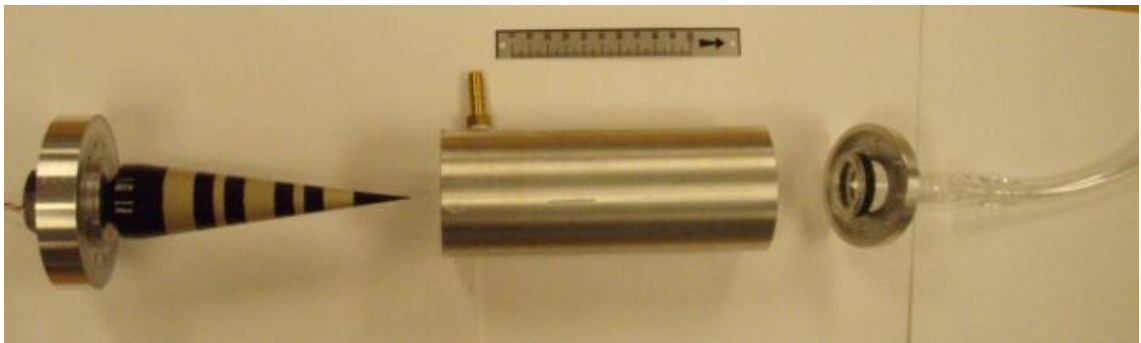


Figure 6.1: First sensor prototype

The capacitances were measured indirectly by two different methods, using a capacitive divider/half bridge and using a resonance frequency method, Sections 6.1.1 and 6.1.2.

6.1.1 Capacitive Divider/Bridge

In order to measure the capacitance of each electrode, the circuits shown in Figures 6.2 and 6.3 were constructed. An AC signal is applied to a voltage divider comprising of

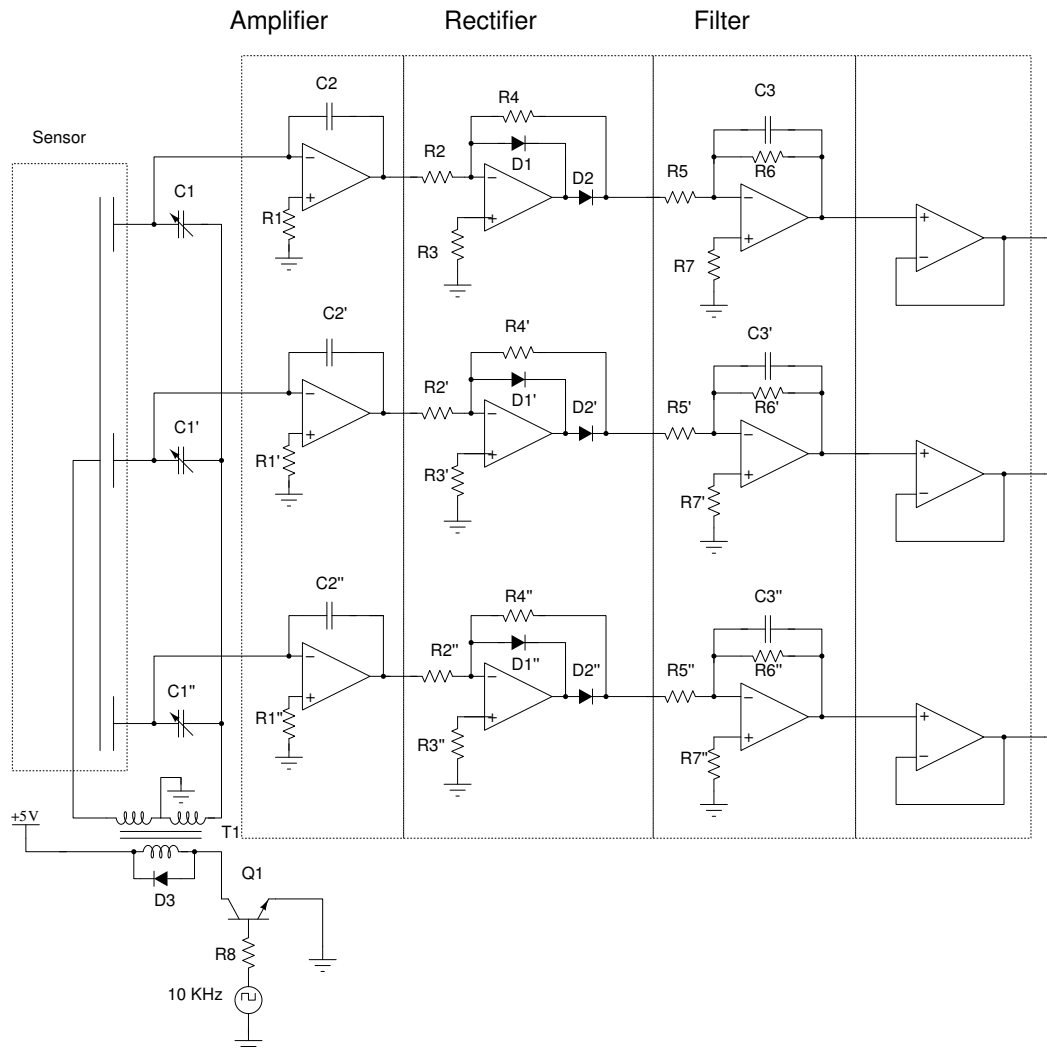


Figure 6.2: Circuits employing a square signal for capacitance measurements.

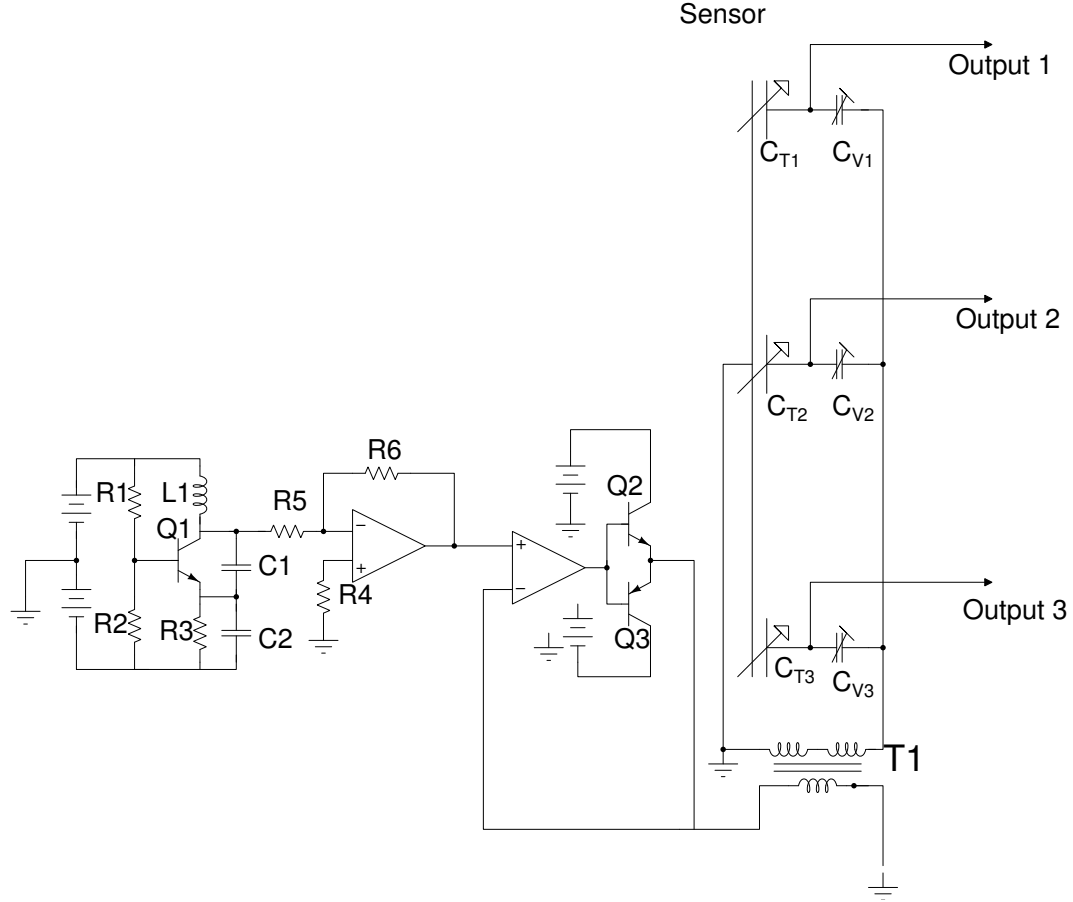


Figure 6.3: Circuits employing a sinusoidal signal for capacitance measurements.

two capacitive impedances. The first impedance is provided by a fixed value capacitor, the second one is the unknown capacitance of the sensor electrodes. The output of a voltage divider is given by the following equation:

$$\frac{V_o(j\omega)}{V_i(j\omega)} = \frac{Z_1}{Z_1 + Z_2} \quad (6.1)$$

This signal is then rectified and filtered in order to get the corresponding DC voltage. The experiment was performed with a square and a sinusoidal. The square wave was somewhat easier to generate but the sine wave produced a better quality output

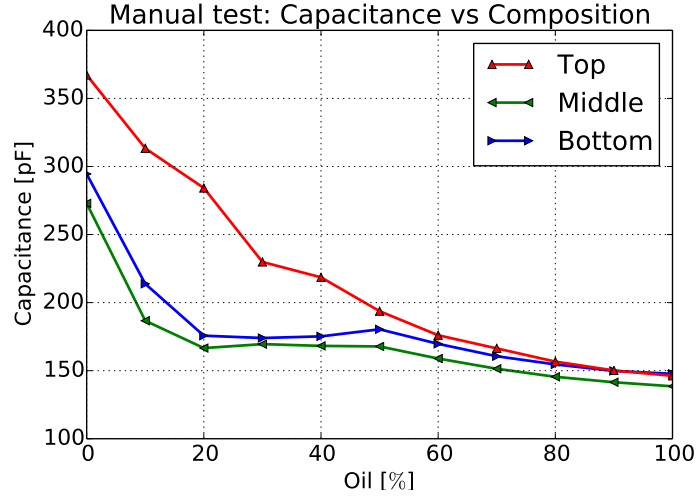


Figure 6.4: Calculated capacitances

signal. From this measured voltage the capacitance can be calculated as:

$$C_2 = \frac{(V_i - V_o) * C_1}{V_o} \quad (6.2)$$

the ratio of oil was increased by 10% in each increment and three runs 0% to 100% were performed. The results are shown in Figure 6.4.

The results obtained from this experiment demonstrate that there is a clear correlation between the ratio of oil to water and the measured and calculated capacitance. However, capacitance measurements made using an RCL meter showed that the electrode impedances had a real part or resistance in addition to the capacitance. Even though electrodes were covered with a layer of enamel and teflon tape, the real part of the impedance couldn't be suppressed completely.

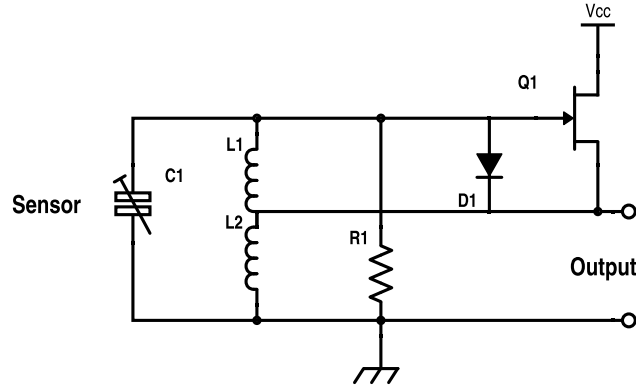


Figure 6.5: Hartley FET oscillator, source drive

6.1.2 Frequency Tests

In order to improve the measurement of the capacitance and make it immune to the effects of the real part of the impedance, a Hartley FET oscillator was employed (Figure 6.5). In general, frequency output sensing techniques tend to provide more noise immunity when the signal probe length effects are not negligible.

The implemented circuit generates a sinusoidal signal in which the frequency depends on the value of a fixed inductor and a variable capacitor (the sensor electrode pair). Any change in capacitance will result in a change in frequency, thus, the sensor electrodes were connected as a part of the circuit. Three oscillators were built in order to measure the three channels simultaneously.

An *Advantech PSI-1780U* counter card was employed to measure the frequency from the three oscillators simultaneously. The control of this card was written in *C*, and it was integrated as part of the existing program for controlling the flow-loop. The response from the sensor is shown in Figure 6.6.

From these results, the capacitance was calculated and compared against the numerical results from simulations in Femm42. The comparison is shown in figure 6.7.

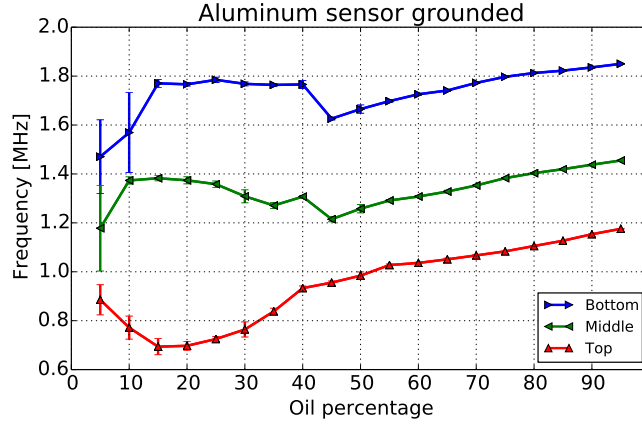


Figure 6.6: Frequency test results

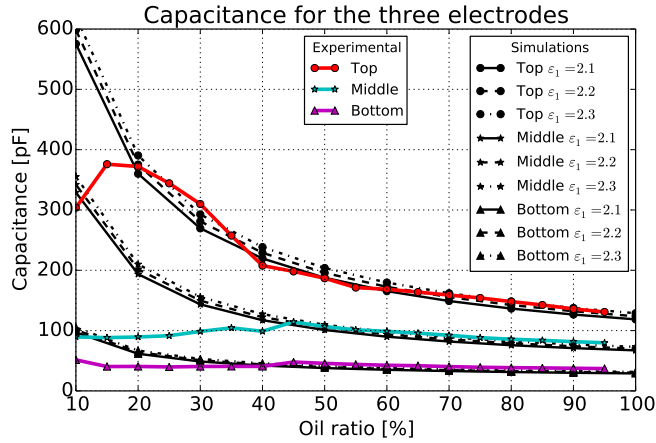


Figure 6.7: Practical results vs numerical simulation results

6.1.3 Temperature Test

One of the objectives of this work is to develop a sensor that is insensitive to drift in the electrical properties of the fluids. The temperature of the oil being extracted is determined, among other factors, by the proximity of the oil reservoir to the earth's mantle. According to the model provided by Malmberg *et al* [37], the electrical

permittivity of water decreases as the temperature increases. Since the analytical model of the proposed sensor shows that this sensor can be immune to changes in temperature, it was decided to test the sensor's response at different temperatures. For the purpose of this research, it wasn't desired to integrate a complete refrigeration unit with the flow loop due to space constraints (desktop setting), instead, a simple method was implemented. Since the thermal capacity of the flow loop was rather large, ice was added to the separator tank and performed several tests. After the initial drop in temperature, the temperature then started to gradually rise with a long time constant which provided enough time to cycle through the entire range of compositions at a nearly constant temperature each time. The temperature range for this test was 8.6 - 21.6C. In this range, the variations in measured capacitances was minimal, and further tests at higher temperature are needed. The result of this test are shown in Figures 6.8a, 6.8b, 6.8c.

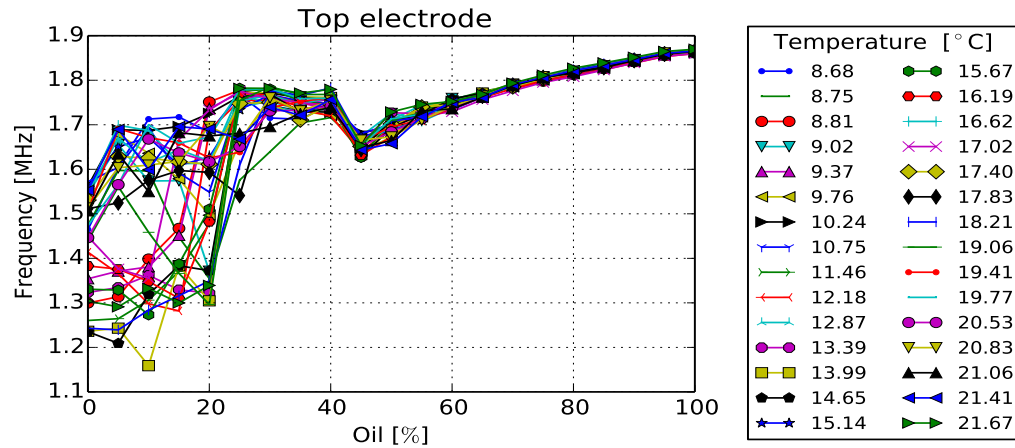
From the plots, one can observe that for low percentages of oil, the variability is higher, and for concentrations above 50% the characteristics is almost linear.

6.1.3.1 Air Test

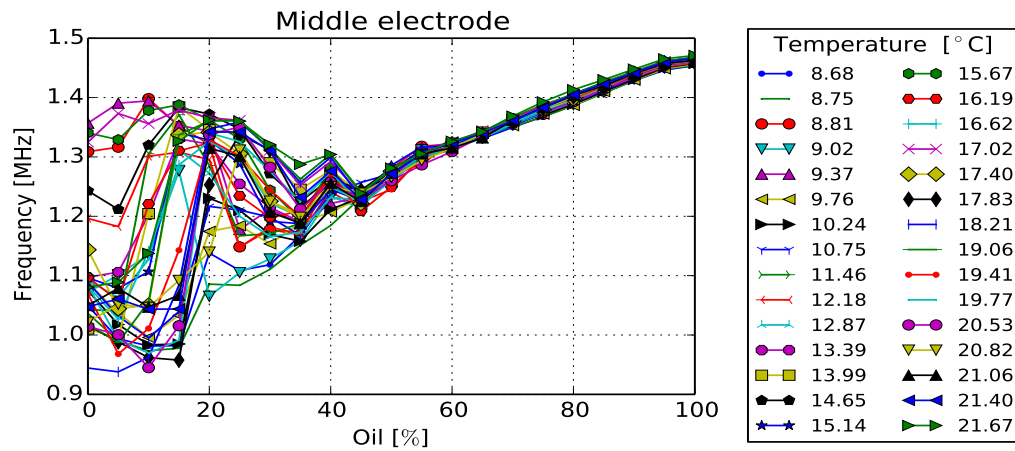
An additional test was performed in order to determine if this sensor is also suitable for three phase measurements. A DC air pump operated at 24V was employed to introduce air into the mixture of oil and water.

6.1.3.2 Air Pump Characterization

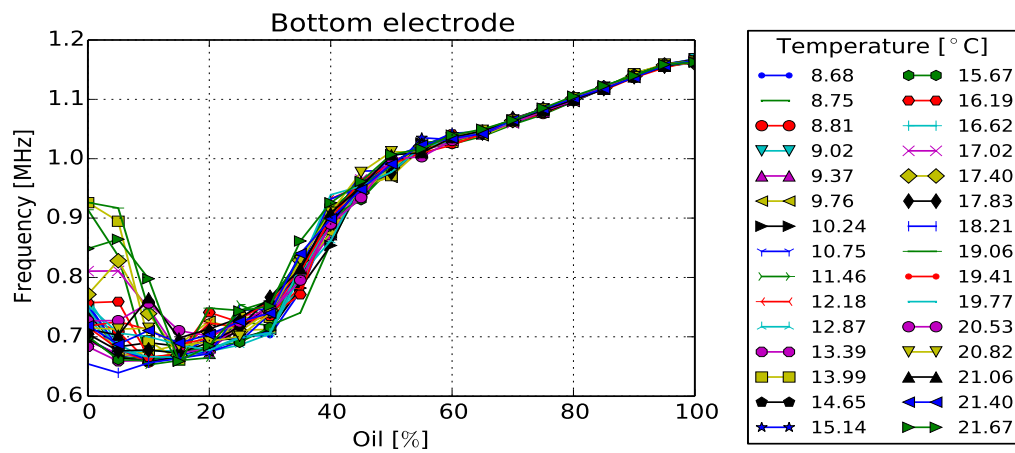
To accurately quantify the effects of introducing the gas phase into the multiphase flow it was needed to first calibrate the air pump. The relationship between the air volume and the pump control voltage is not unique as it depends upon the intake and output pressures. The intake pressure is constant in this case (1 atm) so only



(a)



(b)



(c)

Figure 6.8: Sensor response for different temperatures

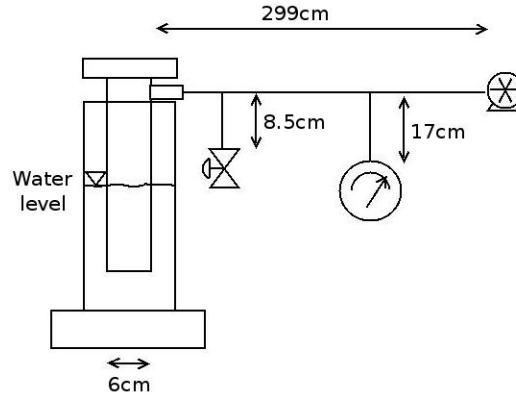


Figure 6.9: Air pump characterization setup

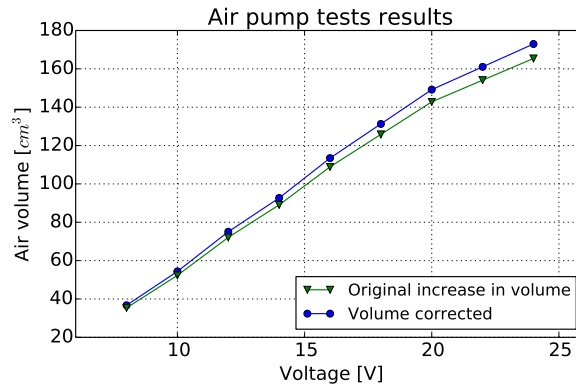


Figure 6.10: Air pump response

the correlation with the output pressure is necessary. The air pump calibration setup comprises the air pump, a manometer with a maximum scale of 15 PSIG (6 inches of water), a glass container with a scale for measuring the water level and a plexiglas container (Figure 6.9). The speed of the pump was changed by varying the applied voltage. The air pump was operated for a 4 second interval at varying speeds. The air was pumped into the glass container immersed inverted in water. As the air volume increases inside the container, the portion of the container above the water level rises. The difference in this raised level was used to calculate the pumped air volume. The increase in volume and pressure were used to calculate the total air volume pumped

(at the sea level). The pressurized air volume and the air volume at sea level are related by the Boyle-Mariotte law (Eq 6.3).

$$P_1 \cdot V_1 = P_2 \cdot V_2 \quad (6.3)$$

Figure 6.10 shows the response of the air pump for different applied voltages.

6.1.3.3 Air Pump Test Results

The three phase test was performed maintaining a constant pump speed and varying the ratio of oil and water. The responses of the three sensors are shown in Figures 6.11a, 6.11b and 6.11c.

The first prototype showed satisfactory results, however, the electrode impedance showed again a real part. The impedance with real part suggests that the applied coating absorbs some water. To prevent such effects and isolate the conductance from the capacitance, a transformer wire was used in the second prototype because of its high quality enamel insulation. A small scale set up was constructed in order to test the response of the coils used to measure capacitance. The next section describes a static test using transformer wire electrodes, followed by experiments on the second flow meter prototype.

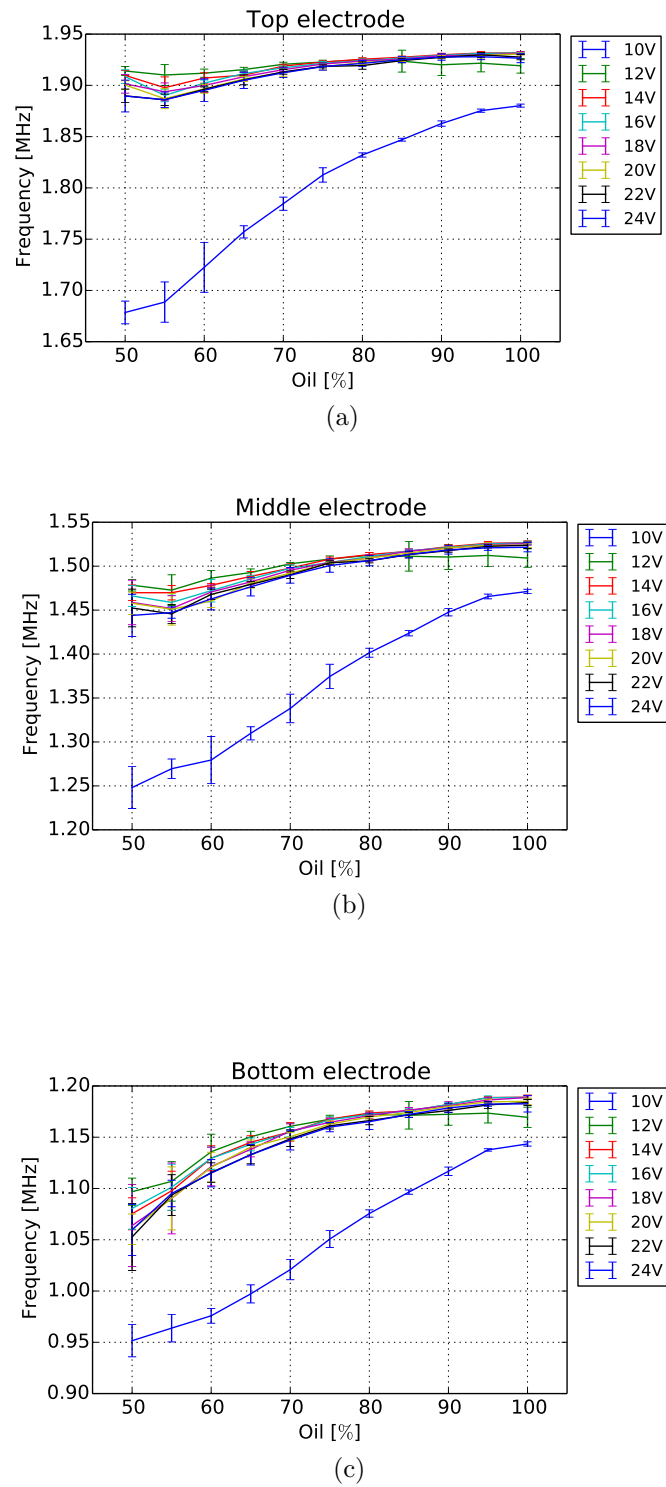


Figure 6.11: Sensor response for varying air ratios

6.2 Capacitive Static Tests

6.2.1 Capacitive Test With a Single Coil

In order to simulate a complete separation of a two phase flow, a small scale static (i.e. no flow) setup was constructed. It consisted of 250mm (ID) x 500mm (L) steel pipe, and 60mm (ID) x 500mm (L) plastic pipe, and a coaxial conical membrane which separated the space between the pipes into two compartments to contain the oil and water phase separately. Inside the inner plastic pipe was placed a black PVC pipe (54.5mm OD) that could move freely along the vertical axis. This second PVC pipe had a coil of 80 turns of 32 AWG with an impedance of $371.5 \mu\text{H} + 7.98 \text{ ohm}$ (Figures 6.12 and 6.13).

The two chambers were filled/emptied to produce a range of different phase combinations of air, water and oil. For every combination of gas/liquid or liquid/liquid, the inner pipe was moved vertically, simulating a change from 0% to 100% in composition. For every increment along the vertical axis, the capacitance

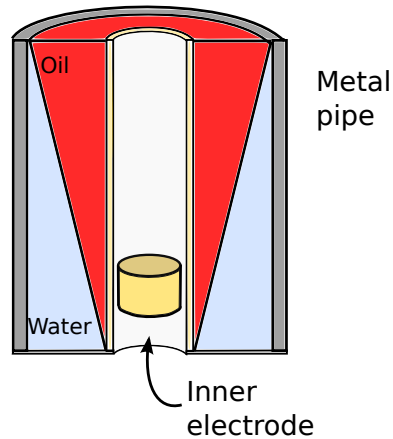


Figure 6.12: Capacitance measurement with a single coil and a metal pipe.



Figure 6.13: Capacitance measurement with two coils and a plastic pipe.

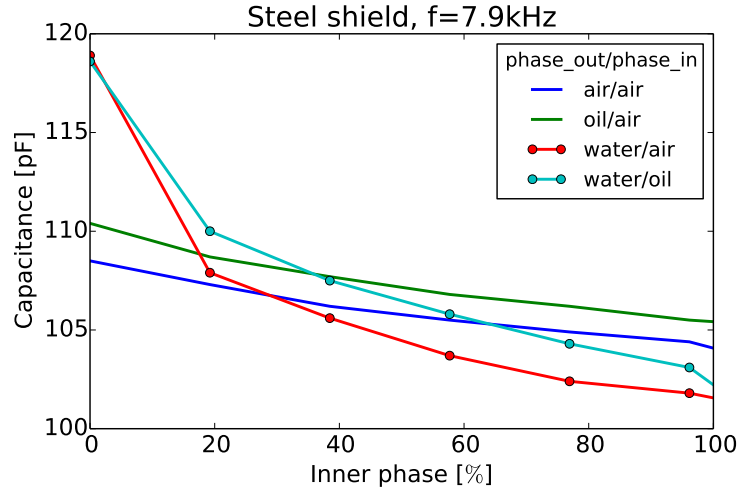


Figure 6.14: Capacitance measurement with two coils and a steel pipe.

was measured using a FLUKE RLC meter PM6306 in C+R parallel mode at 7.9kHz, the results of these tests are shown in Figure 6.14.

As can be seen in the figure, as the the liquid or gas with the lower permittivity increases in volume, the total capacitance decreases. It can also be seen that when there is air in both sections of the sensor, the capacitance change as well. This can be explained by the fact that the plastic separation between the two sections is spatially drifting along the vertical axis.

6.2.2 Capacitive Static Test With Two Coils

Another experiment was performed with the outer electrode modified from the previous experiment in order to simulate a non-conductive cyclone body with a discrete non-grounded electrode. The electrode was constructed as previously by winding a coil element in a single layer of 31 AWG wire and 20mm long. This external electrode slides vertically in sync with the inner electrode (see Figures 6.15a and 6.15b). The outside chamber contained water and the capacitance was measured for either air or

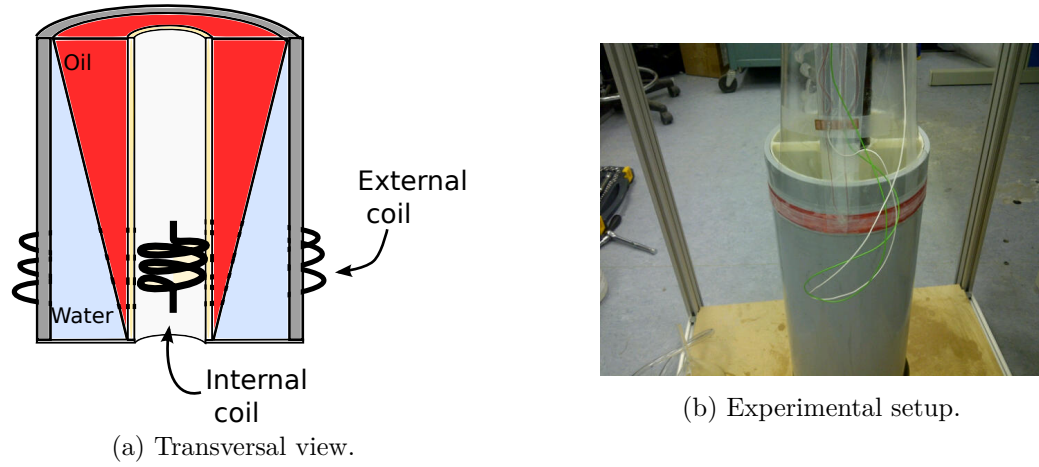


Figure 6.15: Capacitance measurement with two coils and a plastic pipe.

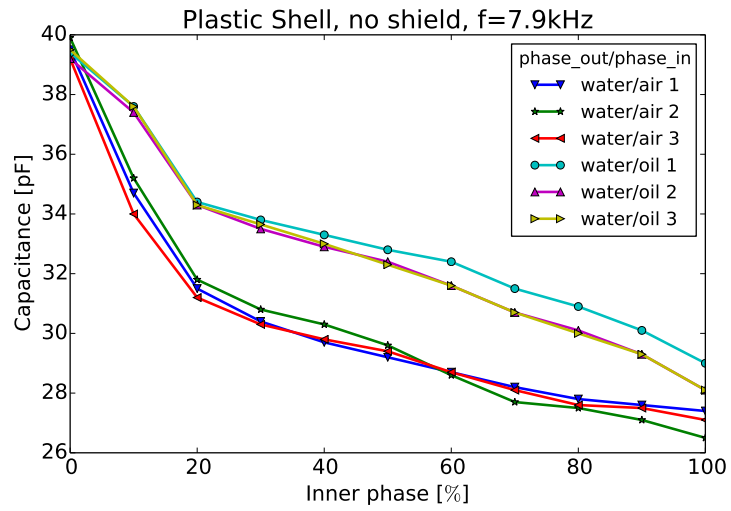


Figure 6.16: Capacitance measurement with two coils and an unshielded plastic pipe

oil as the other phase. The results are shown in Figure 6.16.

It can be observed that the measured characteristics are nearly identical to the previous case when only one coil was used and the capacitance was measured against the steel pipe.

6.2.3 Capacitive Static Test With Two Coils and a Metal Shield

A similar experiment was conducted, but this time the external coil was covered with a 6" wide brass shim foil wound with insulation foil under (to avoid shorted loop) over the outside coil, as it is shown in Figure 6.17, the results are shown in Figure 6.18. In fact, there is not much difference when the shield is grounded and when it is not, and also the range of variation is smaller than in the previous cases.

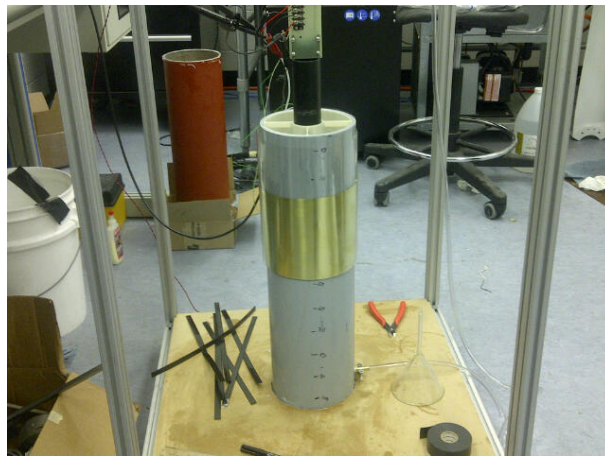


Figure 6.17: Capacitance measurement with two coils and a shielded plastic pipe

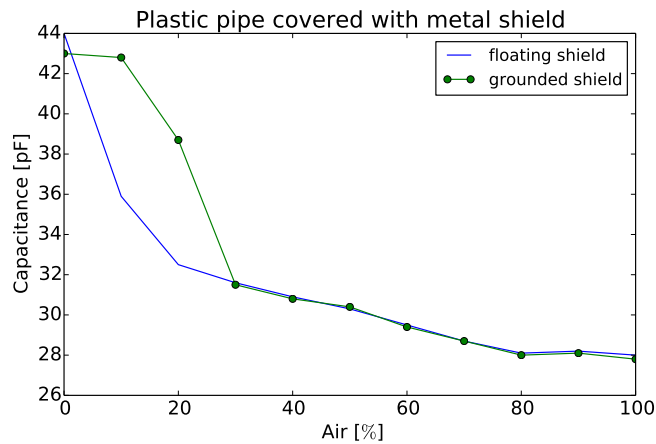


Figure 6.18: Capacitance measurement results with two coils and a shielded plastic pipe

6.3 Prototype #2

6.3.1 Hydrocyclone

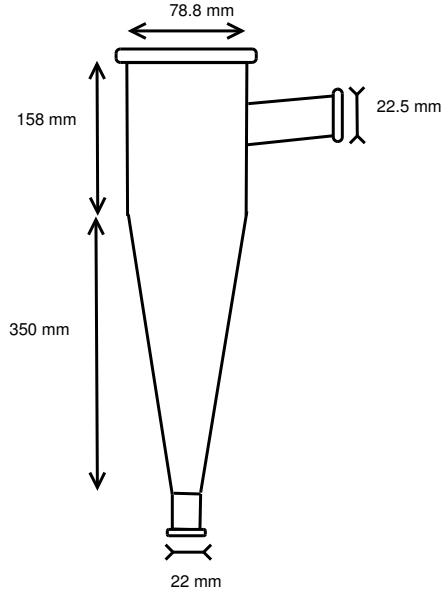


Figure 6.19: Hydrocyclone dimensions.

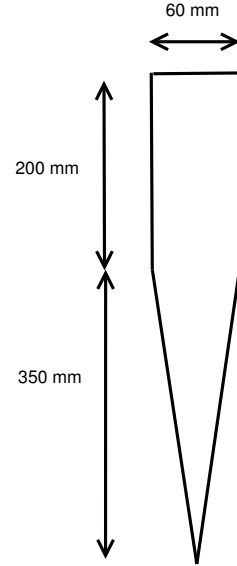


Figure 6.20: Hydrocyclone insert.

The second prototype of a multiphase flow meter was built in glass in order to observe by visual inspection the level of flow stratification within the hydrocyclone. The hydrocyclone employed was based on Dabir's hydrocyclone design and was made at the glass blowing shop of Technical Services at Memorial University (Figure 6.19) [4]. In order to support the inner electrodes, a new glass insert (Figure 6.20) was built, and mounted inside the hydrocyclone.

6.3.1.1 Capacitive Test

In the first test, a stack of electrodes was placed along the hydrocyclone core (as seen in Figure 6.21) and two additional coils were mounted on the outside. Initially, the capacitance was measured between the electrodes when the hydrocyclone was filled



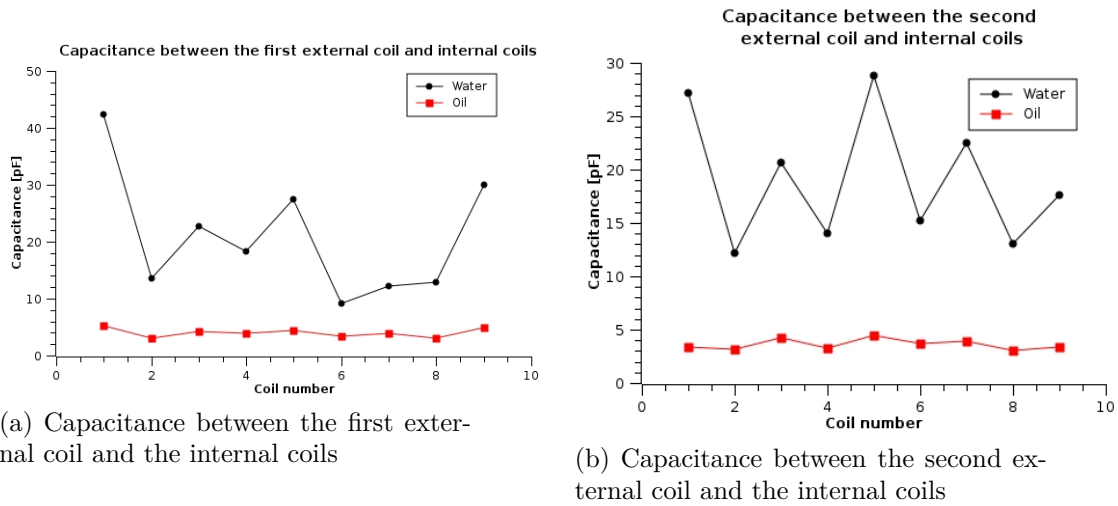
Figure 6.21: Hydrocyclone insert with inner coils

entirely with water and then when oil was substituted for water. These measurements are plotted in Figures 6.22a, 6.22b and 6.22c.

In the first automatic test, the oil ratio was changed from 5% to 95% in increments of 1%. The results of this experiment are shown in Figure 6.23.

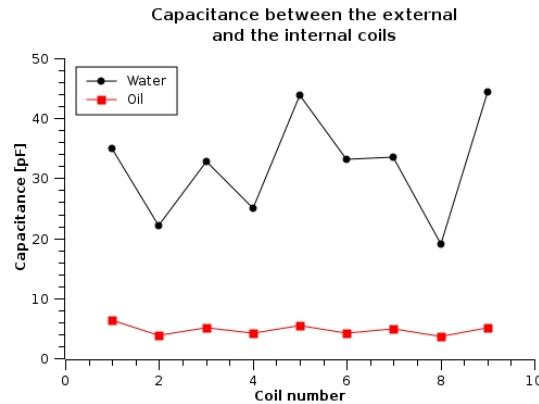
The experiment demonstrates that it is possible to apply the capacitive method by using coaxial coil electrodes as if they were coaxial ring electrodes. The coaxial coil electrodes opens a new possibility to apply them along with the LVDT principle outlined in Chapter 2.

If the external coils are embedded into the cyclone's outer wall, that needs to be made of an insulator material, it could be possible to measure the water phase velocity by the above mentioned LVDT principle. It is convenient as the water phase is accumulated at this side of a cyclone chamber. The flow within the cyclone is a complex matter but for the process information purposes, the total volumetric throughput which is represented by the axial component of the flow velocity is of interest. This is also the component measured by LVDT method. This study was outside of the scope of the current work and will be investigated in the future.



(a) Capacitance between the first external coil and the internal coils

(b) Capacitance between the second external coil and the internal coils



(c) Capacitance between the two external coils and internal coils

Figure 6.22: Capacitance between electrodes

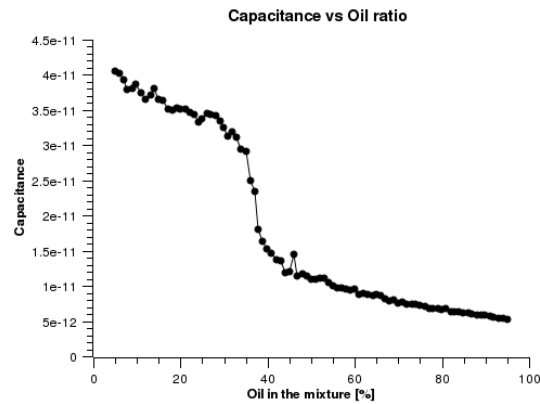


Figure 6.23: Capacitive test 1 in prototype #2

6.3.2 Signal Attenuation Study

Since the capacitive sensor electrodes were constructed as being de facto a solenoid coil each, it was of interest to test a hypothesis of using the Faraday's principle of EMF induction in a conductive liquid phase that forms an annular loop circuit. The only difference was in configuring/connecting the coil (electrode) leads and in the measuring instrumentation. As a hypothesis, it was assumed that the different volume of the conductive water phase creates different level of attenuation in the opposing secondary coil signal. This can be explained as the current induced in the annular water phase establishes a secondary magnetic field that opposes the primary field. Therefore, the resulting secondary signal (voltage) shall decrease with the increase of the water phase.

In order to achieve good measurement resolution, a limited frequency analysis was carried out prior to conducting the above outlined study. The characteristic in which the signal coupling level increases with the applied frequency was measured, however stopping was necessary above 3MHz due to the instrumentation limits. The coils were characterized using RLC meter Fluke PM6306 (this data is listed in Table 6.1). Therefore a 3MHz sine signal from a signal generator was used to excite the primary coil while the RMS voltage of the induced signal in the secondary coil was measured by an oscilloscope. For the first tests, the middle internal coil was used as excitation coil and one of the external coils was used as a detection coil.

The results of this experiment (Figure 6.24) show that the amplitude of the output voltage decreases as the ratio of oil increases. At first glance no problem was seen as the composition axis label had been unintentionally read as the water cut percentage and thus conducted a new automated experiment to further advance this study.

Measurement of inductance @ 1MHz			
External coil [μH]		Internal Coils [μH]	
Upper coil	614.8	L1	29.83
Lower coil	182	L2	11.26
		L3	14.92
		L4	13.18
		L5	27.61
		L6	9.82
		L7	19.62
		L8	6.99
		L9	12.15

Table 6.1: Coil Inductance Values

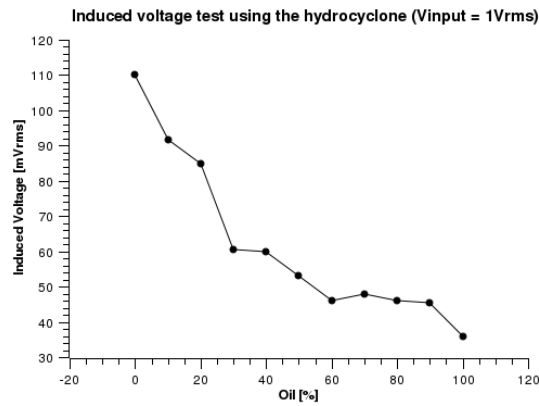
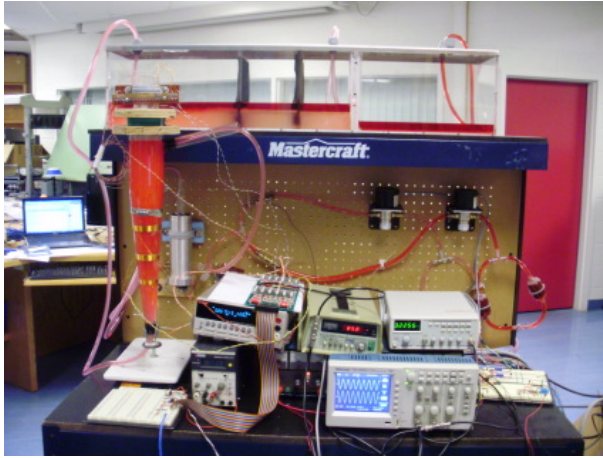


Figure 6.24: Attenuation manual test

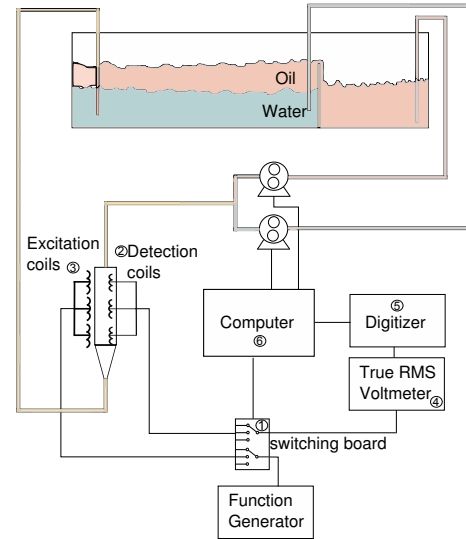
6.3.3 Automated Attenuation Test

For the automatic inductive test, the experimental setup shown in figure 6.25 was used. In this experiment three pairs of coils were used. A computer controlled reed-relay card (1) was switching the excitation signal to the excitation coil array to make only one relay active at a time, and also, to measure the induced voltage in each detection coil.

The excitation signal was applied at the internal coils (2) and the induced voltage was measured on the external coils (3). Since the detected signal had a frequency too high to be measured by a standard voltmeter, a Fluke True RMS Voltmeter (4) was used.



(a) Actual setup



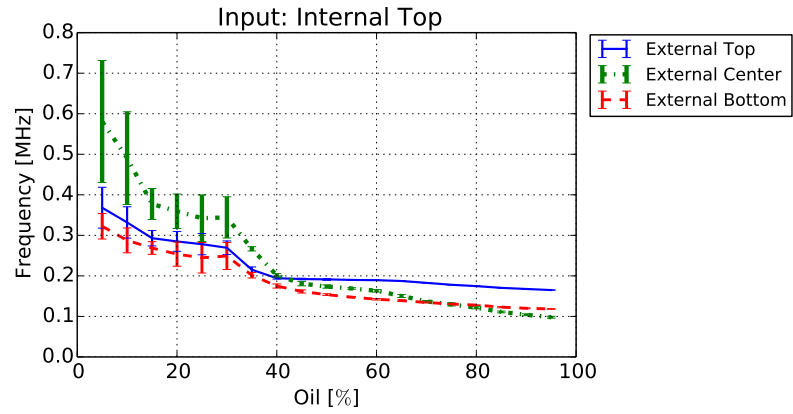
(b) Experimental setup diagram

Figure 6.25: Experimental setup

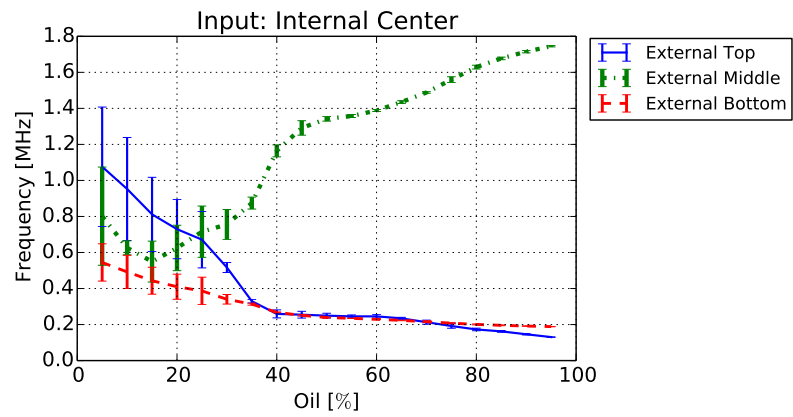
This device, besides measuring accurately the RMS voltage, generates a DC signal which has the same value as the RMS input signal. This DC signal was digitized through a Keithley data acquisition system (5), and the digital data were sent via serial port to a PC for storage and analysis (6). The results of this experiments are shown in Figures 6.26a, 6.26b and 6.26c.

The results obtained when the top internal coil is excited are shown in the Figure 6.26a. It can be observed that the output voltage for the three external coils decreases when the ratio of oil increases, in the same manner as in the first manual test.

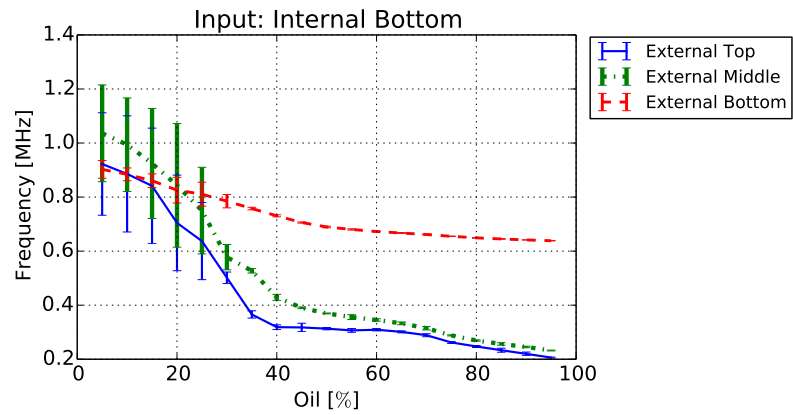
Figure 6.26b shows the output voltages when the excitation signal is applied to the middle internal coil. For the upper and lower detection coils, the amplitude decreases, as expected; however, the voltage at the middle external coil showed a different response. The output voltage showed a decreasing tendency for low oil concentrations and reached a minimum, after which, the phase voltage changed and the amplitude started to increase again.



(a) Internal Top Electrode



(b) Internal Middle Electrode



(c) Internal Bottom Electrode

Figure 6.26: Automated test results

It was realized after this run of automated tests that the initial hypothesis was not confirmed. Further evaluation revealed that the signal coupling effect was a result of the parasitic capacitance between the two coils and as such the characteristics are similar to those obtained in the capacitance measurements.

6.4 Conclusion

A wide range of testing conditions and instrumentation methods was applied to test the fundamental principle of a multiphase flow (composition) meter. Two prototypes were used, and quantitatively different signal detection techniques were applied in each measurement. Automating the data collection was a significant part of this work as these experiments are very complex and very lengthy in time. The theoretical principles of signal transduction as been proven yet the case of robustness is left for future work. This study would require a significant modification to the calibration flow loop, introduction of permittivity modulation to model the parameter drifting, which was beyond the scope of this work.

Chapter 7

Flow separation study

7.1 Introduction

The experimental results in previous chapters show good repeatability for high oil concentrations. However, the same experiments show that the sensor have a low performance for high water concentrations in the mixture. A possible explanation for this problem is that the oil and water were not separated completely. During a test with a high water content, there are oil bubbles that when they pass between the electrodes, the capacitance decreases greatly for a short period of time, after the oil bubble passes the electrode, the capacitance increases again. If the mixture contains many oil bubbles, the capacitance value will change constantly. In order to determine if the oil is separating properly, spreading itself around the core in a thin layer, a flow visualization technique was needed. This chapter starts by describing the most common types of flow visualization, and then explains the technique implemented in this research. This test was complemented with a Computational Fluid Dynamics (CFD) simulation of the liquids inside the hydrocyclone. Finally, a new approach to the hydrocyclone flow separation using an external motor is presented.

7.2 Flow visualization

A limited flow visualization technique was conducted to gain an insight into the flow pattern especially at the high water concentrations at which the large measurement uncertainties were observed. Flow visualization is used to study particle trajectories in a fluid flow. A flow visualization method basically refers to the observation of tracer particles in order to get quantitative and qualitative information. These particles can be solids, liquids or gases. Some of these methods can not be used for a long time, since the liquid eventually becomes contaminated by the solid particles or the liquid tracer making it difficult to observe. Methods involving gaseous tracers are more complex to implement but they have the advantage that they can be used repeatedly, without contaminating the fluid. Examples of methods involving a gaseous tracers can be smoke wire and hydrogen bubbles. Both methods are in the category of electrolytic techniques. The smoke wire method is used when the fluid is oil; in this method a wire immersed in the liquid heats the oil and generates bubbles. When the circuit is pulsed, successive lines can be produced following the flow pattern. The hydrogen bubble method, is an electrolytic technique in which one electrode generates very small hydrogen bubbles. This method has several advantages, among them, this method is low cost, easy to implement and can be used repeatedly without much troubles. This is the technique that was employed to visualize the flow pattern inside the hydrocyclone in this research. The next subsection describes this method in more detail, the setup employed and the results obtained in this project.

7.2.1 Electrolytic Flow Visualization

The hydrogen bubble visualization is a simple and low cost method for flow visualization. This method consists of generating hydrogen bubbles by an electrolysis

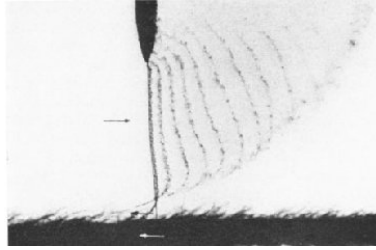


Figure 7.1: Pulsating hydrogen bubbles [36]

process in a water flow. The bubbles are generated by a very thin electrode, usually of 25-50 μm in diameter. This electrode is connected to a negative voltage, and the anode is connected to a larger piece of metal or carbon electrode connected nearby. If the polarity of the power supply is reversed, small oxygen bubbles will be generated. Since the water molecule is H_2O , the number of oxygen atoms is half the number of hydrogen atoms per molecule of water, and as a result, the volume of oxygen bubbles will be smaller. The electrolytic technique has proved to be low cost and easy to implement. If a pulsating voltage is applied, several lines of bubbles will trace the local velocity vector (see Figure 7.1). If light is applied properly, this method can, in combination with a good image capture processing system, help to generate a great amount of qualitative and quantitative data [35].

7.2.2 Experimental Setup

The goal of applying the electrolytic technique was to measure the angular flow speed inside the hydrocyclone. Since the hydrogen bubbles remain visible for a short time before they dissolve in the water, it was necessary to add more electrodes along the hydrocyclone. With this purpose, four ports were added to the hydrocyclone. These ports, that allow the insertion of electrodes for bubble generation, were placed as shown in Figure 7.2. In order to implement a flow visualization technique, a 13mm ($1/2\text{in}$) flow loop was implemented, at the research laboratory (Figure 7.3). Different

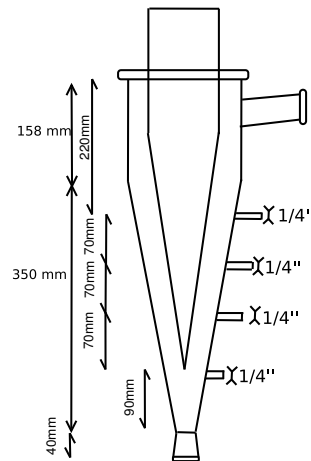


Figure 7.2: Hydrocyclone modified for flow visualization

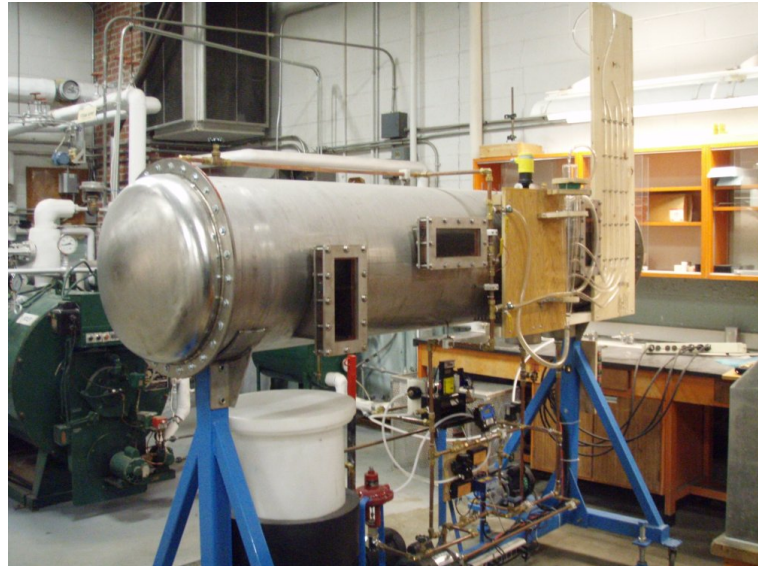


Figure 7.3: Three phase flow loop.

attempts with different power supplies were performed to implement the electrolytic technique, and finally it was decided to built a new power supply since the required voltage was higher than the voltage provided by the available power supplies (Figure 7.4).

Since the bubbles generated dispersed in a short period of time, it was not possible to track them from the port where they were generated until the hydrocyclone outlet. In

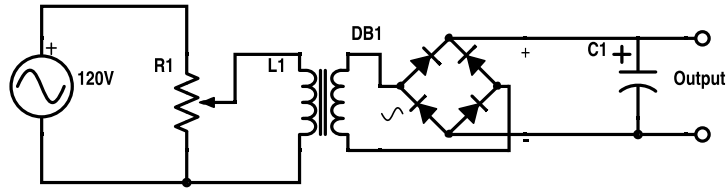


Figure 7.4: Power supply for flow visualization



Figure 7.5: Hydrocyclone with electrodes for electrolysis

order to track the bubbles properly the bubbles were generated periodically at different points along the hydrocyclone. The bubbles inside the flow were video recorded at 24 fps. The generated videos were edited and a time stamp was added to each frame. Based on the time stamp from the videos, it was possible to measure the time that it takes for a single bubble to give one turn inside the hydrocyclone (Figure 7.5). The times for many bubbles from the different ports were taken at different flow rates. The different angular speeds were calculated based on those times. The calculated speeds for the different tests are shown in Figure 7.6.

Since inside a hydrocyclone, as the flow speed increases, the pressure decreases by venturi effect, it should be possible to use the same hydrocyclone to determine the flow

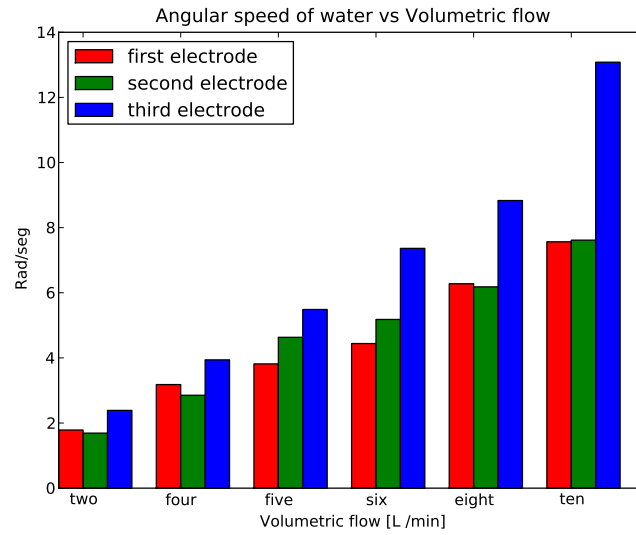


Figure 7.6: Angular speed registered inside the hydrocyclone

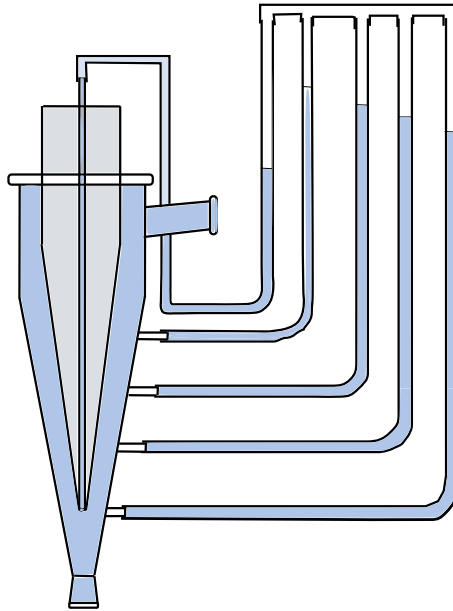


Figure 7.7: Hydrocyclone port configuration for differential pressure measurements.

velocity. This possibility was not developed in this research, however, an additional port was added inside the inner cone of the hydrocyclone for differential pressure measurement. The setup configuration for these measurements is shown in figure 7.7.

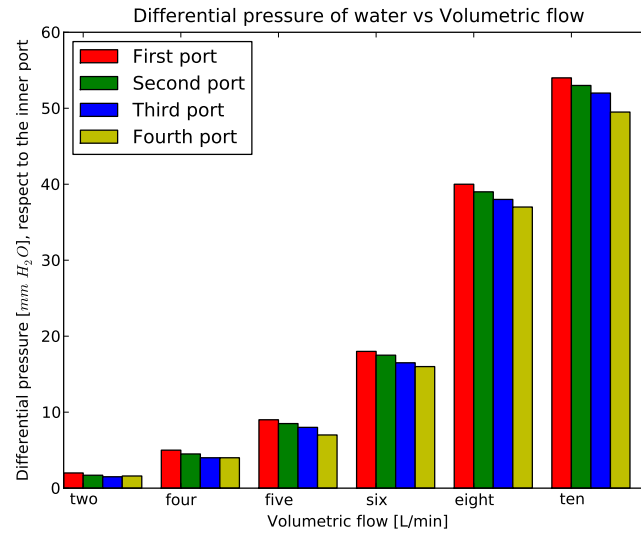


Figure 7.8: Differential pressure registered in the hydrocyclone

The differences in a water column for the different ports, referenced to the center port are shown in Figure 7.8.

7.3 CFD simulation

In order to have a better understanding of the separation inside the hydrocyclone a computer simulation was needed. The selected software for preparing the simulation was OpenFOAM. OpenFOAM is an open source software for computational fluid dynamics. The model used in the simulation had the same dimensions as the aluminum prototype tested before. Since OpenFOAM is only a CFD simulation software, other software was needed for pre-processing files for simulation and for analyzing the results. The CAD software used to create step files for this simulation was freeCAD, which is also open source. After the step files were generated with freeCAD, they were processed with Salome for mesh generation. Salome is an open-source software that provides a platform for pre and post processing for numerical simulation. In the

initial state of this simulation, it was assumed that the flow sensor was filled with water. The simulation was run only for one single composition that corresponds to 50% of oil and 50% of water. The speed of the liquids in this simulation was $1 \frac{m}{s}$. The total simulated time was 1.3 seconds, which was enough to reach a steady state of the flow inside the sensor. The software used for data analysis and visualization was ParaView, which is also open source.

From the analysis of the simulation, it can be seen that the flow seems to be separated on the bottom half of the hydrocyclone (see Figure 7.9. However, from the transversal view of the hydrocyclone, it can be seen that even when it seems that the oil covers the inner core at the bottom, there is still some water close to the core (Figure 7.10). From this simulation, it can be concluded that the electrodes should be placed in the bottom half of the hydrocyclone, and also that the bottom electrode should not be placed close to the end of the inner core. It can also be concluded that this type of simulations can help to optimize the design of a hydrocyclone to obtain the best shape

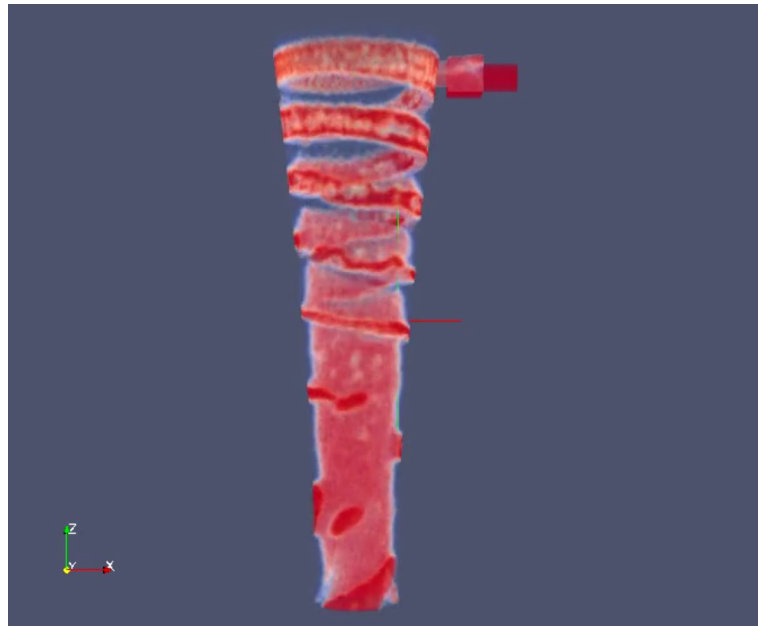


Figure 7.9: Flow simulation with OpenFOAM.

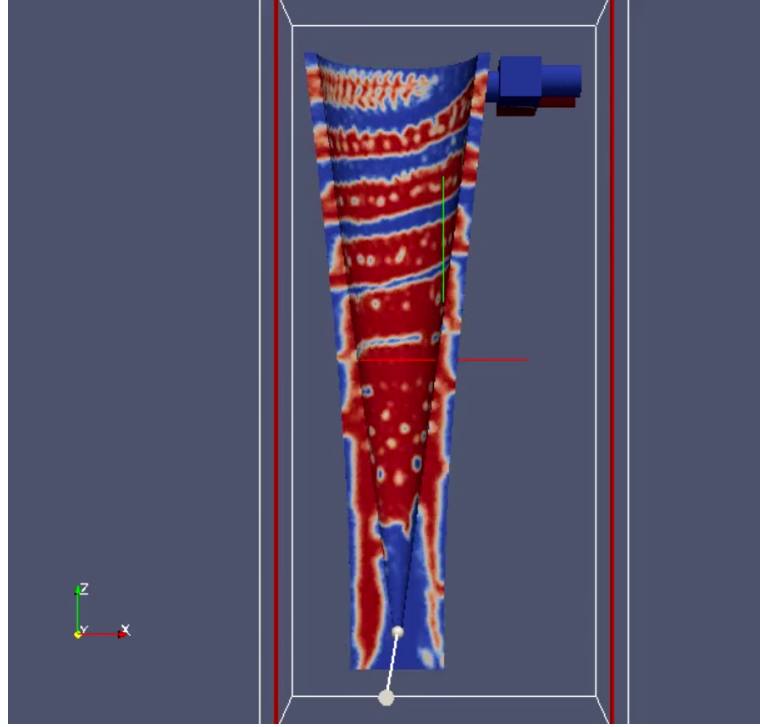


Figure 7.10: Transversal view of the sensor during the simulation.

of hydrocyclone, and select the range of velocities that are most suitable to achieve the best separation.

This simulation was run in a Linux system, and the processing time to simulate 1.3 seconds was 5 weeks. Since the simulation require a long time, some other solution was proposed to achieve better flow separation. This solution is described in the next section.

7.4 Turbo-cyclone

In this research, initial work has been done regarding a hydrocyclone concept that works independently of the flow velocity, a so called turbo-cyclone. This device boosts the centrifugal effect using a spinning agitator. A novel turbo-cyclone concept that rotates its outer shell as opposed to the conventional centrally positioned agitator has

been prototyped. Two objectives have been kept in mind: (A) to improve the energy transfer rate into the flow, and (B) to allow ‘bleeding’ of the oil phase through the axial conduit, as well as place the sensing electrodes on a non-rotational part of the system.

Conventional turbo-cyclones employ a stirrer or agitator in a form of a paddle wheel or propeller placed inside of the tapered chamber. This makes the drive shaft sealing simple. The chosen design uses an outer spinner concept which demands more sophisticated sealing both on the top and the bottom part of the conical chamber. A 3D printer was used to rapid prototype the turbo-cyclone design as shown in Figures 7.11-7.13. The parts were built nearly instantaneously in comparison to the conventional machining processes; however, the polygonal approximation of round surfaces was found difficult to fit together and seal. This was a major problem during the testing that led to excessive leaking (Figure 7.14).

Because of the leaking problems, only a few tests were performed. In these tests, the top electrode showed random measurements, that indicate poor liquid separation.

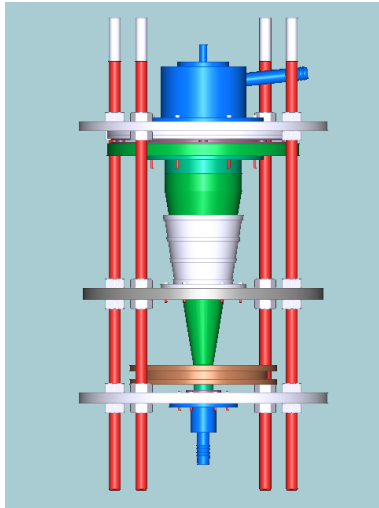


Figure 7.11: Prototype sensor frontal view

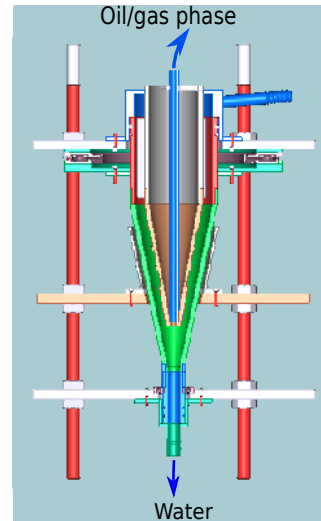


Figure 7.12: Transversal view of the proposed sensor



Figure 7.13: Frontal view of the prototyped sensor

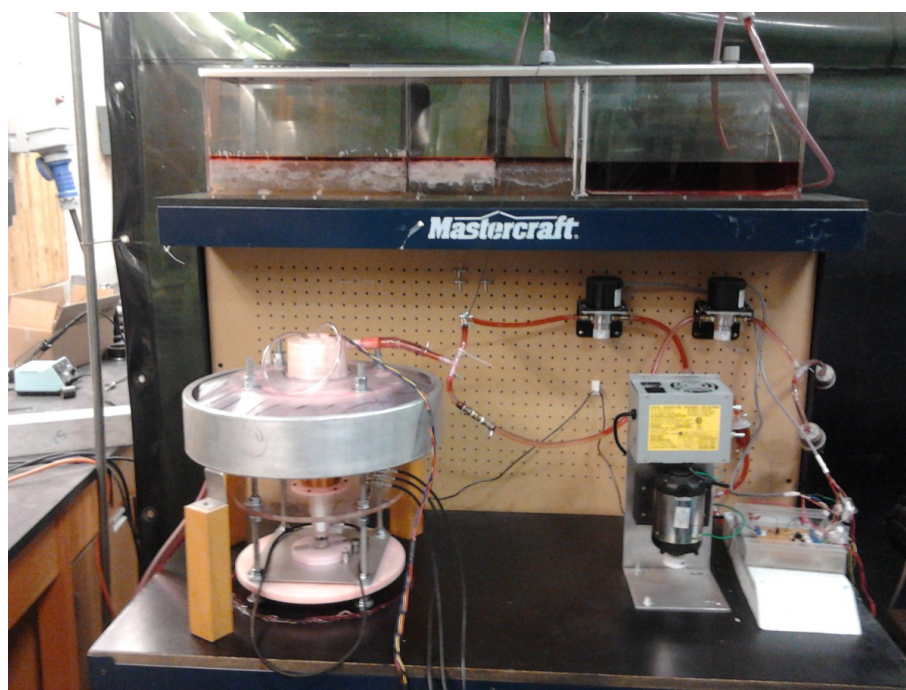


Figure 7.14: Prototyped sensor mounted on the flow loop.

The middle and bottom electrodes showed a response similar to the previous prototypes. At frequencies below 2MHz, the signal decreases for higher water content, and increases for high oil concentrations. At higher frequencies, the response of the electrodes seems to be the opposite. This seems to be due to the fact that there is a small capacitance across continuous turns of wire in a coil. At higher frequencies the accumulated capacitive effect increases and the behavior of the coil is predominantly capacitive. The plots showed in figures 7.15-7.17 represents the electrodes responses at 400kHz, whereas the figures 7.18 to 7.20 shows the response at 6MHz.

Since this prototype presented many problems, new prototype is being currently built using conventional methods. To make the developed sensor more practical and commercially attractive, a larger prototype tested on a larger calibrating flow loop is necessary. The Memorial University's academic collaborator, the College of the North Atlantic (CNA) built in past one of the world's largest multiphase flow loop that recycles all three phases involved: water, oil and nitrogen gas. This makes this 75.1mm (3in) diameter flow loop very unique and attractive. The research team will seek a partnership with a local industry to develop a full size prototype that can be tested on the CNA flow loop.

7.5 Conclusion

The study outlined in this chapter, suggests the need for a flow independent hydrocyclone process. A CFD simulation showed the need for better flow separation. A novel concept of a turbo-cyclone was implemented, however, due to numerous mechanical problems and leaks, the data gathered were inconclusive. The calibration will need to be reiterated in the new setup planned in the future.

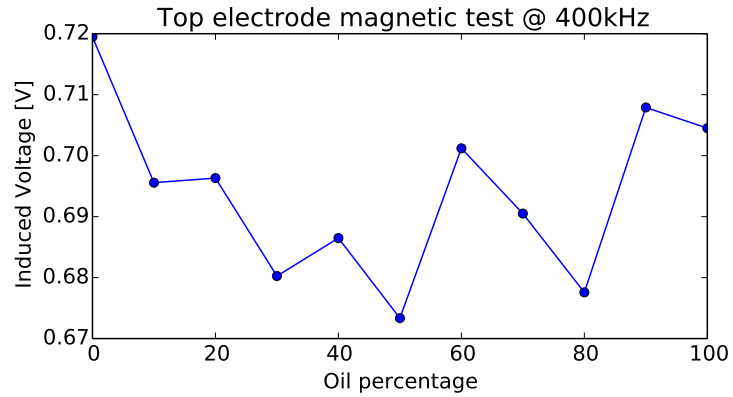


Figure 7.15: Inductive method, top electrode response at 400kHz

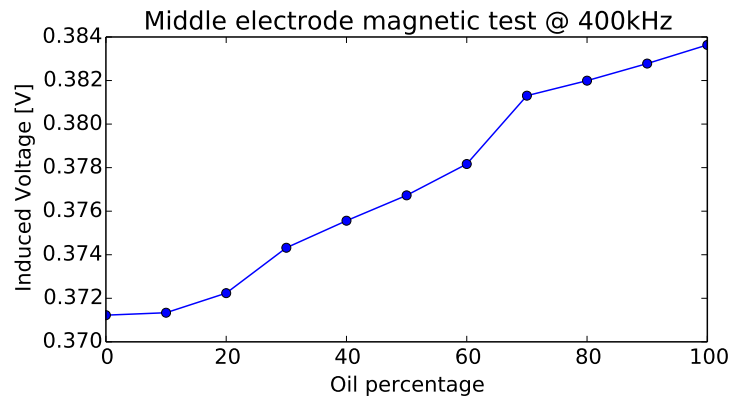


Figure 7.16: Inductive method, middle electrode response at 400kHz

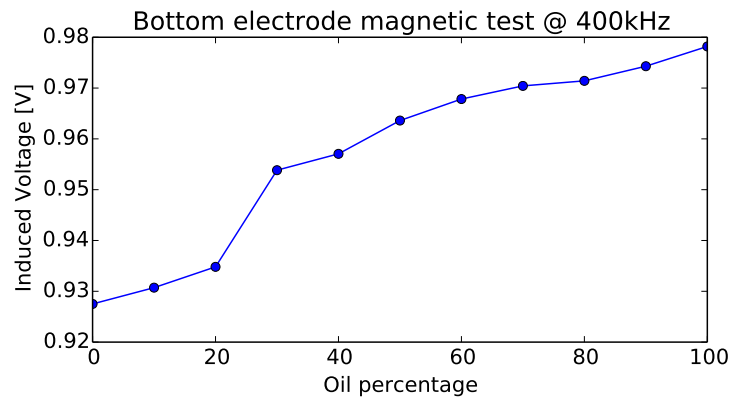


Figure 7.17: Inductive method, bottom electrode response at 400kHz

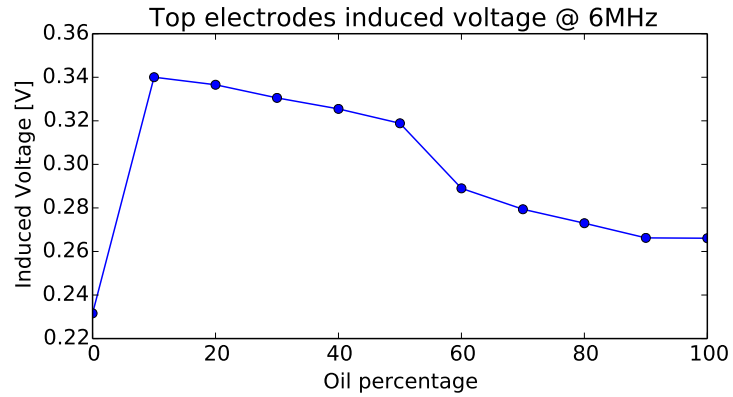


Figure 7.18: Inductive method, top electrode response at 6MHz

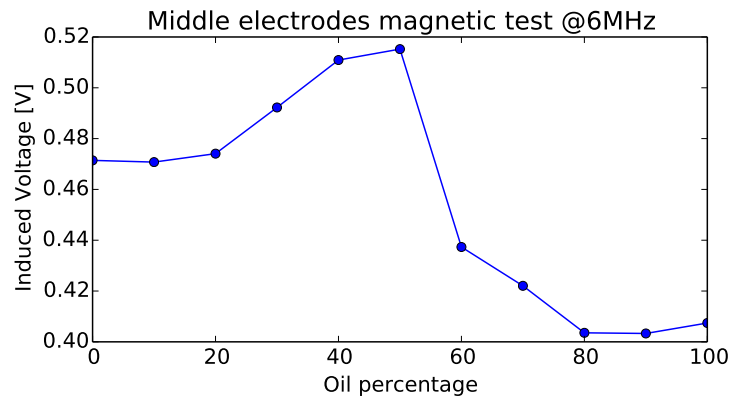


Figure 7.19: Inductive method, middle electrode response at 6MHz

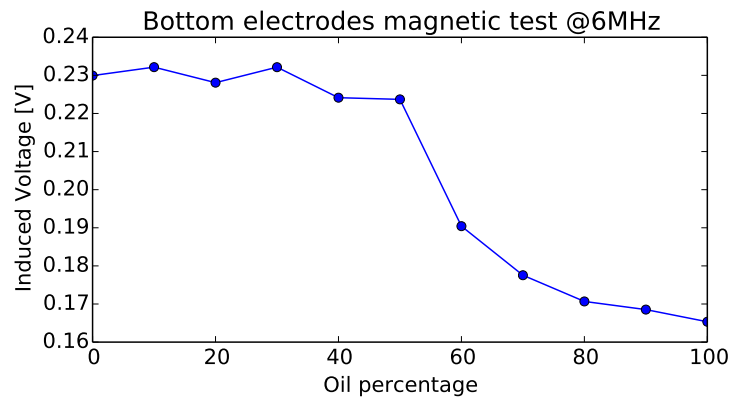


Figure 7.20: Inductive method, bottom electrode response at 6MHz

Chapter 8

Conclusion And Future Work

This thesis describes research work completed regarding the capacitive method for multiphase flow measurement. The capacitive technique is technically easier to implement relative to other techniques on the market, for example gamma ray or pulsed neutron activation. The power levels needed for capacitive type measurement are so low that a sensor operating with this principle does not require any special handling. Neither does it require any radioactive material nor generate any byproducts. The capacitive electrodes are insulated, which means that they are not in contact with the fluid under measurement. This characteristic makes the sensor intrinsically safe. The insulating layer for this sensor should be robust enough to stand abrasion from sand particles in the mixture, which renders the sensor maintenance free. This sensor uses a hydrocyclone to separate temporarily the flow into single phases during the measurements whereas other methods use a mixer to homogenize the flow. Mixing devices may create an emulsion that is difficult to separate downstream. According to this research, the main challenge with this sensor is the lack of accuracy at lower oil compositions. This could be improved by using the turbocyclone concept. After an initial calibration process, this sensor won't need to be recalibrated, and will be

able to operate over a wide range of changes in electrical properties of oil and water. The results obtained along this research show that a sensor using the principles explored in this research could be used in real time measurements for two phase flow and the accuracy of this sensor could be similar to other oil and water sensors that are currently in the market. A brief summary of the accomplishments done during this research are outlined below.

A novel technique in which a hydrocyclone is combined with a capacitive array is introduced and studied in Chapter 3 at both the theoretical and practical levels. The sensing principles were verified analytically at two different levels of complexity and also numerically using FEM modeling. The experimental validation provided a practical insight into a potential realization of the instrumentation system and resulted in quality data with large resolutions and good repeatability across a wide range of multiphase compositions. A sidetracked study into using a magnetic phenomena in multiphase flow sensing did not prove the initial hypothesis but re-confirmed the efficiency of the capacitive sensing for multiphase composition measurement.

Having targeted a practical application the measurement uncertainty was given a large portion of this study. The sensors and other instruments in general tend to work seamlessly with an unchanged accuracy when operated in a controlled laboratory environment in which the parameters are kept free of drifting. This is not, however, the case of field instruments, where other parameters unrelated to the main measurement but which do influence the measurement, undergo some drifting. A study on the robustness of the proposed sensor was conducted in terms of parameter drifting and concluded that the underlying principle of modulating the phase interface in a cyclone to effectively decouple the individual capacitance measurements gives an indication of practical efficiency.

The main focus of this research was not in the area of fluid dynamics to study and

optimize the hydrocyclone process, however some CFD simulations were conducted. This simulations allows to improve the sensor design by finding the best place to locate the electrodes inside the cyclone. In the theoretical analysis, it was assumed the phases were completely stratified and separated creating a well bounded domains of water and oil. This proved as valid assumption in case of oil concentrations between 40% to 100%, however when water phase exceeds 60% instability was observed. This phenomena is believed to attribute to the case of turbulent flow in which the water phase and oil phase are partially mixed together. A study in Chapter 4 explained the challenges with water, a phase of large electrical conductivity. The same composition but different continuous phase material resulted in completely different capacitance data. The phase dispersed in the continuous phase was found to have lesser effect towards the resulting capacitance. This was an important finding that confirmed the need for an actively agitated cyclone, a.k.a. turbocyclone where the holding time can be controlled and full separation eventually achieved.

Passive hydrocyclone in order to function properly requires a minimal flow velocity to promote the phase stratification. Since the stratification process is flow velocity dependent, naturally, the flow velocity will influence the measurement accuracy. An experimental calibration flow loop was built that features a gravity based separator, two positive displacement pumps and a mixing tee to create water-oil mixtures across 0-100% composition. Chapter 5 explains the process of developing the experimental test bed and the data gathering instrumentation.

The calibration data in Chapter 6 indicate the strength of capacitive sensing for multi-phase composition measurement. The developed instruments can be readily adopted by the industry without any modification when the oil phase ranges between 40% to 100%. However, as a general instrument, continued investigation to broaden the range of the composition to 0-100% is required. Different capacitance measurement

techniques were implemented, such as inverting amplifier method or the capacitance to frequency converter. A part of this study used the cylindrical electrodes created by a transformer wire as a coil. The wire is insulated and made the electrode fabrication very versatile. The case of magnetic induction of this two-port, four terminal network was also investigated. It was assumed that the mutual inductance between the two coils is being modulated by the volume of water phase that is conductive. This phenomena was reported in a study on LVDT (linear variable differential transformer) flowmeter for conductive fluids. Unfortunately, such correlation was not found. On the contrary, the same characteristics observed earlier using purely the capacitance were found.

In Chapter 7, hydrocyclone designs in the passive mode of operation were used and a flow visualization of the hydrocyclone process was conducted. Only the water phase was used in order to investigate the type of flow in the hydrocyclone at large water concentrations. A hydrogen bubble stream was generated by a pulsed electrolysis but the visual quality was not sufficient to draw any conclusion on the flow turbulence. Instead, the rotational velocity in the hydrocyclone that is responsible for the phase stratification was measured. This data will be used in future to optimize the hydrocyclone design. This was an important study of the fundamental principles but again did not provide a confirmation of the turbulent nature of flow when the water ratio exceeds 60% and our experimental data exhibit a large standard deviation. The future turbocyclone concept is expected to provide more flexibility in terms of rotational speeds developed and liquid holding time within the cyclone's chamber. An 'outer spinner' turbocyclone was rapid prototyped, which was found having many mechanical problems. The rapid prototyping did not prove very efficient in this flow system. In the future, the plan is to develop a direct drive motor based turbocyclone that is completely sealed with fewer moving parts and simpler driving mechanism.

8.1 Future Work

The knowledge of composition alone is not the only parameter the industry desires to measure. The total flow rate is another critical parameter defining the process. In future, different methods to extract the flow data from the hydrocyclone will be explored as one cannot always assure the two stratified phases to flow at the same speed.

One solution that may gain industries' attention relates to using the hydrocyclone for phase separation. The sensor developed in this research can provide the phase interface localization needed for the separation process. As a result of this research, a new project in collaboration with the University of Copenhagen that leads in research into hydrodynamic modeling of hydrocyclones for oil-spill remediation will start, however, their expertise is lacking in terms of the sensory system needed for the two degree-of-freedom control (valve on the produced water line, and valve on the hydrocarbons line). A new high efficiency separator will be developed to be used in environmental spill cleanup as well as in production.

Current trends indicate that oil production will soon be moving to more hostile environments such as very deep offshore fields or harsh arctic environment since the production at many existing fields is in rapid decline. These harsh conditions pose new challenges to the offshore O&G production and more processing technologies at the seabed will be seen than at the surface. The phase stratification and separation is designed with such potential applications in mind and phase separation can be introduced into the existing design. Large ambient (hydrostatic) pressures are also considered and the overall reliability in terms of fouling, corrosion/abrasion will have to be considered.

Chapter 9

Publications

During this research the following publications were made:

1. Ortiz J., Karwal A. & Masek V. (2008), “Sensor callibrator: PC based multiphase flow loop instrumentation”, IEEE Eighteenth Annual Newfoundland Electrical and Computer Engineering Conference.
2. Ortiz, J., & Masek, V. (2010). “Magnetic fractional component sensor”, Newfoundland Electrical and Computer Engineering Conference.
3. Masek, V. & Ortiz J. (2010), “Magnetic multiphase composition sensor”, Magnetic Measurements MM2010 Conference, Prague, Czech Republic, 2010.
4. Ortiz, J.,& Masek, V. (2011), “Multiphase calibration flow loop instrumentation test bed”, Newfoundland Electrical and Computer Engineering Conference NECEC.
5. Ortiz, J. & Masek, V. (2012), “Magnetic water cut sensor”, Newfoundland Electrical and Computer Engineering Conference.

6. Masek, V. & Ortiz, J. (2012), “Multiphase composition sensor”, Magnetic Measurements MM2012 Conference Tatranské Matliare, Slovakia.
7. Masek, V. & Ortiz, J. (2014), “Capacitive cyclonic sensor for oil spill remediation”, OCEANS’14 MTS/IEEE St. John’s Conference.
8. Ortiz, J. & Masek, V., “Cyclonic Capacitive Sensor For Multiphase Composition Measurement”, Sensors & Transducers Journal (Currently being review 2015).

References

- [1] Framo Engineering As. “Framo Multiphase Flow Meters Phase Watcher Vx”. April 2003.
- [2] A.F. van den Heuvel et al. “Are Multiphase Flow Meters ready for calibration?”. Milestones in Metrology, 2012.
- [3] R Thorn, G. A. Johansen and E A Hammer. “Recent developments in three-phase flow measurement”. Meas. Sci. Technol 8, 1997, pp. 691-701.
- [4] Ian Atkinson *et al.* “A New Horizon in Multiphase Flow Measurement”. Oilfield Review, Volume 16, Issue 4, December 2004.
- [5] The Norwegian society for Oil and Gas Measurement, The Norwegian Society of Chartered Technical and Scientific Professionals. “Handbook of Multiphase Flow Metering”, Revision 2, March 2005
- [6] G. Falcone, G. F. Hewitt, C. Alimonti and B. Harrison. “Multiphase Flow Metering: Current Trends and Future Developments”. Society of Petroleum Engineers. April 2002.
- [7] Neima Brauner. “Modelling and Control of Two-Phase Phenomena: Liquid-liquid Two-Phase Flow Systems”. School of Engineering, Tel-Aviv University.

- [8] Arirachakaran, S., Oglesby, K. D., Malinowsky, M. S., Shoham, O., and Brill, J. P. "An analysis of oil/water flow phenomena in horizontal pipes". Paper presented at SPE Production Operation Symposium. (SPE 18836) March, Oklahoma City (1989).
- [9] Ibrahim M. M.Babelli. "In Search of an Ideal Multiphase Flow Meter for the Oil Industry". *Arabian Journal of Science and Engineering*, Volume 27, Number 2B, October 2002, pp. 113 – 126.
- [10] Mahmoud Meribout, Nabeel Z. Al-Rawahi, Ahmed M. Al-Naamany, Ali Al-Bimani, Khamis Al-Busaidi, and Adel Meribout. "A Multisensor Intelligent Device for Real-Time Multiphase Flow Metering in Oil Fields". *IEEE Transactions on Instrumentation and Measurement*, Vol. 59, no. 6, June 2010.
- [11] Yingwei Li, Jing Gao, Xingbin Liu, and Ronghua Xie. "Energy Demodulation Algorithm for Flow Velocity Measurement of Oil-Gas-Water Three-Phase Flow". Hindawi Publishing Corporation, *Mathematical Problems in Engineering*. Volume 2014, Article ID 705323, 13 pages.
- [12] Halit Eren. "Magnetic flowmeters". *The Measurement, Instrumentation and Sensors Handbook*. John G. Webster Science. CRC Press, LLC, 2000.
- [13] Jesse Yoder. "Principle of Attraction: The Rise of Magnetic Flowmeter Technology", *Flow Control*, January 2005.
- [14] Shercliff, J. A. "Relation between the velocity profile and sensitivity of electromagnetic flowmeters". *J. Appl. Phys.* 25, 1954, pp. 817.
- [15] T. Leeungcalsatien and G.P. Lucas. "Measurement of Velocity Profiles in Multiphase Flow Using a Multielectrode Electromagnetic Flow Meter". *Computing and Engineering Researchers' Conference*, University of Huddersfield, March 2012.

- [16] R. Al-Rabeh, R.C. Baker, J. Hemp. "Induction flow-measurement theory for poorly conducting fluids". Proceedings of the Royal Society of London. Series A, Mathematical and Physical Sciences, Vol. 361, No. 1704, May 3, 1978, pp. 93-107.
- [17] M. Sami A. Abouelwafa and E. John M. Kendall. "The Use of Capacitance Sensors for Phase Percentage Determination in Multiphase Pipelines", IEEE Transactions on Instrumentation and Measurement, Vol. IM-29, No. 1, March 1980.
- [18] Devin Lowe and Kamiel S. Rezkallah "A capacitance sensor for the characterization of microgravity two-phase liquid-gas flows". 1999 Meas. Sci. Technol. Vol. 10, No. 10, pp. 965.
- [19] M. Merilo, R. L. Dechene, W. M. Cichowlas. "Void Fraction Measurement With a Rotating Electric Field Conductance Gauge". Trans. ASME J. Heat Transfer Vol. 99, May 1977, pp.330-332.
- [20] G.P. Lucas, S. Simonian. "Towards a phase-distribution-independent impedance volume-fraction measurement". Flow Measurement and Instrumentation, 1991, pp. 105-114.
- [21] Wael H. Ahmed and Basel I. Ismail. "Innovative Techniques For Two-Phase Flow Measurements", Recent Patents on Electrical Engineering 2008, 1, 1-13.
- [22] Salah I, Al-Mously, and Ahmed Y. Ahmed. "The Use of a Coaxial Capacitor as a Capacitance Sensor for Phase Percentage Determination in Multiphase Pipelines", 10th Mediterranean Electrotechnical Conference, MELECON 2000, Vol. 2.
- [23] Schlumberger. "Fundamentals of Multiphase Metering". ISBN-13:978-097885305-1, 2010.

- [24] Heron Eduardo de Lima Ávila, Daniel J. Pagano, Fernando Rangel de Sousa. “Water Fraction Measurement Using a RF Resonant Cavity Sensor”, 19th Symposium IMEKO TC 4 Symposium and 17th IWADC Workshop. Advances in Instrumentation and Sensors Interoperability July 18-19, 2013, Barcelona, Spain
- [25] Scheers, A.M., Letton, W. “An oil/water/gas composition meter based on multiple energy gamma ray absorption (MEGRA) measurement”, Proceedings of the 14th North Sea Flow Measurement Workshop, Peebles, Scotland, 1996.
- [26] L. Finkelstein, K T V Grattan. “Concise Encyclopedia of Measurement and Instrumentation”. Pergamon Press, 1994.
- [27] R. Krafft, J. Hemp and M. L. sanderson. “Investigation into the use of the Electromagnetic Flowmeter for two-phase Flow Measurements”. Advances in Sensors for Fluid Flow Measurement, IEEE Colloquium on, April 1996.
- [28] MBA Polymers. “Development of Hydrocyclones for Use in Plastics Recycling”. A Summary Report of Research Sponsored by the American Plastics Council. July 1998.
- [29] Hironori Watanabe, Hidesada Tamai, Takashi Satoh, Mitsuhiro Shibata and Toru Mitsutake (2012). “Development of Capacitance Void Fraction Measurement Method for BWR Test, Flow Measurement”, Dr. Gustavo Urquiza (Ed.).
- [30] R. Thorn, G. A. Johansen, and B. T. Hjertaker. “Three-phase Flow Measurement in the Petroleum Industry”. Measurement Science and Technology (2013).
- [31] D. C. Meeker. “Finite Element Method Magnetics, Version 4.2”, October, 2010., <http://www.femm.info>

- [32] Mahmoud Meribout, Ahmed Al Naamany and Khamis Al Busaidi. “Interface Layers Detection in Oil Field Tanks: A Critical Review”. Expert Systems for Human, Materials and Automation (2011), Prof. Petrică Vizureanu (Ed.), ISBN: 978-953-307-334-7
- [33] Micropump Inc. A unit of IDEX corporation, “Micropump IDEX Health and Science, I-Drive, Installation, operation warranty information”. March 2006, Micropump Inc.
- [34] Van der Linden, “Capacitive Sensors: Design and Applications”, Wiley-IEEE Press, 1996, pp. 133.
- [35] A.J. Smits, T.T. Lim. “Flow Visualization, Techniques and Examples”. Imperial College Press, World Scientific Publ., 2000.
- [36] R. Burley, P.J. Grigg. “A solid state pulser for the hydrogen bubble (flow visualization) technique”. Journal of Physics E: Scientific Instruments. Volume 3, No. 12, pp.1018, 1970.
- [37] Malmberg, C.G. and Maryott, A. A. “Dielectric Constant of Water from 0 to 100C”. Journal of Research of the National Bureau of Standards. Vol.56, No.1, January 1956.
- [38] Guy Serbin. Dielectric Permittivity of Free Water.
- [39] T. J. Heimovaara, “Frequency Domain Analysis of Time Domain Reflectometry Waveforms 1. Measurement of the Complex Dielectric Permittivity,” Water Resources Research, vol. 30, pp. 189-199, 1994.

- [40] Meissner, T. and Wentz F. J. “The Complex Dielectric Constant of Pure and Sea Water From Microwave Satellite Observations”. IEEE Transactions on Geoscience and Remote Sensing, Vol. 42, No. 9, September 2004.
- [41] Trond Friisø, Yannick Schildberg, Odile Rambeau, Tore Tjomsland, Harald Førdedal and Johan Sjøblom. “Complex Permittivity of Crude Oils and Solutions Of Heavy Crude Oil Fractions”, Journal of Dispersion Science and Technology, 1998, Vol. 19 Issue 1, pp. 93-126.
- [42] A.F. van den Heuvel et al. “Are Multiphase Flow Meters ready for calibration?”Milestones in Metrology 2012.

Bibliography

- [1] Arnold, K., and Stewart, M. (1999). “Surface Production Operations” (2nd Edition) Volume 1 – Design of Oil-Handling Systems and Facilities. In Surface Production Operations (2nd Edition) Volume 1 – Design of Oil-Handling Systems and Facilities (pp. 101-159).
- [2] Fraden, Jacob. “Modern Sensors, Physics, Designs, and Applications”, 3rd ed. Advanced Monitors Corporation, San Diego, California. Springer, 2004.
- [3] Carlos Gomez *et al.* “Oil-Water Separation in Liquid-Liquid Hydrocyclones (LLHC)- Experiment and Modeling”, Annual Technical Conference and Exhibition, 2001. Society of Petroleum Engineers Inc.
- [4] Eilnaz Pashapour. “Capacitive Array Sensor for Two-Phase Liquid Characterization”. Masters Thesis, Faculty of Engineering and Applied Science, Memorial University of Newfoundland, December 2007.
- [5] CSC – IT Center for Science. “Elmer Tutorials”. January 20, 2010.
- [6] Oleksandr P. Ivakhnenko, David K. Potter. “Magnetic Susceptibility of Petroleum Reservoir Fluids”. Physics and Chemistry of the Earth, Volume 29, Issue 13-14, p. 899-907, Publication Date: 00/2004.

- [7] Balanis, Constantin. “Advanced Engineering Electromagnetics”. John Wiley and Sons, Inc., 1989.
- [8] “Fluke Instruction Manual 8920A/8921A True RMS Voltmeter”. October 1978.
- [9] “Fluke Programmable Automatic RCL Meter PM6306. Instruction Manual”, May 1996, Rev. 2, 02/99.
- [10] Aalborg. “GFM mass flow meter”. http://www.aalborg.com/index.php/main_page/product_overview/id_product_overview/20
- [11] Industrial Electronics Information for Manufacturing Applications “Current-to-Pressure (I/P) Converters”. http://www.industrial-electronics.com/output_devices_amplifiers_valves_relays_variable-frequency_drives_stepper_motors_servomotors/Current-to-Pressure_I-P_Converters.html
- [12] Omega.com. “Current to Pressure (I/P) Converter”. <http://www.omega.com/pptst/IP210.html>; accessed July 2014.
- [13] Williams S., Nevin Ch., Harding C., Sturge C., “Design, Construction, and Installation of a Three Phase Separator, Final Report”. Faculty of Engineering and Applied Science, Memorial University of Newfoundland.
- [14] Great Plains Industries, Inc., “GPI Pulse Out with Display, Owner’s Manual”.
- [15] Aalborg Instruments and Controls, “Operating Manual Totalizer”, Technical Data Sheet No. TD003 Rev. E, Date of Issue: March 1, 2004.
- [16] Burkert Fluid Control Systems “Inline Fittings S030, Instruction Manual”.
- [17] Burkert Fluid Control Systems “Operating Instructions Type 8623-2, Standard Compact Flow Controller”

- [18] B.R. Clayton, B.S. Massey. “ Flow Visualization in Water: A Review of Techniques”. Journal of Scientific Instruments. 1967, vol 44.
- [19] Massachusetts Institute of Technology, Experimental Techniques in Fluids. “Flow visualization, Electrolytic Techniques”. http://web.mit.edu/fluids-modules/www/exper_techniques/5.Electrolytic_Techniques.pdf; accessed August 04, 2014.
- [20] Park, J. and Back, N.G. “Dependence of Salt in Water-in-Crude Oil Emulsion System”. Journal of the Korean Physical Society, Vol. 47, September 2005, pp.S255~S258.
- [21] Reimer, E.M. and Rossiter, J.R. “Measurement of Oil Thickness on Water from Aircraft: A. Active Microwave Spectroscopy, B. Electromagnetic Thermoelastic Emission”. Environmental Studies Research Funds Report No. 078; 1987.
- [22] Pecovska-Gjorgjevich M., Andonovski A., and J. Velevska “Measuring frequency and temperature-dependent permittivities of vegetable oils”. Physica Macedonica 59, (2011) p. 77-89.
- [23] Carey, A.A. “The Dielectric Constant of Lubrication Oils”. Computational Systems Incorporated, 1998.

Appendix A

Flow Loop

A.1 Gear Pumps

The gear pumps employed in the flow loop were manufactured by Micropump Inc. They use the meshing of gears to pump the fluid by positive displacement principle. The electrical characteristics are shown in the table A.1

Table A.1: Lead Wire Assignments

lead	Function	Color	0-5VDC 4-20mA control	Manual control
1	Power In	Red	+ 24VDC	
2	Common	Black	Isolated from motor housing	
3	Control Signal In	white	0-5 VCD or 4-20 mA	potentiometer
4	Tachometer Out	Green	5V square wave-2 pulses per revolution	
5	FWD/REV	Orange	Forward (float and insulate), reverse ground	
6	Shield	-	Connected to housing	

A.2 Data Acquisition Card

The Data acquisition card was a PC30D DAQ card manufactured by Eagle Technologies. The DAC were used to control speed of the gear pumps that controls the percentage of oil and water in the pipes. Each DAC can be configured for 0 to +10V unipolar or $\pm 10V$ bipolar. In this case they were configure for 0 to +10V, according to the tables A.2 and A.3

	Jumpers	
DAC0 Output Range	W3	W4
0 to + 10 V	Out	In
-10 to +10 Volts	In	Out

Table A.2: Jumper Configuration for DAC0

	Jumpers	
DAC1 Output Range	W2	W1
0 to + 10 V	Out	In
-10 to +10 Volts	In	Out

Table A.3: Jumper Configuration for DAC1

Appendix B

Water and Oil Permittivities

B.1 Water Permittivity

The electrical absolute permittivity is the relation between the intensity of electric field intensity $E \left[\frac{V}{m} \right]$ and the electric flux density $D \left[\frac{C}{m^2} \right]$. The electric permittivity is a complex number that depend on the frequency. The variations of the permittivities of oil and water with the frequency are calculated and and shown below.

The static electrical permittivity of water, according to Malmberg *et al* [37] is given by

$$\epsilon = 87.440 + 0.40008t + 9.398(10^4)t^2 - 1.410(10^{-6})t^3 \quad (B.1)$$

The variation in water permittivity with temperature according to this equation are shown in figure B.1.

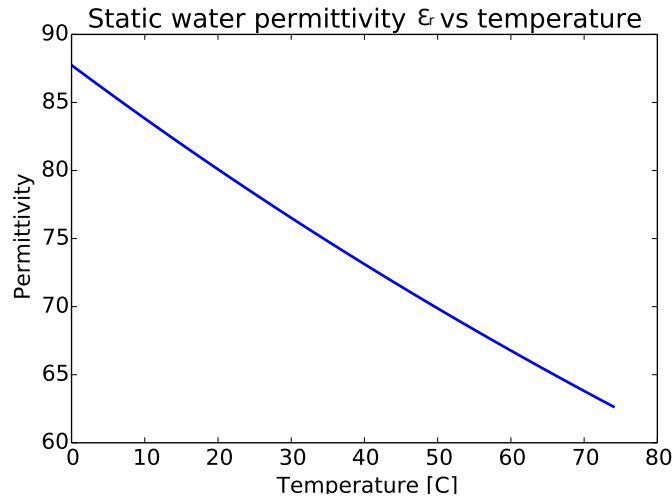


Figure B.1: Static permittivity of water

The previous model does not take into account the effects of frequency. The permittivity of water is a complex number that depends upon the frequency and temperature. This dependency can be described according to the Cole-Cole model [38][39] for frequencies below microwaves:

$$\varepsilon_{H_2O}^*(f, T) = \varepsilon_{\infty} + \frac{\varepsilon_s(T) - \varepsilon_{\infty}}{1 + j \left(\frac{f}{f_{rel}(T)} \right)^{1-\beta}} - \frac{j\sigma_{dc}(T)}{2\pi f \varepsilon_0} \quad (B.2)$$

where:

- $\varepsilon_s(T)$ is the electric permittivity of water at a temperature T in C.
- ε_{∞} is the electric permittivity of water at high frequencies and in the range of 0 to 60 ° has a value of 4.25
- $f_{rel}(T)$ is the relaxation frequency of the material [Hz]
- $\beta = 0.0125$ is a factor which accounts for a possible spread in relaxation frequencies.
- $\sigma_{dc}(T)$ is the conductivity of the water at a temperature T, and
- ε_0 is the permittivity of free space, and is equal to $8.854 \times 10^{-12} \left[\frac{F}{m} \right]$

Figures B.2, B.3 and B.4 show the changes in the magnitude, in the real and imaginary parts of water permittivity with frequency. The figures B.5 and B.6 show the change in the permittivity with temperature and frequency. As it can be seen from these figures, the effect of the frequency is very small, compared with the temperature. During the experiments in this research, a fixed value of water permittivity was considered. At higher frequencies, the permittivity can be greatly affected and other models can be applied [40].

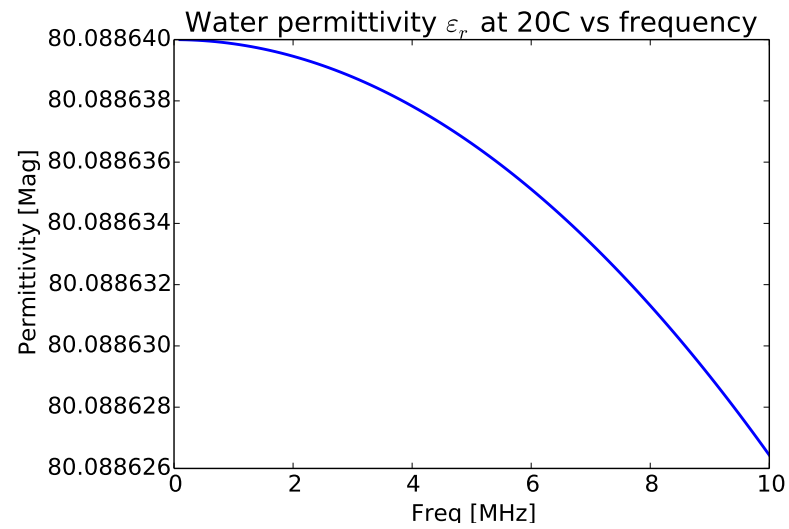


Figure B.2: Variation in the permittivity of water (magnitude) with frequency at a fixed temperature

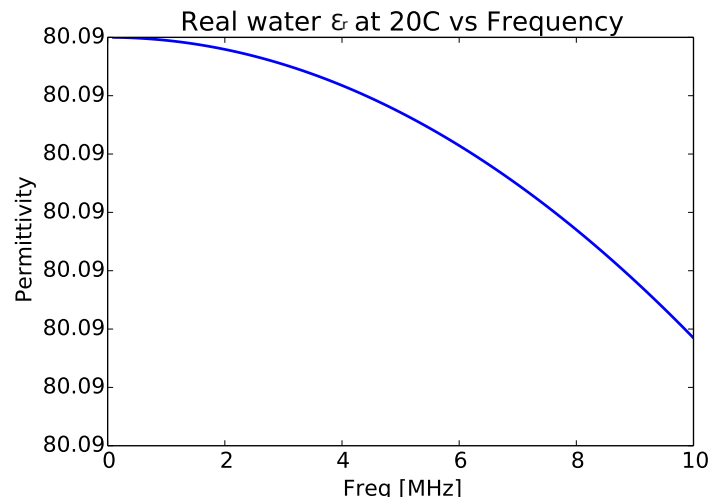


Figure B.3: Variation in the real part of permittivity of water with frequency at a fixed temperature

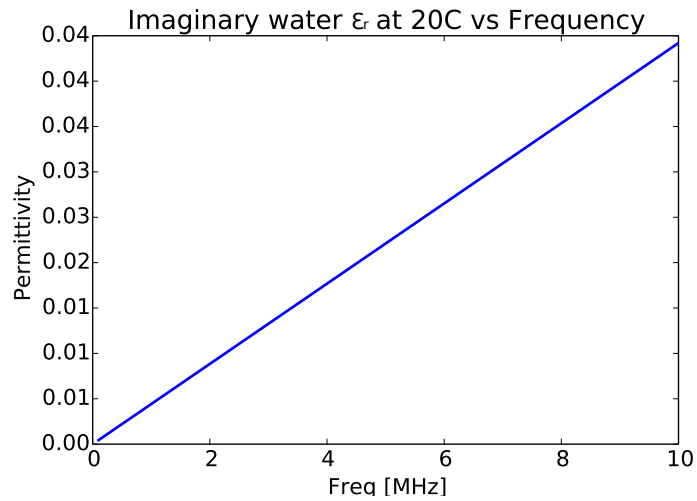


Figure B.4: Variation in the imaginary part of the permittivity of water with frequency at a fixed temperature

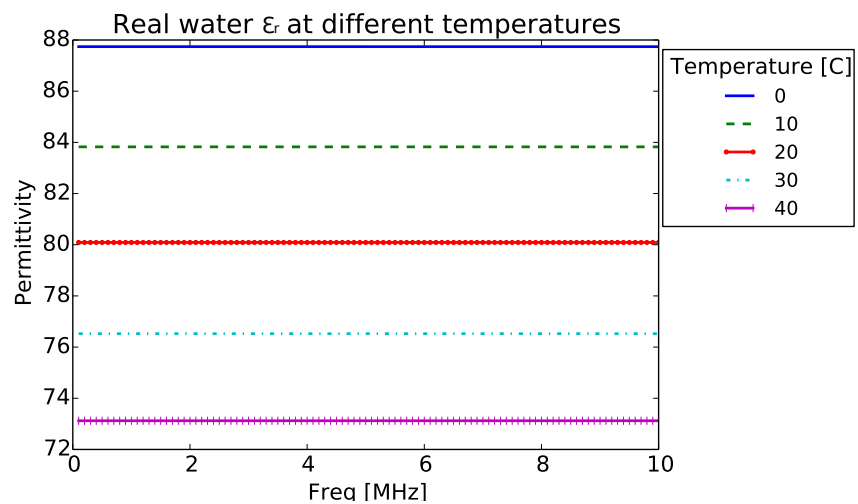


Figure B.5: Variation in the real part of ϵ_{H_2O} vs frequency at different temperatures

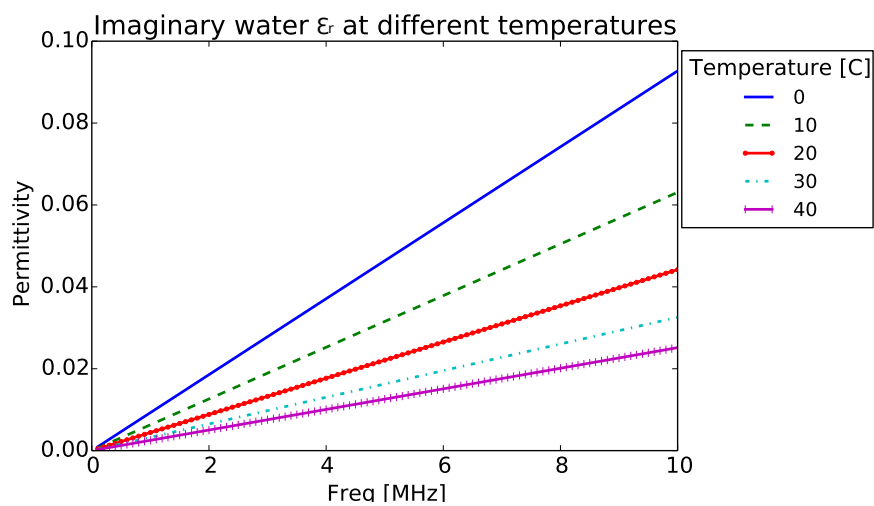


Figure B.6: Variation in the imaginary part of ε_{H_2O} vs frequency at different temperatures

B.2 Oil Permittivity

In 1998, Trond *et al* [41], characterized oil samples from five different field operated by Elf. They provide the Cole-Cole function that describe the behaviour of those samples:

$$\varepsilon_{Oil}^*(\omega) = \varepsilon_{\infty} + \frac{\varepsilon_s - \varepsilon_{\infty}}{1 + (j\omega\tau)^{1-\alpha_p}} + \frac{\varepsilon_p - \varepsilon_s}{1 + (j\omega\tau)^{1-\alpha_p}} - \frac{j\sigma_{dc}}{\varepsilon_0\omega} \quad (B.3)$$

Table B.1: Cole-Cole Parameters for the Spectra of the Crude Oils B1 and B2

crude oil	ε_s	ε_{inf}	τ	α	$\sigma [nS/m]$
B1	2.666	2.260	9.92	0.67	14.0
B2	2.302	2.174	3.375	0.55	12.1

The variation of permittivity for the samples B1 and B2 according to the values in table B.1 are shown in figures B.7 B.8 and B.9.

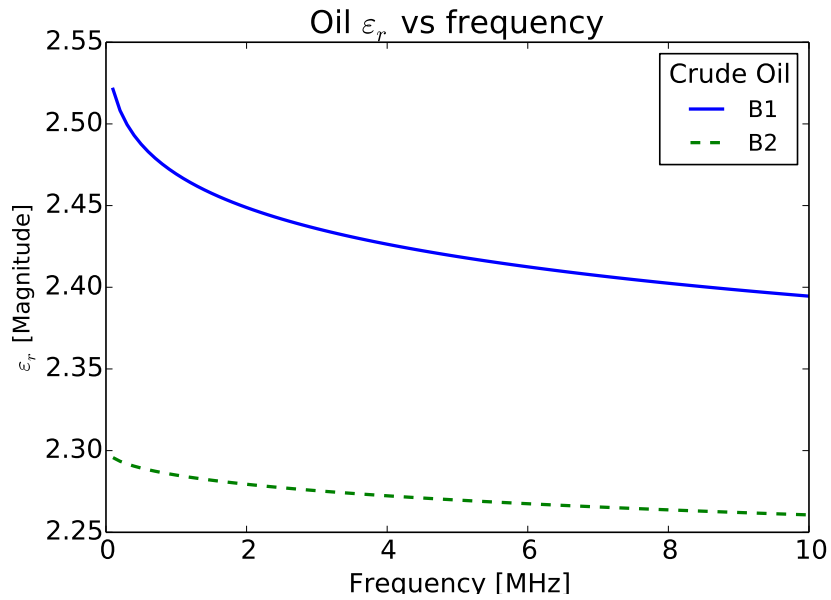


Figure B.7: Variation in magnitude of ε_{Oil} vs frequency

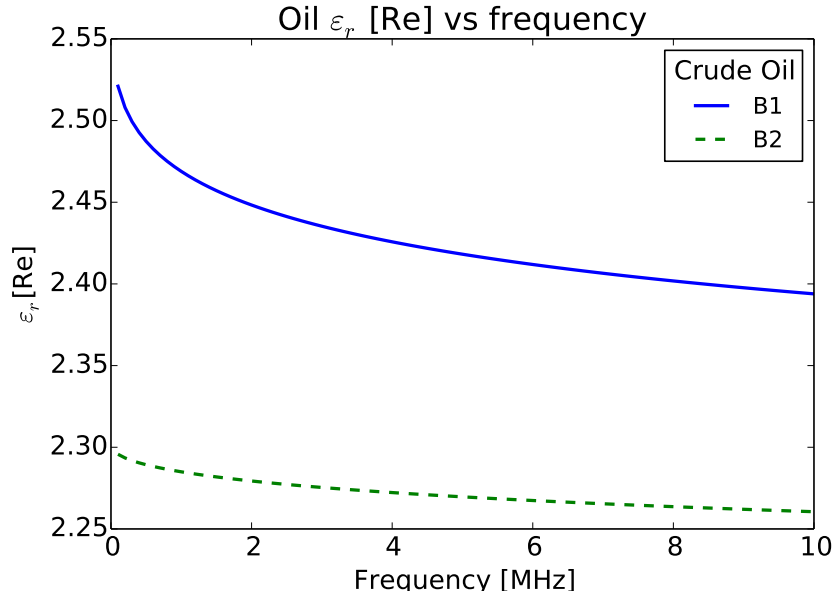


Figure B.8: Variation in the real part of ε_{Oil} vs frequency

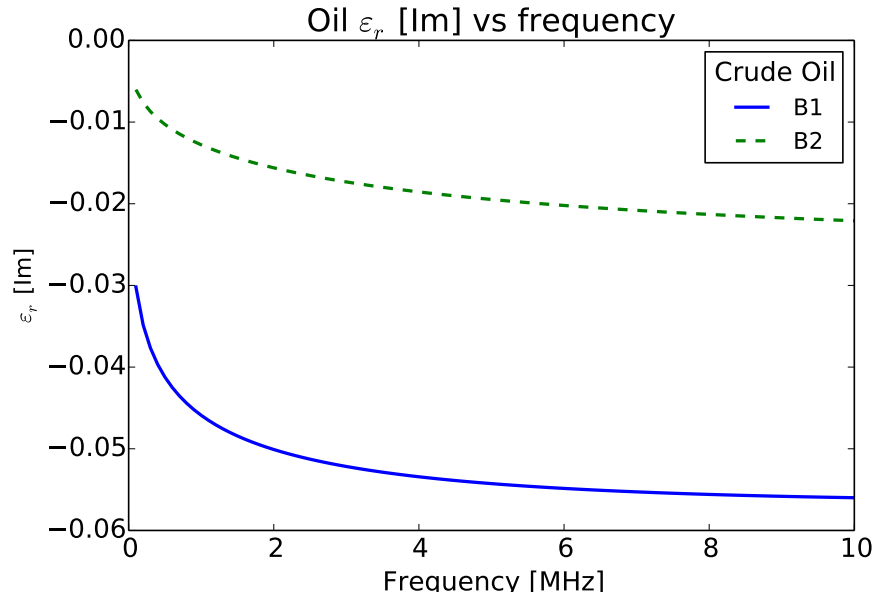


Figure B.9: Variation in the imaginary part of ε_{Oil} vs frequency